MAGNETO-OPTICAL STUDY OF GERMANIUM AND III - V COMPOUNDS USING THE PHOTOELECTROMAGNETIC EFFECT

by

Alain J. Barbarie

Submitted to the School of Graduate Studies of the University of Ottawa in partial fulfillment of the requirements for the degree of Doctor of Philosophy

Department of Physics
Faculty of Science and Engineering
University of Ottawa
OTTAWA, Canada

1974

to my parents

STATEMENT OF ORIGINALITY

Given below is a list of work done during the course of this study which, to the best of the author's knowledge, had not been previously undertaken:

1) The first observation in the photoelectromagnetic effect of Ge, GaSb, InP, and GaAs of magneto-optical structures associated with transitions between Landau levels.

2) A simple line shape study of magneto-optical structures observed by a direct method (as opposed to a modulated technique).

3) The analysis of the magneto-optical structures in the photoelectromagnetic spectral distribution in terms of the Pidgeon and Brown formulation.

4) The first observation in InP of magneto-optical structures associated with transitions between Landau levels.

5) Some theoretical developments concerning the mobility of diffusing carriers in intense magnetic fields.

6) The use of pyrolytically deposited aluminum oxide films to preserve oxidation-free surfaces.

7) The first observation in the photoelectromagnetic effect of GaSb and InP of spectral oscillations associated with the longitudinal optical phonon transitions.

8) A study of the mechanisms relating the surface oxidation of

the samples with the apparition in the photoelectromagnetic effect of broad oscillations associated with longitudinal optical phonons (of the type usually observed in photoconductivity).

ABSTRACT

Some theoretical developments demonstrate that the magnitude of the photoelectromagnetic (PEM) effect varies with the absorption coefficient of the semiconductor above the fundamental edge. A rather simple and straightforward method of studying direct interband magneto-optical transitions between Landau levels can be achieved by observing the oscillatory spectral distribution of the PEM effect. The method was first applied to two germanium samples at a temperature of 4.2K, over the energy range 0.9 - 1.1 eV, using linearly polarized light parallel and perpendicular to magnetic fields of up to 70 kG applied along the [111] direction of the crystals. The spectral oscillations are analysed in terms of the Pidgeon and Brown formulation. The analysis yields values for the direct bandgap energy, the ground state exciton binding energy, and the band parameters. A line shape study of the magneto-optical structures predicts a shift of the energy position of the maxima towards the higher energies with increasing impurity scattering. Provided one accounts for the above energy shift, the band parameter values obtained for Ge using the PEM technique are in excellent agreement with the previously published theoretical and experimental results. Having verified that the PEM technique is accurate and reliable, the method was extended to the study of other less investigated semiconductors such as GaSb and InP. These are hetero-polar materials and under certain specific surface conditions resulting from oxidation, broader spectral

oscillations associated with longitudinal optical (LO) phonons could be observed. A pyrolytic coating process was used to preserve the clean surfaces necessary to observe the Landau structures in these materials. Contrary to the above, the photoconductivity spectra of GaAs exhibit better resolved magneto-optical structures than the PEM effect. The study of both an epitaxial and high resistivity GaAs gave us some insight in the mechanisms relating oxidation to the broader LO phonon structures. Photo-effects such as photoconductivity and the PEM effect offer an interesting alternative to the more complicated modulated reflectivity techniques.

List of Tables

2.1	Chemical Etches	30
2.2	Description of the samples studied	33
3.1	Matrix elements for the two symmetric 4 x 4 Pidgeon and Brown matrices.	45
5.1	Coding of the direct magneto-optical interband transitions	86
5.2	Identification of the experimental curves in the fan diagram of the E // B polarization PEM spectra of Ge (M).	87
5.3	Comparison of the band parameter values for Ge determined in the present experiment with previously published values.	89
5.4	Comparison of the band parameter values of GaSb determined in the present experiment with previously published values.	107
6.1	Recapitulative summary of the experimental results for the present research	140

List of Figures

2.1 A schematic description of the apparatus 25

2.2 A description of the sample holder 26

2.3 A description of the lower part of the cryostat containing the superconducting solenoid. 27

2.4 A schematic description of the power supply and control for the superconducting solenoid. 29

2.5 A description of the apparatus for the deposition of Al_2O_3 films.
A, B, dry N_2; C, constant temperature (140°C) oil bath; D, aluminum tri-isopropoxide; E, heating element; F, substrate holder; G, exhaust. 32

3.1 Energy levels for a simple two-band model in a magnetic field. 38

3.2 A schematic of the $\varepsilon(\bar{k})$ versus $\bar{k}$ curves in the vicinity of $\bar{k} = 0$ for the conduction and valence bands of III - V compounds. 39

3.3 The Landau levels for the conduction band and light- and heavy-hole bands (in the Pidgeon and Brown numbering system). The arrows represent the lowest energy interband transitions: the

solid arrows for the E // B right circular polarization, the dotted arrows for the E // B left circular polarization, and the dashed arrows for the $E \perp B$ polarization. 51

3.4 The absorption coefficient of a semiconductor as a function of the incident photon energy in the presence of a magnetic field: in the absence of scattering (dashed line), including scattering (solid line). The long dashed line denotes the absorption coefficient in the absence of a magnetic field. 55

3.5 A qualitative description of the broadening effects on a magneto-optical structure. 57

3.6 An illustration of our definition of visibility for the magneto-optical structures. 59

4.1 A description of the PEM effect. 64

4.2 The qualitative demonstration of a sign reversal for the diffusion of optically injected carriers due to the high surface recombination velocity in a surface layer of thickness x. 68

4.3 The LO phonon transition cascading process in the absence of a magnetic field. 70

4.4 The LO phonon transition cascading process in the presence of a magnetic field. 71

5.1 PEM spectra for the E // B polarization of both Ge (M) and Ge (N) at 20 kG. The dashed line indicates a peak scaled down by a factor of -3. 77

5.2 PEM spectra for the E ⊥ B polarization of both Ge (M) and Ge (N) at 50 kG. The dashed line indicates a peak scaled down by a factor of -3.. 78

5.3 Visibility of the magneto-optical structures in the PEM spectra of germanium versus the magnetic field strength. 79

5.4 Photon energy values at the maxima versus the magnetic field strength for the E // B polarization PEM spectra of Ge (M). The dashed lines represent the experimental curves, the solid lines the theoretical curves. 81

5.5 Photon energy values at the maxima versus the magnetic field strength for the E ⊥ B polarization PEM spectra of Ge (M). The dashed lines represent the experimental curves, the solid lines the theoretical curves. 82

5.6 Photon energy values at the maxima versus the magnetic field strength for the E // B polarization PEM spectra of Ge (N). The dashed lines represent the experimental curves, the solid lines the theoretical curves. 83

5.7 Photon energy values at the maxima versus the magnetic field strength for the E ⊥ B polarization PEM spectra of Ge (N). The dashed lines represent the experimental curves, the solid lines the theoretical curves. 84

5.8 Dember spectra for the E // B and E ⊥ B polarization of Ge (M) at 45 kG. 92

5.9 Photon energy values at the maxima versus the magnetic field strength for the E // B polarization Dember spectra of Ge (M). 93

5.10 Photon energy values at the maxima versus the magnetic field strength for the E ⊥ B polarization Dember spectra of Ge (M). 94

5.11 Visibility of the magneto-optical structures in the Dember spectra of germanium versus the magnetic field strength. 96

5.12 The Dember short-circuit signal as a function of the magnetic field strength. 98

5.13 PEM spectrum of the irradiated germanium sample Ge (M3). 99

5.14 PEM spectrum for the E // B polarization of GaSb (1). 102

5.15 PEM spectrum for the E ⊥ B polarization of GaSb (1). 103

5.16 Photon energy values at the maxima versus the magnetic field strength for the E // B polarization PEM spectra of GaSb (1). 104

5.17 Photon energy values at the maxima versus the magnetic field strength for the E ⊥ B polarization PEM spectra of GaSb (1). 105

5.18 PEM spectrum for the E // B polarization of GaSb (2) at 50 kG. 110

5.19 Photon energy values at the minima versus the magnetic field strength for the E // B polarization PEM spectra of GaSb (2). 111

5.20 Plot of the extrapolated photon energy values at B = 0 versus the phonon transition order. 112

5.21 PEM spectrum for the E // B polarization of InP (1). 115

5.22 PEM spectrum for the E ⊥ B polarization of InP (1). 116

5.23 Photon energy values at the minima versus the magnetic field strength for the E // B polarization PEM spectra of InP (1). 117

5.24 Photon energy values at the minima versus the magnetic field strength for the E ⊥ B polarization PEM spectra of InP (1). 118

5.25 PEM spectrum of InP (2) at 20 kG. 121

5.26 Photon energy values at the minima versus the magnetic field strength for the PEM spectra of InP (2). 122

5.27 Plot of the extrapolated photon energy values at B = 0 versus the phonon transition order 123

5.28 Comparison between the PEM spectrum and photoconductivity spectrum of GaSb (1) at 70 kG. 126

5.29 Comparison between the PEM spectrum and photoconductivity spectrum of GaSb (2) at 30 kG. 127

5.30 Photoconductivity spectrum of GaAs (1) at 60 kG. 128

5.31 PEM spectrum of GaAs (1) at 35 kG. 129

5.32 Photon energy values at the minima versus the magnetic field strength for the photoconductivity spectra of GaAs (1). 131

5.33 Photoconductivity spectra of GaAs (2) for both E // B and E ⊥ B polarization at zero field. 133

5.34 Photon energy values at the minima of the photoconductivity spectra of GaAs (2) versus the phonon transition order. 134

5.35 Photoconductivity spectrum of epitaxial GaAs at B = 0 given by Nahory. 135

5.36. The PEM short-circuit signal of GaSb (1), curve I, and GaSb (2) curve II, versus the magnetic field strength. 137

TABLE OF CONTENTS

Statement of Originality	3
Abstract	5
List of Tables	7
List of Figures	8
1. Introduction	19
2. Experimental Method	24
2.1 Apparatus	24
2.2 Sample Preparation	30
3. Magneto-Optical Properties	35
3.1 Direct Interband Transitions in a Magnetic Field	35
3.1.1 A simple two-band model	36
3.1.2 The treatment by Luttinger and Kohn	39
3.1.3 The Pidgeon and Brown scheme	43
3.1.4 A method of analysis using the Pidgeon and Brown scheme	47
3.1.5 The selection rules	50
3.2 Absorption Coefficient for a Semiconductor in a Magnetic Field	53
3.2.1 Direct interband magneto-absorption	53
3.2.2 A line shape study of the absorption structures	56

4. Transport Properties 62

4.1 The Photoelectromagnetic (PEM) effect 62

4.1.1 The classical treatment 62

4.1.2 The anomalous PEM effect 68

4.2 The Phonon-Electron Interactions in III-V Compounds 69

5. Experimental Results and Discussion 74

5.1 Germanium 75

5.1.1 The PEM effect 76

5.1.2 The Dember effect 91

5.1.3 The irradiated and pyrolytically coated surfaces 97

5.2 Gallium Antimonide 100

5.2.1 The interband transitions between the Landau levels 101

5.2.2 The phonon-electron interactions 108

5.3 Indium Phosphide 113

5.3.1 The interband transitions between the Landau levels 113

5.3.2 The phonon-electron interactions 120

5.4 Gallium Arsenide 120

5.4.1 The photoconductivity spectra 124

5.4.2 The epitaxial GaAs 125

5.4.3 The high resistivity GaAs 132

6. Conclusion - 138

Appendix 143

List of References 149

Acknowledgements 153

1. INTRODUCTION

Ever since the discovery of magneto-optical interband transitions in 1959 (1.1, 1.2), magneto-optical techniques have played an important role in the determination of band parameters in a number of materials (1.1 - 1.6). Of these materials, germanium and III - V compounds are characterized by strong direct interband transitions in which electrons at the top of the valence bands are photo-excited across the forbidden energy gap to the bottom of the conduction band. In a magnetic field the valence and conduction bands split up into a series of magnetic sub-bands called Landau levels. The energy separation between these levels and the photon energy required for an interband transition between them increase with increasing magnetic field strength. In this manner the optical properties of a semiconductor such as absorption and reflection are perturbed by the presence of a magnetic field. At first these effects where studied by optical transmission (1.1 - 1.2, 1.5 - 1.7). The rapid increase in the absorption coefficient with increasing photon energy greatly restricts the spectral region which can be investigated using this magneto-optical technique. The study of reflectivity removes the above restrictions. However, the magneto-optical structures of the reflectivity spectrum are so much weaker than those of the absorption spectrum that the magneto-reflectivity experiments proved even more difficult to perform.

In the early 60's differential techniques (1.8) were developed to enhance the sensitivity of the absorption and reflectivity

to small changes such as those due to the presence of a magnetic field. An externally applied periodic perturbation, such as an electric field, a stress, or a variation in temperature modulates the absorption or reflection of the material. To do so without perturbing the parameters to be measured is experimentally difficult. An interesting alternative to the experimental complexity of the modulated techniques is to study the spectral distribution of photo-effects in a magnetic field. Filion and Fortin (1.9) have studied the photoconductivity spectra of GaSb in intense magnetic fields and they obtained results comparable to or better than those published by Reine et al. (1.4) who used a stress modulated reflectivity technique. More recently, Rochon and Fortin (1.10) have reported magneto-optical structures observed in the spectral distribution of the photovoltaic effect in germanium. The broad aim of this research project is to develop and make use of yet another photo-effect technique the photoelectromagnetic (PEM) effect. The study also serves to investigate the PEM and associated Dember effect in quantizing magnetic fields.

The PEM effect was first reported in 1934 by K. Kikoin and M. Noskov (1.11) in Cu_2O. More recently, Zielinger (1.12) extensively studied the PEM effect in Cu_2O. The effect has had some practical applications in the area of detectors (1.13). The main advantage of a PEM detector is that it does not require any voltage bias. To date the most complete classical formulation for this effect remains that of W. van Roosbroeck (1.14) in 1956.

When a semiconductor crystal is placed in a magnetic field,

in a Voigt configuration and light ($h\nu > \varepsilon_g$) is shone on it, an electric potential develops at its boundaries. This effect, called the PEM effect, arises as a result of the Hall effect associated with the diffusion of optically injected carriers. The diffusion velocity of the excess carriers depends on their concentration gradient which in turn depends on the absorption coefficient. The PEM effect is thus expected to reflect the spectral distribution of the absorption coefficient in a semiconductor and can thus be used as a magneto-optical technique. The advantage of this technique over the photoconductivity technique is that it does not require a bias voltage which usually reduces the signal-to-noise ratio. As pointed out by Filion and Fortin (1.16) the PEM technique is also superior in that it depends directly on the absorption coefficient and does not require, as photoconductivity does, a surface-volume dependence of the photo-sensitivity.

An important aspect of this research project was to establish the PEM technique as an accurate and reliable method of magneto-optical investigation. In order to analyse the magneto-optical structures present in the PEM spectra it is necessary to have a theory which predicts the change in the direct interband magneto-optical transition energies with the magnetic field in terms of the relevant band parameters. In Chapter 3 we review the theoretical developments concerning the magneto-optical properties of a semiconductor. We first present the linear model of Luttinger and Kohn (1.16), and then the more complete formulation by Pidgeon and Brown (1.6) which takes into account the non-parabolicity effects of the conduction band. Since

the PEM technique is a direct method of investigation, a line shape study of the magneto-optical structures was necessary in order to relate the energy position of the structures to the interband transition energy.

Chapter 4 deals with some transport properties of semiconductors. The chapter includes a theoretical development explaining why the PEM effect and the associated Dember effect should reflect the magneto-absorption structures. We also study the influence of phonon-electron interactions on the spectral distribution of photoeffects in III - V compounds.

Two germanium crystals are extensively studied in section 5.1 of Chapter 5. The PEM technique is seen to yield band parameter values in excellent agreement with previously published experimental and theoretical values (1.3, 1.17). In section 5.2 and 5.3 of Chapter 5 the PEM technique is extended to the study of GaSb and InP respectively. The band parameter values found for GaSb are in better agreement with the theoretical predictions of Lawaetz (1.17) than those of Filion (1.9) and Reine (1.4). To the best of the author's knowledge no interband magneto-optical information had even been published for InP prior to this work. Both GaSb and InP are hetero-polar materials and under certain specific conditions they exhibited in the spectral distribution of the PEM effect the broader structures associated with phonon-electron interactions usually observed in photocon-

ductivity. By measuring the energy separations of these broader oscillations it was possible to evaluate the longitudinal optical (LO) phonon energy for these semiconductors.

In section 5.4 of Chapter 5 we investigate GaAs. Contrary to the previously studied materials, in GaAs the photoconductivity spectra exhibit better resolved magneto-optical structures than the PEM spectra. Some results obtained on a high resistivity GaAs sample are compared to those of Nahory (1.18) for an oxidized epitaxial GaAs sample. This gave us some insight on the mechanisms relating surface oxidation and impurity concentration with the observed spectral distribution of the photo-effects. Trapping is suspected to be a determining factor in the spectral character of the photo-effects.

2. EXPERIMENTAL METHOD

2.1 Apparatus

A schematic description of the apparatus necessary to study photo-effects in intense magnetic fields is given in Figure 2.1. The experimental set-up may be broken down into three parts; the optical set-up, the superconducting magnet and associated cryostat, and the synchronous detection system.

The optical set-up: The optical part of the apparatus consists of a Spex 1700-111, 3/4 meter, Czerny-Turner spectrometer. Either a Nernst filament or a quartz-iodine lamp was used as infrared source. Two 600 groves/mm gratings with their blaze at 0.75μ and 1.6μ respectively and, two low-pass filters at 0.652μ and 1.04μ used to cut off the second order radiation, complete the accessories of the spectrometer. The incoming radiation was chopped at either 85 Hz or 500 Hz and the outgoing radiation was polarized using HR Polaroid polarizers. Both slit openings were normally kept at 500μ, giving a resolution of 10Å or 1 meV at 1.2μ.

The superconducting magnet and associated cryostat: The monochromatic light emerging from the spectrometer was focussed on the samples installed in a Voigt configuration inside the magnet. The PEM effect only occurs in samples in a Voigt configuration. Figure 2.2 shows a top view of the sample holder. Two aluminum front surface mirrors are placed at 45° with respect to the incoming radiation.

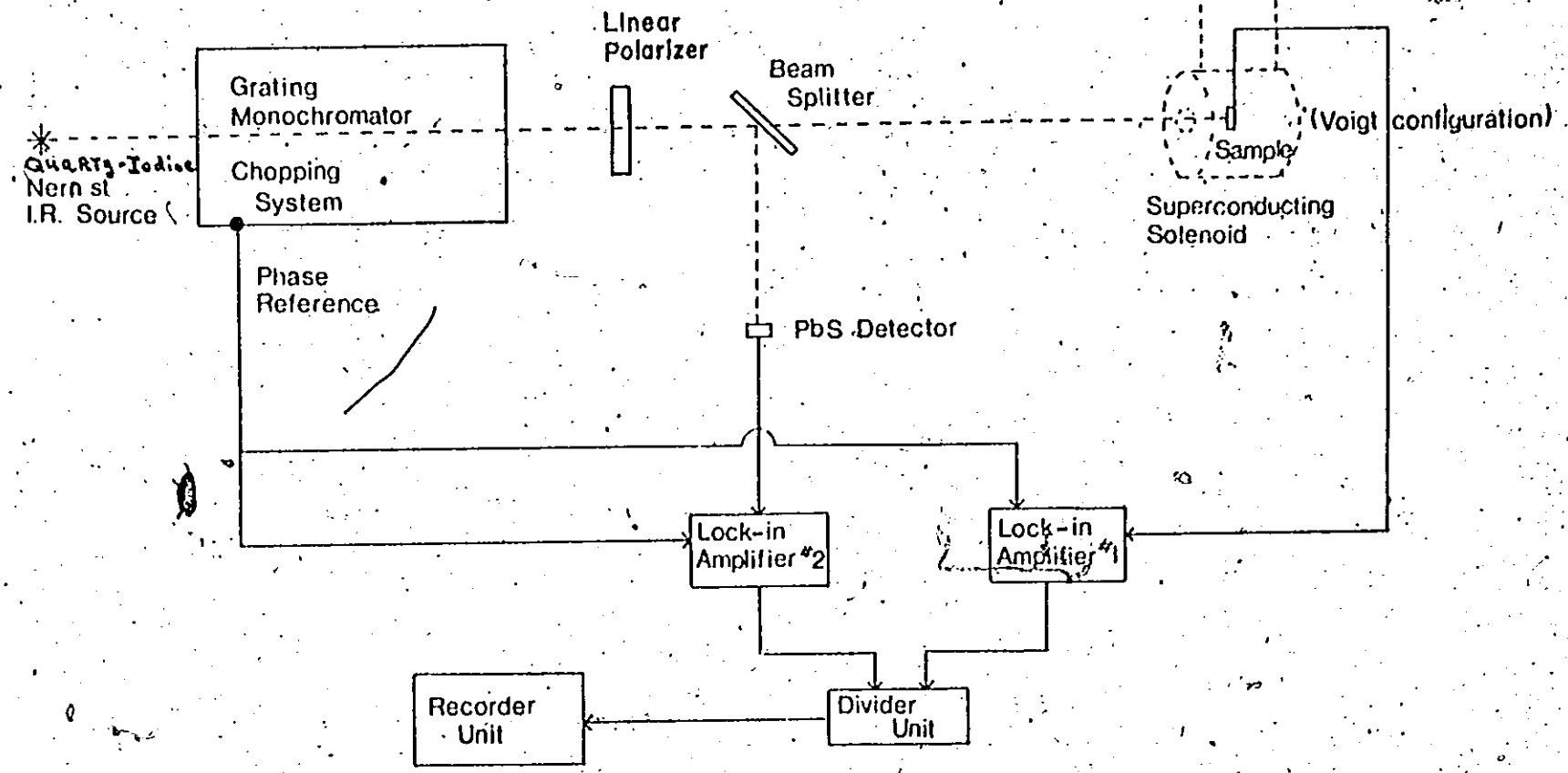

Figure 2.1:- A schematic description of the apparatus.

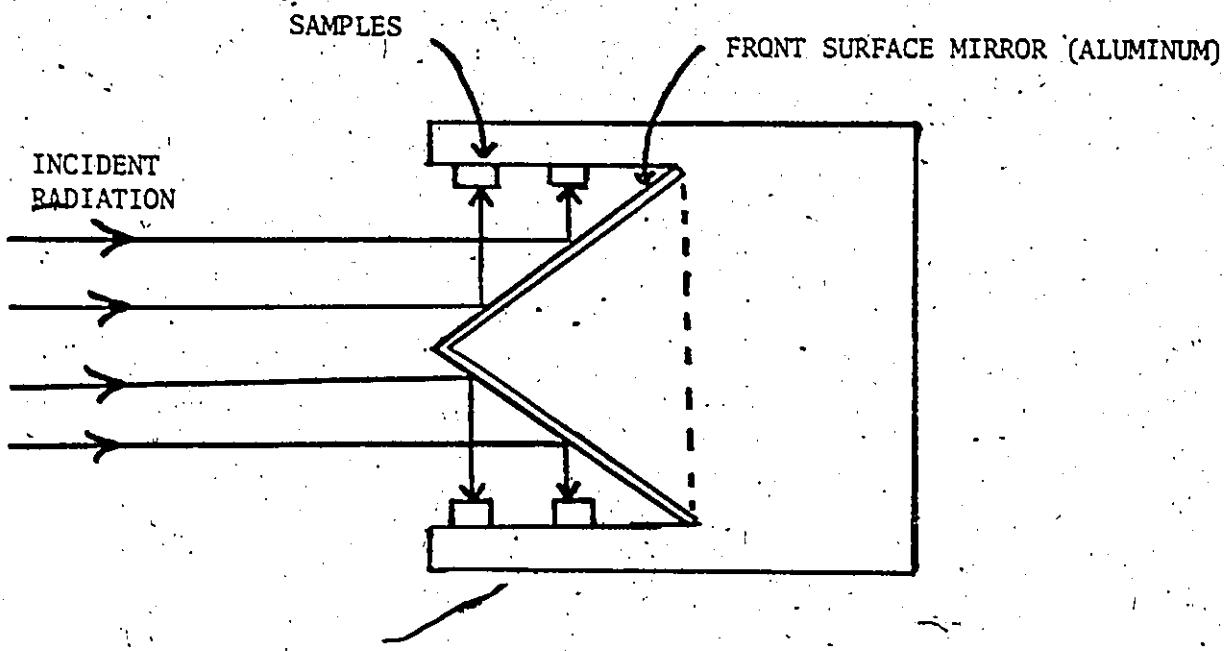

Figure 2.2: A description of the sample holder.

The four samples could then be installed perpendicular to both the incident radiation and the magnetic field. The lower part of the cryostat containing the magnet, the experimental chamber, and the sample holder is described in Figure 2.3, taken from Filion (2.1). The samples were kept at the surrounding liquid helium temperature by introducing approximately 10 mm Hg of helium gas in the experimental chamber. The infrared radiations reach the samples inside the magnet via two sealed quartz windows. The resulting photo-signal from the samples then leaves the experimental chamber the opposite way via ceramic feed-throughs.

The superconducting magnet was constructed by Ferranti Packard

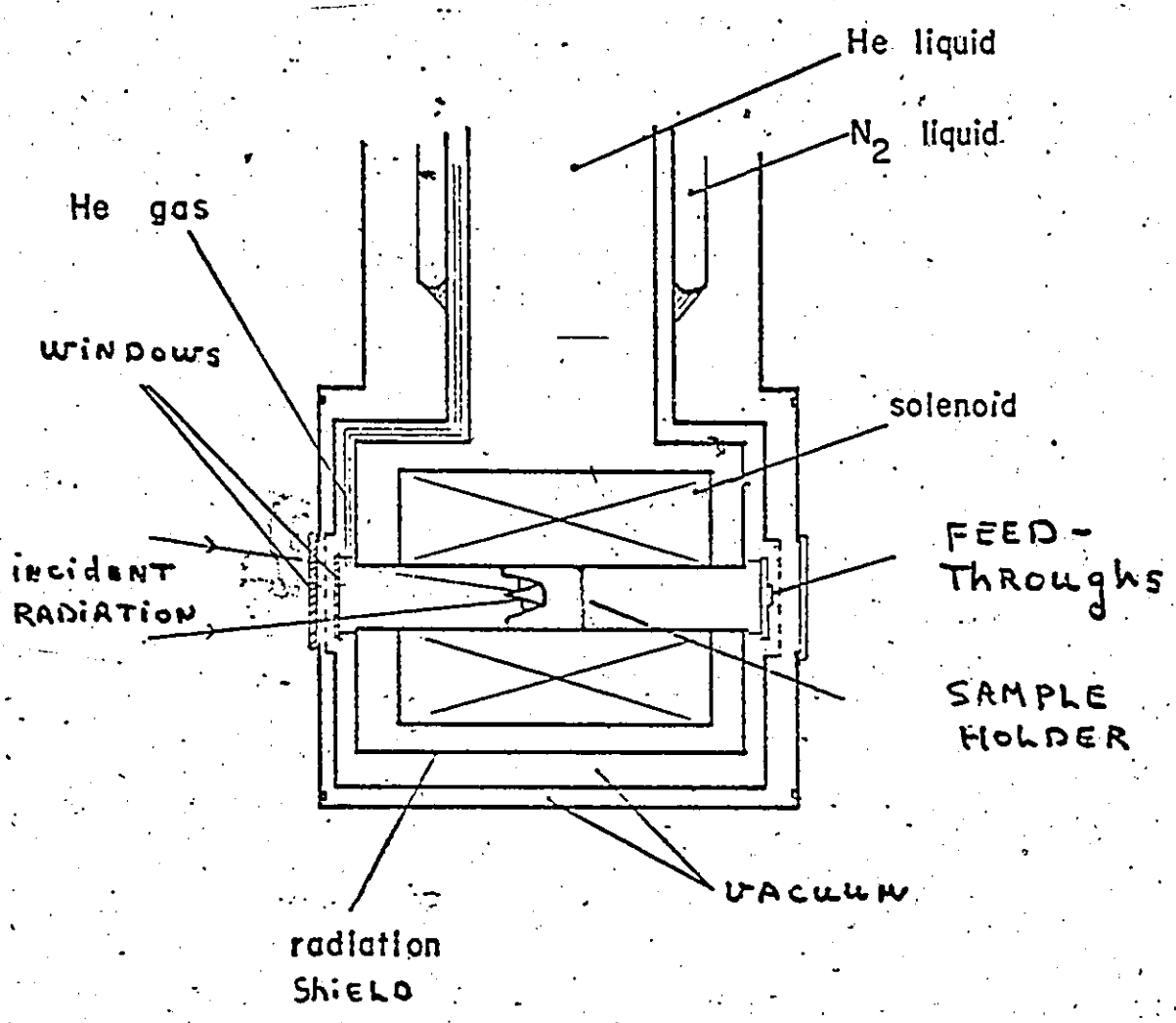

Figure 2.3: A description of the lower part of the cryostat containing the superconducting solenoid.

and installed in a Sulfrian cryostat. The solenoid is made with niobium titanium wire. It has a clear bore of 1.55 inches with an homogeneity of 1% over a 1 inch d.s.v. at its center. The critical current is 51 Amperes allowing fields of up to 72.5 kG. Figure 2.4, also taken from Filion (2.1), schematically describes the current supply and control for the superconducting solenoid.

The synchronous detection system: The photo-signal of the sample was fed into a first Lock-In Amplifier, a PAR model 220. Using a beam splitter, a 10% portion of the infrared radiation was deflected onto a PbS detector and its signal was fed to a second Lock-In Amplifier, a PAR model 122. The division of the first signal by the second corrected for variations in intensity of the light incident on the samples. The resulting signal was finally recorded on a Honeywell Recording Unit.

In order to maximize the signal-to-noise ratio without loosing any information, the electronic time constant had to be matched with the scanning speed and the slit opening i.e., the resolution. For example, an electronic time constant of approximately 3 seconds necessitates a 10Å resolution with a 3Å/sec scanning speed. The average signal-to-noise ratio of the photo-signals recorded was always > 10.

The impedance of the high purity samples at low temperatures was in excess of 100 Meg and the input impedance of the Lock-In is only 10 Meg. In the case of a PEM signal, to a good approximation this means that a short-circuit current is measured. This information

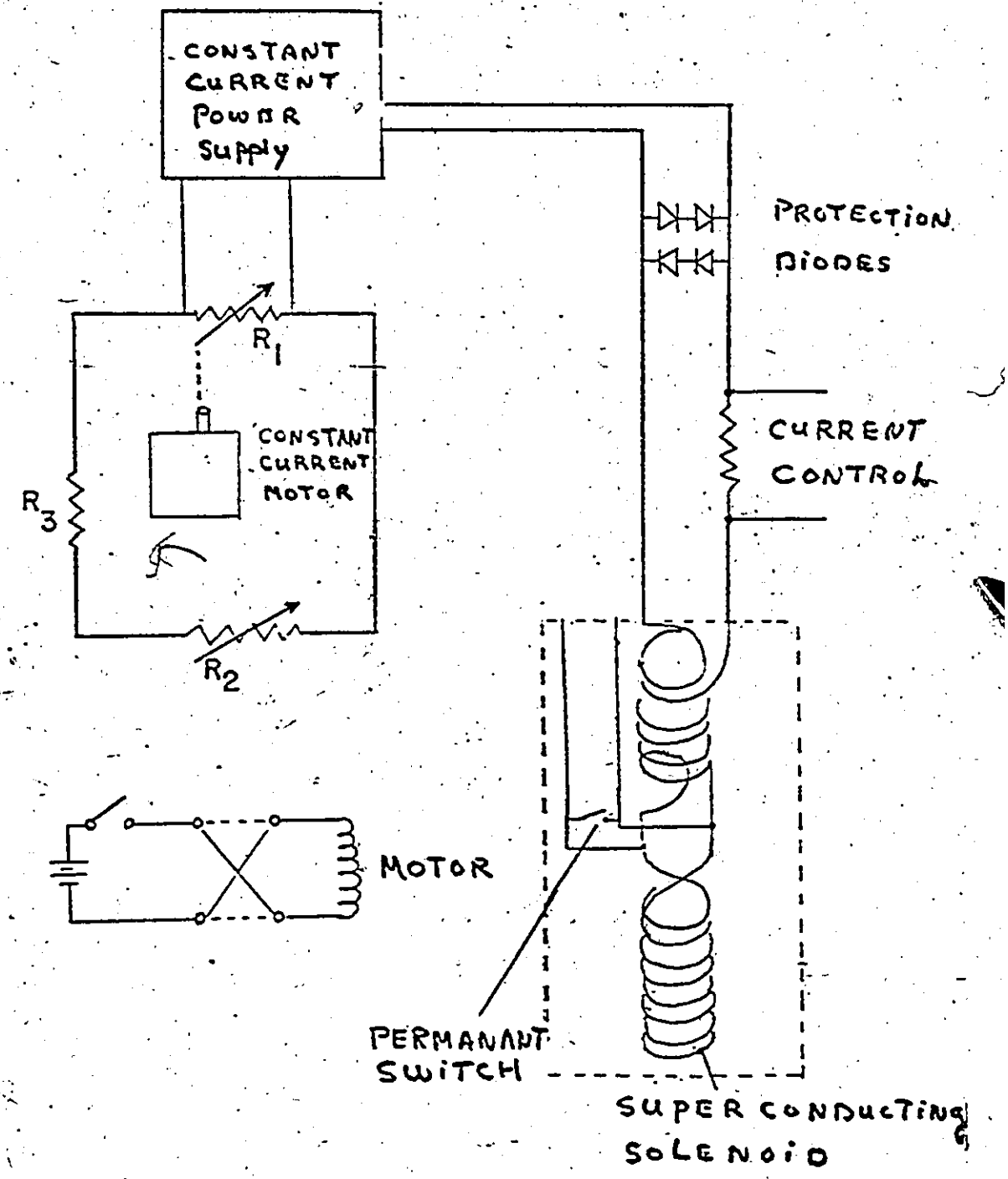

Figure 2.4: A schematic description of the power supply and control for the superconducting solenoid.

will become useful when developing theoretical expressions for the PEM signal.

2.2 Sample preparation

The surface preparation of the samples represent an important aspect of this research project. Because of the long process of trial and error involved in surface preparation we estimate that over one hundred samples were prepared during the course of this work. Only ten of these samples were fully investigated and they will be described later in this section.

The first step in sample preparation is the cutting of the samples into parallelepipeds of approximately 1 x 2 x 10 mm. The crystal axes are then determined so that the [111] direction be oriented parallel to the magnetic field. A mechanical lapping of the surfaces follows using 5 micron Al_2O_3 powder. Next the samples are chemically etched: the various etches used are given in Table 2.1.

Table 2.1

Etch	Chemical Components
CP-8	$3HF$, $5HNO_3$, $3CH_3COOH$
10% Br	$1Br_2$, $10CH_3OH$
RT-1	$2H_2SO_4$, $1H_2O_2$, $2H_2O$
RT-2	$20H_2SO_4$, $1H_2O_2$, $1H_2O$

The normal exposure time to air necessary for the installation of the samples usually sufficed to oxidize their surface. Otherwise, oxidation of the surface can easily be achieved by heating the sample in air. Preventing unwanted surface oxidation is a more difficult task. The coating of the surfaces by a pyrolytic deposition of an Al_2O_3 film (2.2) revealed itself an excellent solution to the problem of preserving clean surfaces. The deposition apparatus is shown in Figure 2.5. The temperature inside the deposition chamber is first raised to 520°C in the presence of a circulating reducing gas, 10% hydrogen and 90% nitrogen, and then lowered to 420°C. The aluminum tri-isopropoxide $[Al(OC_3H_7)_3]$ is heated by an oil bath to 140°C and a transport gas, nitrogen, carries the emanating vapors to the pyrolyzing region over the specimen, where they decompose and deposit the oxide film.

Finally, the contacts consist of indium drops, 0.5mm in diameter, alloyed to the sample with gold wires attached to them. Between preparation and installation the samples were kept in an evacuated chamber.

The ten samples studied are labelled and described in Table 2.2. With the exception of the GaAs samples these are all single crystal samples and they were all installed with their [111] direction parallel to the magnetic field.

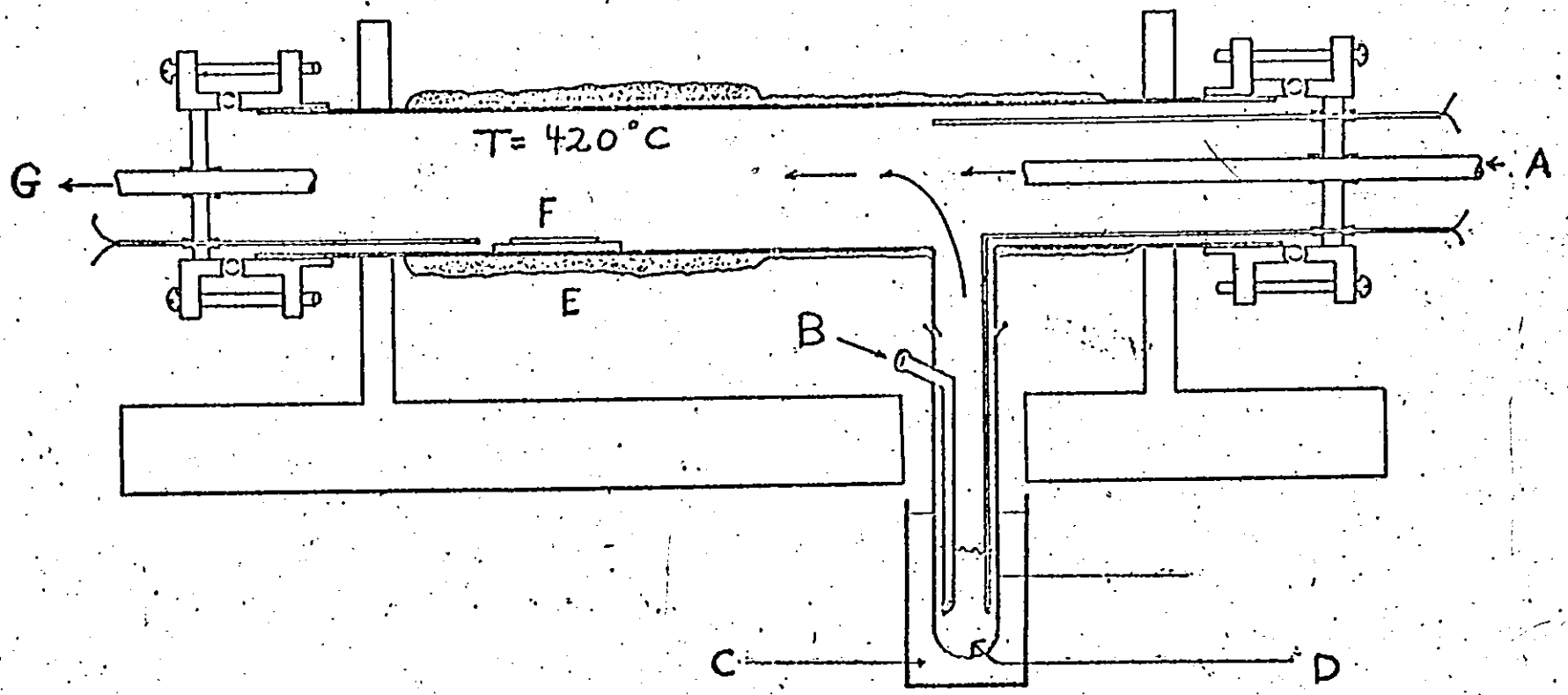

Figure 2.5: A description of the apparatus for the deposition of Al_2O_3 films.

A, B, dry N_2; C, constant temperature (140°C) oil bath; D, aluminum tri-isopropoxide; E, heating element; F, substrate holder; G, exhaust.

Table 2.2

Sample	ρ Ω-cm	μ $\frac{cm^2}{volt\text{-}sec}$	Impurity concentration cm^{-3}	Chemical etch	Contact alloy	Surface Treatment
Ge(M)	47 [1]		4×10^{12} [1]	CP-8	In at 410°C	none
Ge(N)	45			CP-8	In at 410°C	none
Ge(M2)	47 [1]		4×10^{12} [1]	CP-8	In at 410°C	Al_2O_3 coating
Ge(M3)				CP-8	In at 410°C	Irradiated with neutrons
GaSb(1)	0.0412 [2]	670 [2]	2.5×10^{17} [2]	CP-8	In at 410°C	none
GaSb(2)	0.0412 [2]	670 [2]	2.5×10^{17} [2]	Cp-8	In at 410°C	Heated to 150°C in air for 2 minutes
InP(1)	0.7 [3]	4,400 [3]	2×10^{15} [3]	10% Br	In at 520°C	Al_2O_3 coating
InP(2)	0.7 [3]	4,400 [3]	2×10^{15} [3]	10% Br	In at 520°C	none
GaAs(1)		202,000 at 77K [4]	1.4×10^{12} [4]	RT-2 [4]	SnIn	Al_2O_3 coating
GaAs(2)	2×10^{7} [2]	2,000-4,200 [5]		RT-1	In at 520°C	Al_2O_3 coating

All Ge and GaSb samples were p-type. The other samples were not measured.

(1) Dr. H. Pullan, Ontario Research Foundation
(2) Monsanto, St.Louis (U.S.A.)
(3) Semimetals, Inc., Allendale, N.J. (U.S.A.)
(4) Dr. D. L. Rode, Bell Laboratories, Murray Hill, N.J. (U.S.A.)
(5) F. Prat, Master's Thesis, University of Ottawa.

3. MAGNETO-OPTICAL PROPERTIES

3.1 Direct Interband Transitions in a Magnetic Field

3.1.1 A simple two-band model

3.1.2 The treatment by Luttinger and Kohn

3.1.3 The Pidgeon and Brown scheme

3.1.4 A method of analysis using the Pidgeon and Brown scheme

3.1.5 The selection rules

3.2 Absorption Coefficient for a Semiconductor in a Magnetic Field

3.2.1 Direct interband magneto-absorption

3.2.2 A line shape study of the absorption structures.

3. MAGNETO-OPTICAL PROPERTIES

In this chapter we begin by reviewing some of the more fundamental theoretical developments concerning the direct magneto-optical interband transitions in a semiconductor. The theoretical results presented will prove essential to the proper analysis of the magneto-optical spectra. In order to adequately interpret these spectra, it also became necessary to investigate the line shape of the predicted absorption structures.

3.1 Direct Interband Transitions in a Magnetic Field

In this first section we describe how the valence and conduction bands of a semiconductor split up under the influence of magnetic field into sub-bands called Landau levels. A simple two-band model is used to introduce this phenomenon. In the case of degenerate valence bands the task of evaluating the energy position of the Landau levels becomes more difficult. Luttinger and Kohn (3.1) were the first to solve this problem and we present their results. Their solution for the interband transition energies between the levels vary linearly with the magnetic field. A rapid inspection of our experimental results should satisfy the reader that this theory fails at higher magnetic fields. Having encountered the same problem in indium antimonide, Pidgeon and Brown (3.2) overcome this difficulty by including in their calculation of the transition energies the non-parabolicity effects of the conduction band. Here again we shall

present their results. The above theoretical developments enable us to evaluate the band parameters that will best fit our experimental data. The iterative process employed to achieve such a fit is fully described. We conclude this section by giving the selection rules which govern the direct interband transitions between the levels.

3.1.1 A simple two band model

In the vicinity of $\bar{k} = 0$ the energy momentum relations for a simple two-band model are given by:

$$\varepsilon_c = \varepsilon_g + (\hbar^2 k^2/2m_c) \qquad 3.1$$

$$\varepsilon_v = -(\hbar^2 k^2/2m_v) \qquad 3.2$$

where the indices c and v denote the conduction and valence band respectively, m_c and m_v for the electron and hole effective mass and ε_g for the energy gap between the two bands at $\bar{k} = 0$.

The Hamiltonian for the motion of a free electron (neglecting spin) in a magnetic field is:

$$\mathcal{H} = [\bar{P} + (e/c)\,\bar{A}\,]^2/2m \qquad 3.3$$

where

$\bar{P} = \hbar\bar{\nabla}/i$ is the momentum operator,

$\bar{A}$, is the vector potential of the dc magnetic field, and

m, the free electron mass.

For a conduction band electron the Hamiltonian is simply that of the free electron plus the periodic potential energy $V(\bar{r})$ of the electron

in the crystal. The effective mass approximation accounts for this periodic potential energy and the Hamiltonian for the conduction band electron may be expressed as:

$$\mathcal{H} = [\bar{P} + (e/c)\ \bar{A}\ ]^2/2m_c \qquad 3.4$$

where the conduction band effective mass m_c now replaces the free electron mass m.

The conduction electron wave functions are:

$$\psi(\bar{r}) = \mu_c(\bar{r})\ f_c(\bar{r}) \qquad 3.5$$

where $\mu_c(\bar{r})$ is the periodic part of the Bloch functions for $\bar{k} = 0$ and $f_c(r)$ is a slowly varying function of position compared to the Bloch functions. From the solution of the following Schrodinger-like equation:

$$[\bar{P} + (e/c)\ \bar{A}\ ]^2\ f_c(\bar{r})/2m_c = (\varepsilon_c - \varepsilon_g)\ f_c(\bar{r}) \qquad 3.6$$

one obtains the following eigenvalues for the conduction band electron:

$$\varepsilon_c(n) = \varepsilon_g + (n + \tfrac{1}{2})\hbar\omega_c + (\hbar^2 k_z^2/2m_c) \qquad 3.7$$

where n (> 0) is the magnetic quantum number and:

$$\omega_c = e\,H/cm_c \qquad 3.8$$

is the cyclotron frequency of the electrons in the conduction band. In a similar fashion one obtains for the holes in the valence band:

$$\varepsilon_v(n) = -[(n + \tfrac{1}{2})\hbar\omega_v + (\hbar^2 k_z^2/2m_v)] \qquad 3.9$$

Figure 3.1 illustrates how the valence and conduction band split up under the influence of a magnetic field.

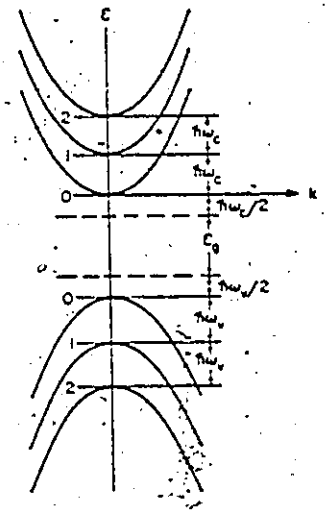

Figure 3.1: Energy levels for a simple two-band model in a magnetic field.

Equations (3.7) and (3.9), first obtained by Landau (3.3), contain a very important result, namely, that the applied magnetic field splits the three dimensional conduction band into a series of two-dimensional harmonic oscillator-like levels separated by an energy, $\hbar\omega$. This produces a ladder of one-dimensional sub-bands known as the Landau levels. The next two sub-sections deal with the problem of calculating the energy position of these levels in germanium and III-V compounds.

3.1.2 The treatment by Luttinger and Kohn

Luttinger and Kohn (3.1) were the first to calculate the energy positions of the Landau levels for the more complicated case of degenerate valence bands which characterize germanium and III - V compounds. These materials all have, in the vicinity of $\bar{k} = 0$ $\varepsilon(\bar{k})$ versus $\bar{k}$, curves similar to those shown in Figure 3.2

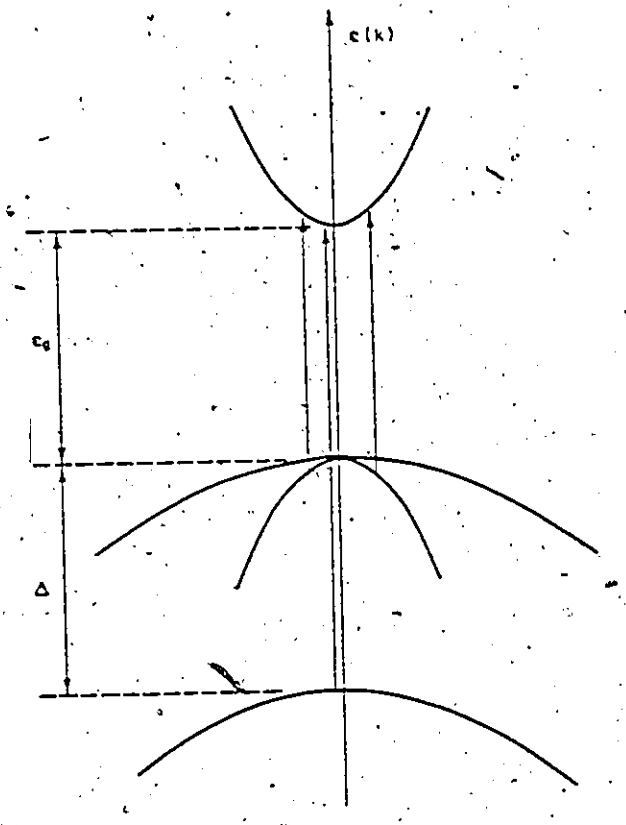

Figure 3.2: A schematic of the $\varepsilon(\bar{k})$ versus $\bar{k}$ curves in the vicinity of k=0 for the conduction and valence bands of III - V compounds.

The conduction band is similar to the one considered in the simple two-band model. On the other hand the valence band is degenerate at $\bar{k} = 0$ and at an energy Δ below which point lies the spin orbit split-off

valence band extremum. The three valence bands belong to a p-like atomic orbital, whereas the conduction band is s-like. In the presence of a magnetic field both the spin degeneracy and the degeneracy at $\bar{k} = 0$ are lifted resulting in eight Landau level ladders.

The light- and heavy-hole valence band ladders are labelled a^+, a^-, b^+, b^-. Two quantum pair numbers characterize these ladders, (M_J, n) and $(M_J + 2, n - 2)$, where M_J denotes the total magnetic quantum number and n the Landau quantum number. Depending on whether the levels are denoted by n or by n - 2, the $a^{\pm}$ ladders have $M_J = -\frac{1}{2}$ or $+\frac{3}{2}$ and the $b^{\pm}$ ladders have $M_J = -\frac{3}{2}$ or $+\frac{1}{2}$. The two conduction band ladders are denoted a^c and b^c. For an s-like band the total magnetic quantum number of the levels is equal to the spin magnetic quantum number. Consequently, $M_J = M_S = \pm\frac{1}{2}$ for the conduction band with $M_J = +\frac{1}{2}$ for the a^c ladder and $M_J = -\frac{1}{2}$ for the b^c ladder. Finally the split-off band ladders are denoted a^s and b^s with $M_J = -\frac{1}{2}$ for the a^s ladder and $M_J = +\frac{1}{2}$ for the b^s ladder.

Luttinger and Kohn calculate in units of $s = \frac{\hbar eH}{mc}$ the energy position of the Landau levels for the degenerate valence bands. Their solutions are expressed as functions of the following parameters: γ_1^L, γ_2^L and γ_3^L, called Luttinger's parameters. These may be related to Kittel's parameters A, B and C in the following manner:

$$\gamma_1^L = A; \quad \gamma_2^L = -B/2; \quad \gamma_3^L = \tfrac{1}{2}\left[C^2/3 + B^2\right]^{\frac{1}{2}} \qquad 3.10$$

where the constant energy surfaces of the degenerate valence bands is

given by:

$$\varepsilon(\bar{k}) = -\frac{\hbar^2}{2m}\{Ak^2 \pm [B^2k^4 + C^2[k_y^2k_z^2 + k_x^2k_y^2 + k_x^2k_y^2]]^{\frac{1}{2}}\} \qquad 3.11$$

In the Pidgeon and Brown numbering system, the expression for the energy positions of the Landau levels are for the a^+ and a^- ladders:

$$\varepsilon_a^+(-1) = -\tfrac{1}{2}(\gamma_1^L - \gamma'^L - k^L)$$

$$\varepsilon_a^+(0) = -\tfrac{1}{2}(3\gamma_1^L - 3\gamma'^L - k^L)$$

$$\varepsilon_a^{\pm}(n) = -[(n+\tfrac{1}{2})\gamma_1^L - \gamma'^L + \tfrac{1}{2}k^L] \mp [\{(n+\tfrac{1}{2})\gamma'^L - \gamma_1^L + k^L\}^2 + 3n(n+1)(\gamma''^L)^2]^{\frac{1}{2}} \qquad 3.12$$

where n = 1, 2, 3 ---; and similarly for the b^+ and b^- ladders:

$$\varepsilon_b^+(-1) = -\frac{1}{2}(\gamma_1^L + \gamma'^L - 3k^L)$$

$$\varepsilon_b^+(0) = -\frac{3}{2}(\gamma_1^L + \gamma'^L - k^L)$$

$$\varepsilon_b^{\pm}(n) = -[(n+\tfrac{1}{2})\gamma_1^L + \gamma'^L - \tfrac{1}{2}k^L] \mp [\{(n+\tfrac{1}{2})\gamma'^L + \gamma_1^L - k^L\}^2 + 3n(n+1)(\gamma''^L)^2]^{\frac{1}{2}} \qquad 3.13$$

where n = 1, 2, 3 ---; and where

$$\gamma'^{L} = \gamma_3^L - (\gamma_3^L - \gamma_2^L)f(\theta) \qquad 3.14$$

$$\gamma''^{L} = \gamma_3^L - \frac{1}{3}(\gamma_3^L - \gamma_2^L)[1 + f(\theta)] \qquad 3.15$$

$$f(\theta) = \frac{1}{4}(3\cos^2\theta - 1)^2 \qquad 3.16$$

with θ as the angle between the magnetic field direction and the z-axis (the [001] direction) in the $(1\bar{1}0)$ plane. The parameter k^L is exclusive to the magnetic field problem and plays the role of a g-factor

$$k^L = \gamma_3^L + \frac{2}{3}\gamma_2^L - \frac{1}{3}\gamma_1^L - \frac{2}{3} \qquad 3.17$$

As the Landau quantum number n increases the energy separation of the Landau levels tends to $s(m/m_{lh})$ for the light-hole ladders and to $s(m/m_{hh})$ for the heavy-hole ladders where m_{lh} and m_{hh} denote the effective masses at the top of the light- and heavy-hole bands respectively. For the limit of large n values Roth [3.4] deduces from equation (3.12) and (3.13) that:

$$\left.\begin{matrix} m/m_{lh} \\ m/m_{hh} \end{matrix}\right\} = \gamma_1^L \pm [(\gamma'^{L})^2 + 3(\gamma''^{L})^2]^{\frac{1}{2}} \qquad 3.18$$

Therefore the energy separation of the Landau levels for the valence band ladders becomes uniform as n increases. This is also true for the

conduction band ladders where the energy position of the Landau levels is given (in units of s) by the following expression:

$$\varepsilon^{c}_{a,b} = m/m_c(n + \tfrac{1}{2}) + g_c M_{J/2} \qquad 3.19$$

$$\text{where } m/m_c = 1 + E_{p/3}\left[2/\varepsilon_g + \frac{1}{\varepsilon_g + \Delta}\right] \qquad 3.20$$

$$\text{and } g_c = 2\left[1 - E_p/3\left[1/\varepsilon_g - \frac{1}{\varepsilon_g - \Delta}\right]\right] \qquad 3.21$$

g_c being the effective spectroscopic splitting factor and E_p the conduction band interaction energy defined by Kane [3.5]. The higher direct interband transition energies are therefore expected to be equally spaced. Our experimental results verify this prediction, however, the same results do not verify the linear dependence of the transition energies on the magnetic field as predicted by the theory of Luttinger and Kohn.

In the next sub-section we describe how Pidgeon and Brown [3.2] partially account for this discrepancy by including in the expressions for the energy position of the Landau levels the effects of the non-parabolicity of the conduction band.

3.1.3 The Pidgeon and Brown scheme

In their calculation of the energy position of the Landau levels Pidgeon and Brown include the non-parabolicity effects of the bands by treating the eight bands as being all nearly degenerate. The energy positions are solutions to an 8x8 eigenvalue problem.

By changing the basis function the eigenvalue matrix can be factored in two 4x4 symmetric matrices of the following form:

$$\begin{bmatrix} s M_1 - \varepsilon_g - \varepsilon & \sqrt{s}\, M_2 & \sqrt{s}\, M_4 & \sqrt{s}\, M_7 \\ \sqrt{s}\, M_2 & -s M_3 - \varepsilon & s M_5 & s M_8 \\ \sqrt{s}\, M_3 & s M_5 & s M_6 - \varepsilon & s M_9 \\ \sqrt{s}\, M_7 & s M_8 & s M_9 & s M_{10} + \Delta - \varepsilon \end{bmatrix} \qquad 3.22$$

The matrix elements are given in Table 3.1. The "a-matrix" gives the energy position of the levels for the a^c, $a^{\pm}$ and a^s ladders while the "b-matrix" gives the energy position of the levels for the b^c, $b^{\pm}$ and b^s ladders. Eight parameters define these elements: ε_g, Δ, E_p, $F = f(\hbar^2/m)$ a matrix element representing the interaction of the conduction band with higher lying bands, $\gamma_1 = \gamma_1^L - T$, $\gamma' = \gamma'^L - T$, $\gamma'' = \gamma''^L - T$, and $k = k^L - T$ where $T = E_p/6\varepsilon_g$. Unfortunately, no suitable analytical form exists for the solution of these matrices and they must be solved numerically.

The solutions ε for the two symmetric matrices given in equation (3.22) can be expanded in a power series in s as follows:

$$\varepsilon = \varepsilon_0 + \varepsilon_1 s + \varepsilon_2 s^2 + \varepsilon_3 s^3 + \ldots \qquad 3.23$$

By substiting this expansion in the determinant equation of the two

Table 3.1: Matrix elements for the two symmetric 4 x 4 Pidgeon and Brown matrices.

M_1	$m + 1 + 2f\,(m+\frac{1}{2})$	$m + 2f\,(m+\frac{1}{2})$
M_2	$\left[\frac{1}{2} m E_P\right]^{1/2}$	$\left[\frac{1}{6} m E_P\right]^{1/2}$
M_3	$-(\gamma_1+\gamma')(m-\frac{1}{2}) - \frac{3}{2}\kappa$	$-(\gamma_1-\gamma')(m-\frac{1}{2}) - \frac{1}{2}\kappa$
M_4	$\left[\frac{1}{6}(m+1) E_P\right]^{1/2}$	$\left[\frac{1}{2}(m+1) E_P\right]^{1/2}$
M_5	$-\left[3(m+1)m\right]^{1/2}\gamma''$	$-\left[3(m+1)m\right]^{1/2}\gamma''$
M_6	$-(\gamma_1-\gamma')(m+\frac{3}{2}) + \frac{1}{2}\kappa$	$-(\gamma_1+\gamma')(m+\frac{3}{2}) + \frac{3}{2}\kappa$
M_7	$\left[\frac{1}{3}(m+1) E_P\right]^{1/2}$	$\left[\frac{1}{3} m E_P\right]^{1/2}$
M_8	$\left[6(m+1)m\right]^{1/2}\gamma''$	$-\sqrt{2}\left[\gamma'(m-\frac{1}{2}) + \frac{\kappa+1}{2}\right]$
M_9	$-\sqrt{2}\left[\gamma'(m+\frac{3}{2}) - \frac{\kappa+1}{2}\right]$	$-\left[6(m+1)m\right]^{1/2}\gamma''$
M_{10}	$-\gamma_1(m+\frac{3}{2}) + \kappa + \frac{1}{2}$	$-\gamma_1(m-\frac{1}{2}) - \kappa - \frac{1}{2}$

matrices and regrouping the terms containing equal powers of s, equations for the expansion coefficients ε_0, ε_1, ε_2 ...etc may be obtained. The equation for the zeroeth order in s is then:

$$(\varepsilon_0 - \varepsilon_g)\varepsilon_0^2(\varepsilon_0 + \Delta) = 0 \qquad 3.24$$

which has four solutions $\varepsilon_0 = \varepsilon_g$, 0, 0, $-\Delta$ corresponding to the zero field band edges. The equation for the first order in s is:

$$[(\varepsilon_0 - \varepsilon_g) + (\varepsilon_0 + \Delta)]\varepsilon_0^2\varepsilon_1 = \varepsilon_0^2[M_1(\varepsilon_0 + \Delta) + M_{10}(\varepsilon_0 - \varepsilon_g) + M_7^2]$$
$$+ \varepsilon_0(M_2^2 + M_4^2)(\varepsilon_0 + \Delta) \qquad 3.25$$

The expansion coefficient ε_1^c for the conduction band is obtained by letting $\varepsilon_0 = \varepsilon_g$. The result is the same as that given in equation (3.19) except for the additional term 2f added to the effective mass ratio m_c/m. By letting $\varepsilon_0 = -\Delta$ one obtains the expansion coefficient ε_1^s for the split-off band. The common factor ε_0 in equation (3.25) implies that for the light- and heavy-hole bands where $\varepsilon_0 = 0$, no solution exists. Therefore it is necessary to go to the next highest order in s to find a solution for the ε_1 expansion coefficients of the two valence bands. As expected, the coefficients $\varepsilon_{a,1}^{\pm}$ and $\varepsilon_{b,1}^{\pm}$ are exactly those calculated by Luttinger and Kohn; equations (3.12) and (3.13). As can be seen from equation (3.23) the ε_2 expansion coefficients will reflect the second order dependence for the energy position of the Landau levels on the magnetic field. Because of the complexity of these coefficients no expressions are given for the

valence band coefficients and Aggarwal [3.6] only gives an approximate expression for the conduction band coefficient ε_2^c:

$$\varepsilon_2^c = \frac{(n + \frac{1}{2})^2}{\varepsilon_g} (m/m_c - 1) \left[\frac{3\varepsilon_g^2 + 4\Delta\varepsilon_g + 2\Delta^2}{(\varepsilon_g + \Delta)(3\varepsilon_g + 2\Delta)} \left(\frac{m}{m_c} + \gamma_1\right) + 2\gamma_3 \right] \qquad 3.26$$

Given the above expressions for the expansion coefficients, the power series expression describing the energy position of the Landau levels can now be used to calculate the band parameters that best fit the experimental data. Next we will present the iterative process used in the evaluation of the band parameters.

3.1.4 A method of analysis using the Pidgeon and Brown scheme

The Pidgeon and Brown approach uses eleven parameters in calculating the energy positions of the Landau levels. These parameters are: m_c, γ_1^L, γ_2^L, γ_3^L, k^L, f, ε_g, Δ, H, n and the orientation of the crystal in the magnetic field. Using equation (3.17), k^L may be expressed in terms of Luttinger's parameters. The term f, the spin orbit splitting energy Δ, as well as the small difference $\gamma_3^L - \gamma_2^L$ can be predetermined using published values. The direct bandgap energy ε_g is obtained from the zero field convergence of the experimental interband transition energies. Finally, the orientation of the crystal in the magnetic field is predetermined experimentally. This leaves five adjustable parameters: m_c, γ_1^L, γ_3^L, H, n. The interband

energies can therefore be expressed as follows:

$$\epsilon_n = f(\alpha_m, H, n) \qquad 3.27$$

where m = 1, 2, 3

and $\alpha_1 = m_c$; $\alpha_2 = \gamma_1^L$; $\alpha_3 = \gamma_3^L$.

The parameters α_m can be written as:

$$\alpha_m = \alpha_m^0 + a_m \qquad 3.28$$

where α_m^0's are approximately correct initial values and a_m's are presumably small corrections to these values. The new function:

$$\epsilon_n = f(\alpha_m^0 + a_m, H, n) \qquad 3.29$$

can be expanded in a Taylor series about α_m^0's as follows:

$$f(\alpha_m, H, n) \simeq f(\alpha_m^0, H, n) + \sum_{\ell=1}^{3} F_\ell(\alpha_m^0, H, n)a_\ell \qquad 3.30$$

where $$F_\ell(\alpha_m^0, H, n) = \left.\frac{\partial f(\alpha_m, H, n)}{\partial \alpha_\ell}\right|_{\alpha_m^0} \qquad 3.31$$

The sum of the square of the deviations between the theoretical transition energy and the experimental energy will be:

$$D = \sum_i [\epsilon_i - f(\alpha_m, H_i, n)]^2 \qquad 3.32$$

The purpose of the exercise is to minimize D with respect to the

corrections a_ℓ. The conditions are:

$$\frac{\partial D}{\partial a_\ell} = 0; \ \ell = 1, 2, 3 \qquad 3.33$$

This produces a set of three simultaneous linear homogeneous equations for the three corrections a_m:

$$\sum_{\ell=1}^{3} A_{m\ell} a_\ell = B_m; \ m = 1, 2, 3 \qquad 3.34$$

where $$A_{m\ell} = \sum_i^N F_m(\alpha_m^0, H_i, n) F_\ell(\alpha_m^0, H_i, n) \qquad 3.35$$

and $$B_m = \sum_i^N F_m(\alpha_m^0, H_i, n)[\varepsilon_i - f(\alpha_m, H_i, n)] \qquad 3.36$$

The iteration process consists in using those last coefficients $A_{m\ell}$ and B_m to evaluate a set of corrections a_m; the new parameters $\alpha_m = \alpha_m^0 + a_m$ can then be used to find a second, presumably smaller, set of corrections and so on. The iterative process is expected to converge to a lower limit of D giving us a set of parameters α_m offering the best possible fit. Associated to these parameters, a root mean square deviation for the experimental points will be given by:

$$D_{r.m.s.} = \frac{1}{N}\left\{\sum_i^N [\varepsilon_i - f(\alpha_m, H_i, n)]^2\right\}^{\frac{1}{2}} \qquad 3.37$$

where N is the total number of experimental points. This last expression measures the ability of the parameters α_m to reproduce

the experimental results.

The above iterative process can only be operational if the experimental points are properly identified, that is, if the initial and final states of the observed transitions are known. The task of identifying the experimental points is greatly simplified by the existence of selection rules governing the interband transitions. These selection rules will be presented next.

3.1.5 The selection rules

Figure 3.3 schematically summarizes the theoretical predictions for the energy positions of the Landau levels. The figure also indicates the allowed interband transitions between the Landau levels. In the Faraday configuration, where the electric vector $\vec{E}$ of the incident radiation is always perpendicular to the magnetic field $\vec{B}$, the allowed transitions are:

$$a^{\pm}(n') \rightarrow a^{c}(n)$$
$$b^{\pm}(n') \rightarrow b^{c}(n) \qquad 3.38$$

where Δn and $\Delta M_J = +1$ for the left circularly polarized light and where Δn and $\Delta M_J = -1$ for the right circularly polarized light. The above transitions are also allowed in the Voigt configuration provided the electric vector $\vec{E}$ is still perpendicular to the magnetic field $\vec{B}$. In the latter case however, the two circularly polarized modes cannot be physically differentiated. Nevertheless, the Voigt configuration

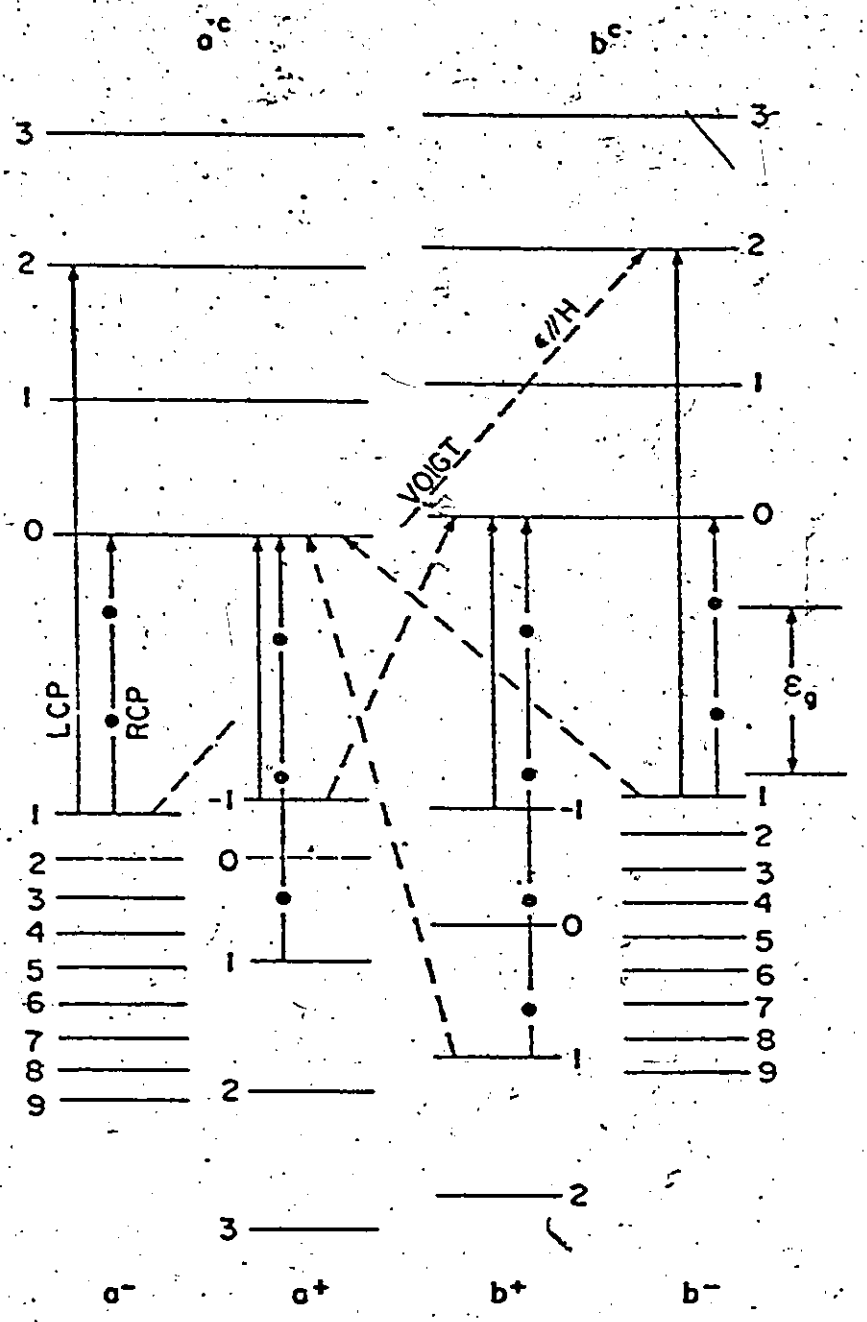

Figure 3.3: The Landau levels for the conduction band and light- and heavy-hole bands (in the Pidgeon and Brown numbering system). The arrows represent the lowest energy interband transitions: the solid arrows for the E // B right circular polarization, the dotted arrows for the E // B left circular and the dashed arrows for the E ⊥ B polarization.

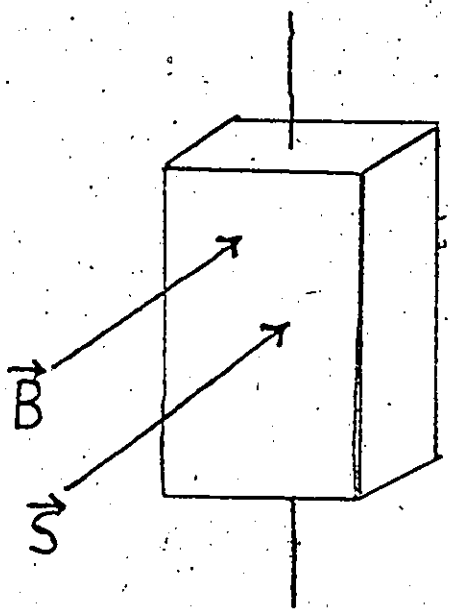

Faraday Configuration

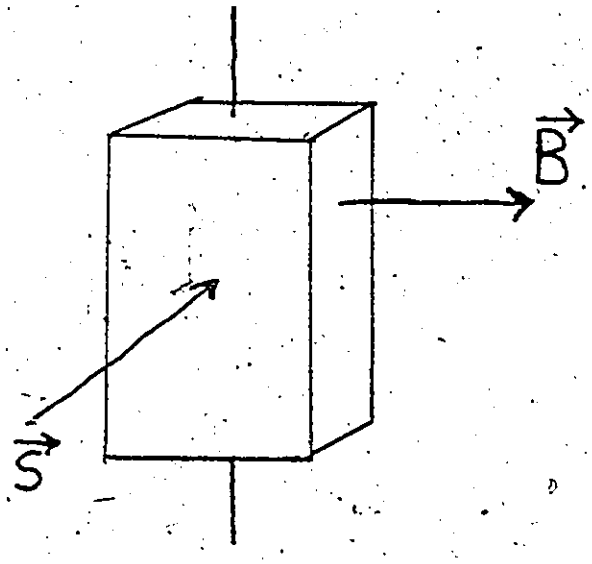

Voigt Configuration

does allow the electric vector $\vec{E}$ to be parallel to the magnetic field $\vec{B}$. This gives rise to a new set of allowed transitions:

$$a^{\pm}(n') \rightarrow b^{c}(n);\ \Delta n = +1$$

$$b^{\pm}(n') \rightarrow a^{c}(n);\ \Delta n = -1 \qquad 3.39$$

where $\Delta M_J = 0$.

Having reviewed the theoretical predictions concerning the energy position of the Landau levels and the allowed transitions between them, the next step is to describe the means by which these transitions reveal themselves physically. One such means is the oscillatory spectral distribution of the absorption coefficient in a magnetic field.

3.2 Absorption Coefficient of a Semiconductor in a Magnetic Field

In a magnetic field the interband transitions between the Landau levels of the valence and conduction band will cause oscillations in the absorption coefficient above the fundamental edge. Again a simple two-band model is used in reviewing this phenomenon. The scattering mechanisms will smooth out the absorption structures and shift the energy position of their maxima towards higher energies. This energy shift is important in our method of investigation and a line shape study of the absorption structures qualitatively relates the maghitude of this shift to the visibility of the structures.

3.2.1 Direct interband magneto-absorption

In the absence of a magnetic field the transition probability and absorption coefficient for direct interband transitions can be calculated from the time dependent perturbation theory, whereby one obtains the "golden rule" given by:

$$\alpha(\omega) = C \int M_{cv}^2 \delta[\varepsilon_c - \varepsilon_v - \hbar\omega] d^3p \qquad 3.40$$

where $\hbar\omega$ is the incident photon energy, M_{cv}, the matrix element between the valence and conduction band, and the coefficient C involves universal constants and the density of states effective mass. The calculation of the absorption coefficient in the simple case of a two-band model has been carried out by a number of workers [3.7] and they find in the absence of a magnetic field:

$$\alpha(\omega) = \frac{A}{\omega} [\hbar\omega - \varepsilon_g]^{\frac{1}{2}} \qquad 3.41$$

where, for allowed direct transitions (in MKS units):

$$A = \kappa e^2 \left[\frac{2m^*}{h}\right]^{3/2} |P_{cv}|^2 / 16\pi c\varepsilon m^2$$

with m^* as the reduced mass, P_{cv} as the momentum matrix, κ as the dielectric constant and ε as the permittivity. The extension of this treatment to include the effect of a magnetic field gives an absorption edge corresponding to each pair of Landau levels. Summing over pairs of initial and final states, the absorption coefficient becomes:

$$\alpha(\omega, H) = \frac{A}{2\omega} s \sum_{n=0}^{\infty} [\hbar\omega - \varepsilon_g - \varepsilon_n]^{-\frac{1}{2}} \qquad 3.42$$

where $\varepsilon_n = (n + \frac{1}{2})s$

and $s = \frac{e\hbar H}{m^*c}$

The dashed curve in Figure 3.4 qualitatively represents the singularities of the absorption coefficient in the presence of a magnetic field. In the absence of scattering the singularities occur when $\hbar\omega = \varepsilon_g + \varepsilon_n$. The solid curve in the same figure is also a qualitative representation of the absorption coefficient in a magnetic field but it includes the broadening of the peaks. The singularities in the absorption do not exist in a real crystal due to the relaxation effects of both the holes and the electrons. Actually, relaxation effects can be introduced quite readily by rewriting the absorption

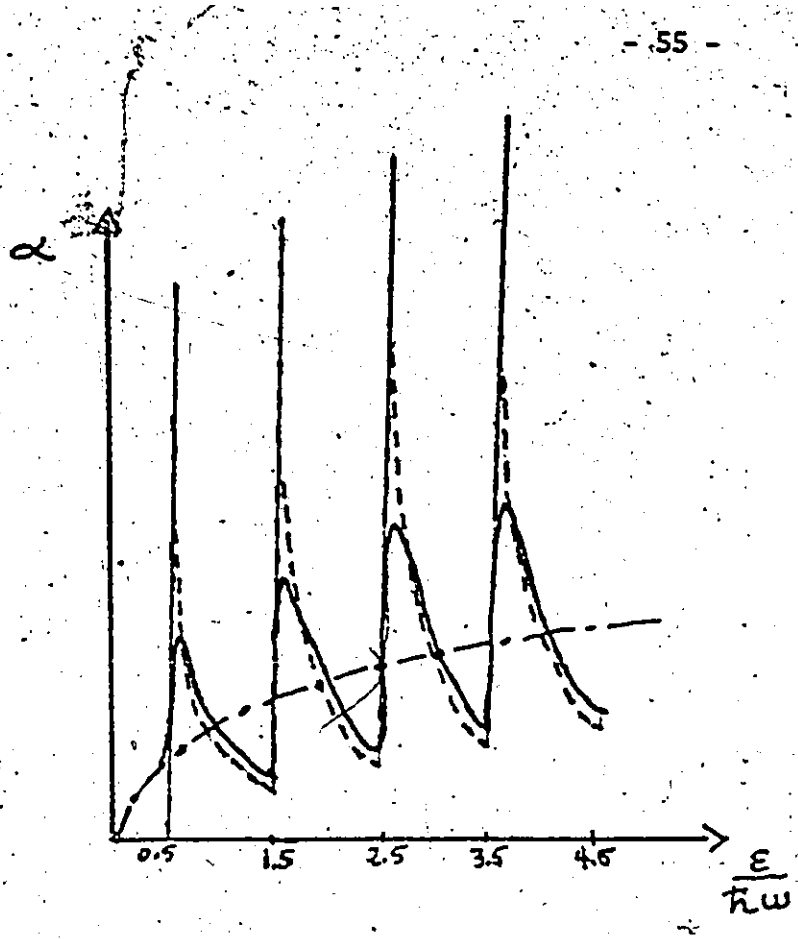

Figure 3.4: The absorption coefficient of a semiconductor as a function of the incident photon energy in the presence of a magnetic field: in the absence of scattering (dashed line), including scattering (solid line). The long dashed line denotes the absorption coefficient in the absence of a magnetic field.

coefficient as:

$$\alpha(\omega, H) = \frac{A'S}{\omega} \sum_{n=0}^{\infty} [\hbar\omega - \varepsilon_g - \varepsilon_n - i/\tau_n]^{-\frac{1}{2}} \qquad 3.43$$

where τ_n denotes the carrier collision time for the n^{th} interband transition. As scattering smooths out the singularities, it also shifts the energy position of the peaks towards higher energy. Unlike modulation techniques, our method of investigation looks at the direct signal and not its derivative. Consequently the importance of the energy shift towards higher energies must be accounted for. Equation (3.43) is difficult to manipulate and in the following sub-section we present a simpler approach to the question of relaxation effects.

3.2.2 A line shape study of the absorption structures

In order to account for the broadening of the absorption structures resulting from the scattering mechanisms, we introduce a broadening parameter Γ_n denoting the uncertainty in the transition energy of the n^{th} oscillation. This parameter Γ_n is related to the carrier collision time τ_n, introduced in equation (3.43), by the Heisenberg uncertainty principle:

$$2\Gamma_n = h/\tau_n \qquad 3.44$$

The relaxation effects can now be introduced by rewriting the absorption coefficient as the convolution of the absorption coefficient function $\alpha(\varepsilon, H)$ with a square distribution function $f(\varepsilon - \varepsilon')$ in the following manner:

$$\alpha(\varepsilon, H) = \int_0^\infty \alpha(\varepsilon)\ f(\varepsilon - \varepsilon')d\varepsilon \qquad 3.45$$

equation 3.45 may be rewritten as:

$$\alpha(\varepsilon, H) = \int_{\varepsilon - \varepsilon'/2}^{\varepsilon + \xi'/2} \alpha(\varepsilon)d\varepsilon \Big/ \varepsilon' \qquad 3.46$$

Putting $\varepsilon'/2 = \Gamma_n$ we obtain for the absorption coefficient:

$$\alpha(\varepsilon, H) = \frac{A'}{2} s \sum_{n=0}^{\infty} \frac{\int_{\varepsilon-\Gamma_n}^{\varepsilon+\Gamma_n} \frac{[\varepsilon - \varepsilon_g - \varepsilon_n]^{-1/2}}{\varepsilon} d\varepsilon}{\Gamma_n} \qquad 3.47$$

where $A' = A\hbar/2$

and $\varepsilon = \hbar\omega$ is the incident photon energy

Integrating the right hand side of equation (3.45) we get.

$$\alpha(\varepsilon, H) = A' \sum_{n=0}^{\infty} \frac{s}{\Gamma_n}[\varepsilon_g - \varepsilon_n]^{-1/2} \left[\tan^{-1} \left[\frac{\hbar\omega + \Gamma_n - [\varepsilon_g + \varepsilon_n]}{[\varepsilon_g + \varepsilon_n]} \right]^{1/2} - \tan^{-1} \left[\frac{\hbar\omega - \Gamma_n - [\varepsilon_g + \varepsilon_n]}{[\varepsilon_g + \varepsilon_n]} \right]^{1/2} \right] \qquad 3.48$$

In the region of interest close to the fundamental edge:

$$\frac{\hbar\omega \pm \Gamma_n - [\varepsilon_g + \varepsilon_n]}{[\varepsilon_g + \varepsilon_n]} \ll 1 \qquad 3.49$$

and the approximation:

$$\tan^{-1} x \simeq x \quad \text{when } x \ll 1 \qquad 3.50$$

is valid in equation (3.46) and it gives:

$$\alpha(\varepsilon, H) = A' \sum_{n=0}^{\infty} \frac{s}{\Gamma_n} [\varepsilon_g + \varepsilon_n]^{-1} \left[(\hbar\omega + \Gamma_n - [\varepsilon_g + \varepsilon_n])^{\frac{1}{2}} - (\hbar\omega - \Gamma_n - [\varepsilon_g + \varepsilon_n])^{\frac{1}{2}} \right] \qquad 3.51$$

According to this last expression the absorption coefficient will exhibit maxima whenever: $\hbar\omega = \varepsilon_g + \varepsilon_n + \Gamma_n$. As indicated in Figure 3.5 the energy shift is expected to be equal to the broadening parameter Γ_n.

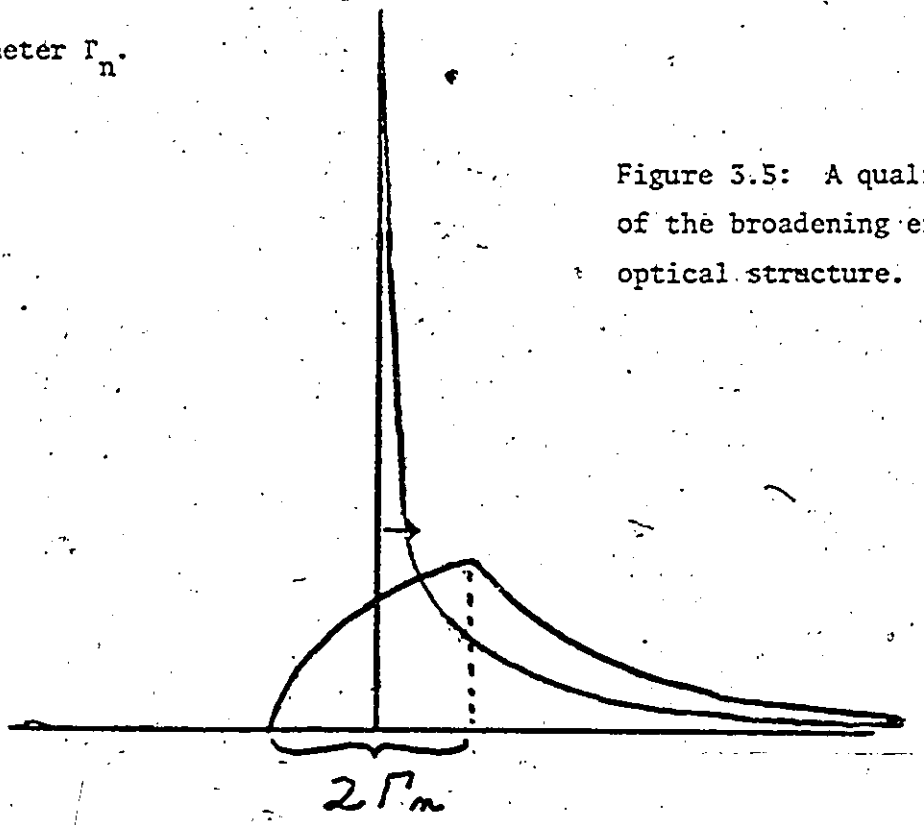

Figure 3.5: A qualitative description of the broadening effects on a magneto-optical structure.

In the limit of low temperatures if one neglects phonon scattering, only impurity scattering remains and the broadening parameter is then proportional to the energy of the carriers to the power -3/2 (3.8). The broadening parameter is thus expected to be maximum at B = 0, where it will smear out the energy position of the convergence of the magneto-optical transition structures, and to diminsh with increasing field strength. The energy shift is therefore expected to decrease with higher magnetic fields, namely the structures become sharper. Nevertheless, if the method of analysis presented in the previous section is to yield the proper band parameter values, the experimental points taken as the energy position of the absorption structure maximum must be corrected for the energy shift, even at higher magnetic fields.

To evaluate this correction we find it useful to introduce the notion of visibility for the absorption structures, in a fashion somewhat analogous to that for the visibility of interference fringes in optics. We define the visibility of the n^{th} oscillation as follows:

$$W(n) = \frac{\alpha_m(n) - \alpha_t(n)}{\alpha_m(n)} \qquad 3.52$$

where $\alpha_m(n)$ is the absorption coefficient for the maximum of the n^{th} oscillation and $\alpha_t(n)$ its minimum where the next structure begins. Figure 3.7 illustrates our definition. Neglecting the contribution of the preceeding oscillations one has for the n^{th} oscillation:

$$\alpha_m(n) = A' \frac{s}{\varepsilon_g + \varepsilon_n} (2/\Gamma_n)^{\frac{1}{2}} \qquad 3.53$$

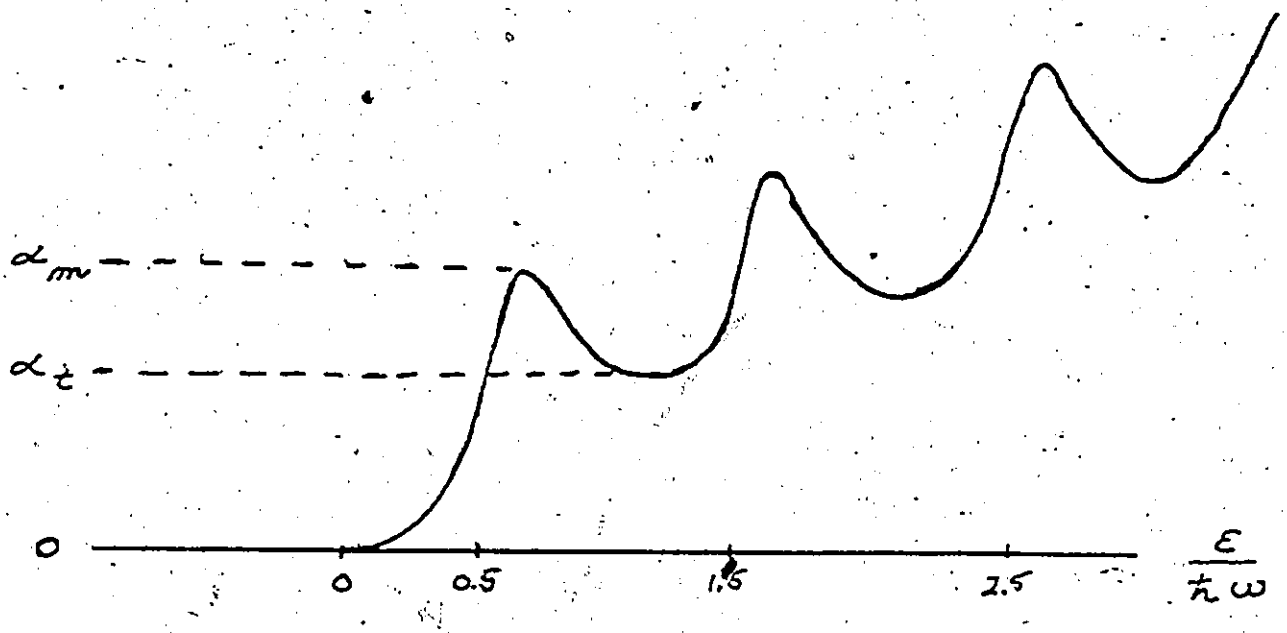

Figure 3.6: An illustration of our definition of visibility for the magneto-optical structures.

and $$\alpha_t(n) = A' \frac{s}{\varepsilon_g + \varepsilon_n + s} \frac{1}{(s)^{\frac{1}{2}}} \qquad 3.54$$

Assuming $\varepsilon_g + \varepsilon_n >> s$, the visibility of the n^{th} structure is:

$$W(n) = 1 - (\Gamma_n/2s)^{\frac{1}{2}} \qquad 3.55$$

A negative value for the visibility has no physical significance and implies that the structure is not visible. The structures are therefore expected to disappear as their broadening parameter tends to twice their separation energy, namely when the uncertainty in the transition energies completely overlap. In a real crystal we also expect the structures to disappear with increasing incident phonon energy because the corresponding increase in the absorption coefficient will tend to redistribute more of the absorbed photo-carriers near the surface where they recombine faster and where the broadening is much larger.

A measure of the visibility of the oscillations should enable us to evaluate τ_n, Γ_n, and the energy shift in the position of the maxima. However, the measured visibility of the structures is reduced by the contributions of the adjacent ones. This is especially true in the case of III-V compounds where the interband transitions possibilities are numerous. Thus our line shape study only informs us that, given the same effective masses, a better visibility of the absorption structures signify a smaller shift in the energy position of their maxima.

The oscillatory spectral distribution of the absorption coefficient for a semiconductor in a magnetic field can be observed in a number of ways. Any physical phenomenon which depends on the absorption coefficient might do. In the next section we discuss the PEM effect in the above context.

4. TRANSPORT PROPERTIES

4.1 The Photoelectromagnetic (PEM) Effect

4.1.1 The classical treatment

4.1.2 The anomalous PEM effect

4.2 Phonon-Electron Interactions in III-V Compounds

4. TRANSPORT PROPERTIES

A study of the transport properties relevant to the PEM effect indicates its dependence on the absorption coefficient above the fundamental edge. Prior to this work the PEM effect had never been used to investigate the changes in the absorption coefficient resulting from magneto-optical interband transitions. Under certain specific conditions we also see how the phonon-electron interactions can profoundly modify the spectral distribution of photo-effects.

4.1 The Photoelectromagnetic (PEM) Effect

When a semiconductor crystal is placed in a magnetic field in the Voigt configuration and light of $h\nu > \varepsilon_g$ is shone on its surface, a photo-voltage will develop at its boundaries. This is the PEM effect. In this section we describe the various transport phenomena involved and indicate the dependence of the effect on the absorption coefficient. When the electron and hole mobilities are different, the difference in diffusion velocity of the carriers gives rise to another photo-effect, the Dember effect. This effect is also seen to depend on the absorption coefficient. Finally, the possibility of an anomalous behaviour is examined.

4.1.1 The classical treament

In this section the PEM effect is described under the following ideal conditions: an homogeneous sample, namely, neglecting surface effects; low intensity illumination ($\Delta n << n$); thick sample, $t >> L_D$ where L_D is the

injected carriers diffusion length. Based on the most complete classical treatment of the PEM effect, that of W. van Roosbroeck (4.1), the PEM effect can be described as a Hall effect associated with the diffusion of optically injected carriers. The excess concentration of carriers at the illuminated surface diffuse inwards in a random walk fashion. The diffusion current density of the carriers is given as:

$$J_x(x) = e\ D\ \nabla_x n(x) \qquad 4.1$$

where $$D = \mu \frac{kT}{e}$$

n(x) being the carrier concentration at a depth x away from the illuminated surface and μ the Hall mobility of the carrier. The simplest case occurs when the mobility* of both carriers, the electron and the hole, is equal and there is no trapping. As shown in Figure 4.1 the diffusing carriers will be deflected in the presence of a magnetic field by the Hall angle θ where:

$$\tan\theta = \mu B \qquad 4.3$$

For low magnetic fields where tan θ < 1 the current density along the y-axis will be:

$$J_y(x) = 2J_x(x) \tan\theta \qquad 4.4$$

---

* Unless otherwise specified, mobility is to be taken as meaning Hall mobility.

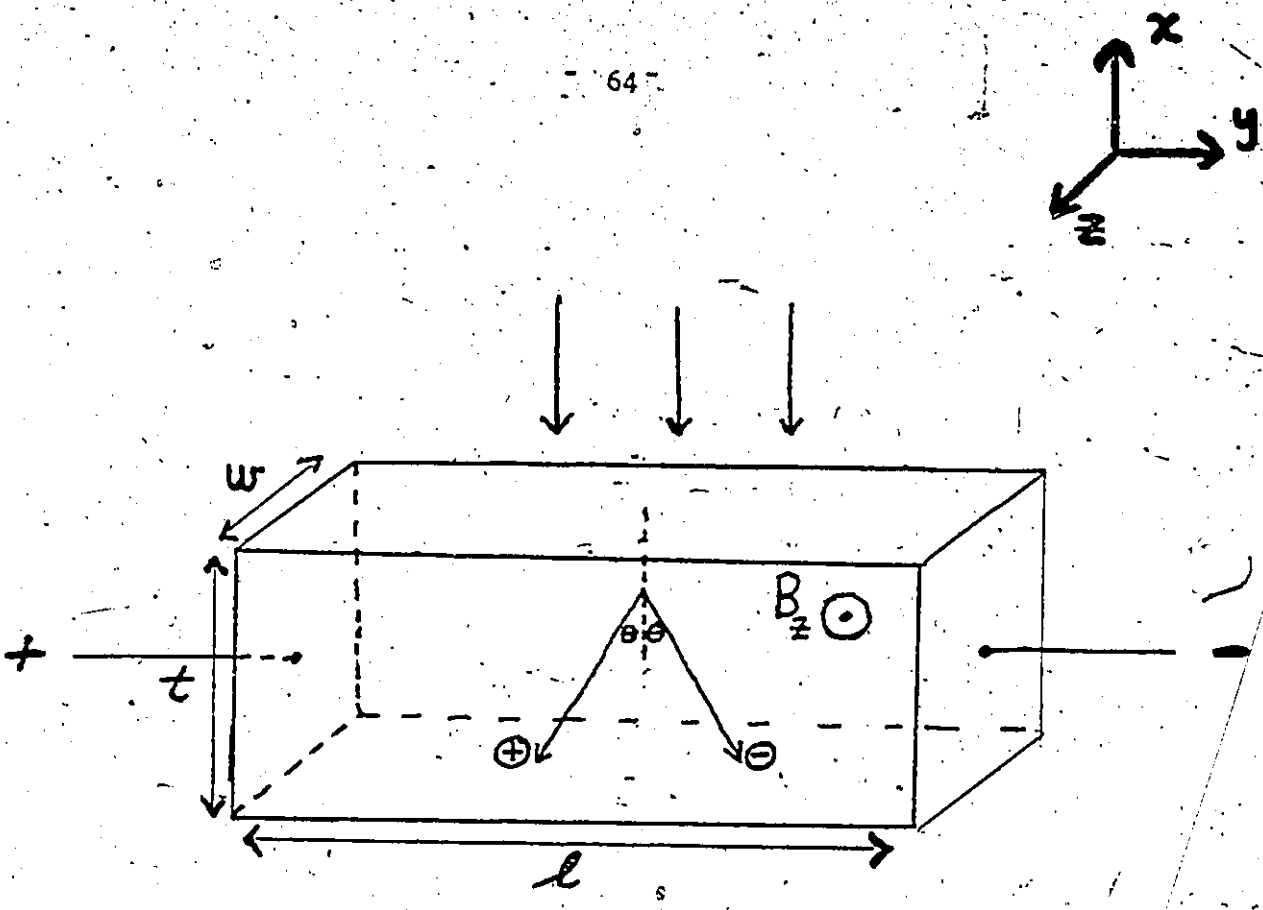

Figure 4.1: A description of the PEM effect.

Substituting equations (4.1) and (4.2) into equation (4.4) one gets:

$$J_y(x) = 2\mu^2 \, B \, kT \, \nabla_x n(x) \qquad 4.5$$

Averaging the current density $J_y(x)$ over the thickness and multiplying by the cross-section of the sample gives the PEM effect short-circuit current:

$$i_{PEM} = 2w\mu^2 \, B \, kT \, [n(t) - n(0)] \qquad 4.6$$

where w is the width of the sample and t its thickness.

The number of photons absorbed per increment dx is given by:

$$-\frac{dN}{dx} = N_0 \alpha e^{-\alpha x} \qquad 4.7$$

where $$N = N_0 e^{-\alpha x} \qquad 4.8$$

and N_0 being the incident number of photons per unit area per unit time. Assuming a quantum efficiency of one the carrier generation rate G(x) will then be:

$$G(x) = N_0 \alpha e^{-\alpha x} \qquad 4.9$$

The recombination rate R(x) will be:

$$R(x) = r [n(x)]^2 \qquad 4.10$$

since both carriers have an equal concentration distribution; r is a constant depending on the recombination rate of the carriers. Equating the generation and recombination rate, we get for the carrier concentration at equilibrium:

$$n(x) = \left[\frac{N_0 \alpha}{r}\right]^{\frac{1}{2}} e^{-\alpha x/2} \qquad 4.11$$

By substituting the above carrier concentration expression in the short-circuit current expression, equation (4.6) and assuming $t >> \alpha^{-1}$ above the fundamental edge, we get:

$$i_{PEM} = 2w\mu^2 B kT \left[\frac{N_0 \alpha}{r}\right]^{\frac{1}{2}} \qquad 4.12$$

Therefore under ideal conditions the PEM short-circuit current can be expected to vary as the square root of the absorption coefficient.

A more realistic case would have a different Hall mobility for each type of carrier. In the absence of trapping, for an n-type semiconductor, the situation can be mathematically described as follows:

$$J_x(x)/e = -Dpx \frac{dp(x)}{dx} + \mu_p\, p(x)E_x(x) \qquad 4.13$$

$$J_x(x)/e = bDpx \frac{dn(x)}{dx} + b\mu_p[n_0 + n(x)]E_x(x) \qquad 4.14$$

where $$J_x(x) = J_{px}(x) = -J_{nx}(x) \qquad 4.15$$

μ_p is the hole mobility, μ_n is the electron mobility and $b = \mu_n/\mu_p$, n_0 is the electron density in the dark, $n(x)$ and $p(x)$ are the density of excess photo-excited electrons and holes respectively, and $E_x(x)$ is an electric field that builds up across the thickness of the sample as a result of the Dember effect. The Dember effect arises as a result of the greater mobility of one carrier. These carriers diffuse faster, setting up at equilibrium an electric field $E(x)$ which assists the transport of the minority carrier and retards that of the majority carrier. Under such conditions the PEM effect becomes a minority carrier effect, because for every minority carrier that diffuses and recombines a majority carrier must tag along to maintain equilibrium. The situation is essentially the same as in the previous case and equation (4.12) is still valid provided the proper corrections are made to the parameters μ and r. The Dember short-circuit current can be obtained by averaging the majority carrier diffusion current density over the thickness of the sample and multiplying by the area

of the illuminated surface. We then get for the Dember short-circuit current:

$$i_D = \frac{w\ell}{t} \mu kT \left[\frac{N_0 \alpha}{r}\right]^{\frac{1}{2}} \qquad 4.16$$

Equations (4.12) and (4.16) indicate the dependence of both the PEM and Dember effect on the absorption coefficient. These effects are thus expected to reflect the spectral distribution of the absorption coefficient. The next step is to verify that equations (4.12) and (4.16) are also valid in the limit of intense magnetic fields.

4.1.2 The anomalous PEM effect

In the case of a very high surface recombination velocity resulting from surface defects or surface oxidation, the carrier concentration at the illuminated surface could decrease sufficiently to cause a sign reversal of the diffusion current. The situation is illustrated in Figure 4.2. The fast recombination of the carriers

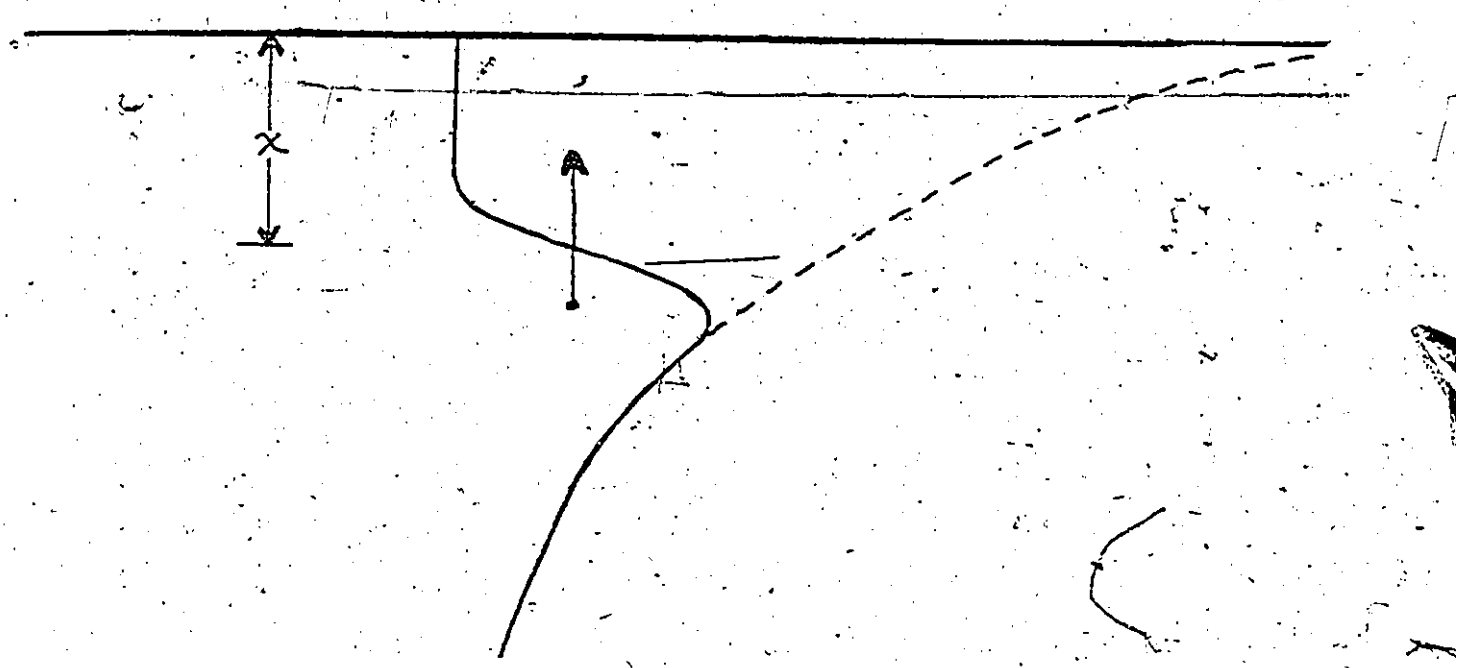

Figure 4.2: The qualitative demonstration of a sign reversal for the diffusion of optically injected carriers due to the high surface recombination velocity in a surface layer of thickness x.

near the surface causes the concentration gradient to be steeper towards the illuminated surface reversing the normal diffusion direction of the optically injected carriers. Both the PEM and Dember would then also reverse. Such anomalous behavior has been observed for the above effects [4.2]. Under the above condition an increase in the absorption

coefficient would redistribute more of the injected carriers into the high recombination region at the surface, reducing both the net number of carriers and their concentration gradient towards the illuminated surface. The minima rather than the maxima are then expected to reflect the magneto-optical interband transitions in the case of an anomalous PEM or Dember effect. As will be seen in section 5.3.1, InP is believed to exhibit the above anomalous condition.

We have now seen that both the normal and anomalous behaviors of the PEM and Dember effects can reflect the oscillatory spectral distribution of the absorption coefficient for a semiconductor in a magnetic field. Given certain specific conditions the PEM effect can also reflect the phonon-electron interactions present in III-V compounds. In the next section we will review the mechanisms whereby the phonon-electron interactions give rise to broader oscillations in the spectral distribution of photo-effects.

4.2 Phonon-Electron Interactions

Under certain specific condition, spectral oscillations may appear in photo-effects as a result of phonon-electron interactions. According to Habegger and Fan [4.3] the broad oscillations associated with longitudinal optical (LO) phonons and usually observed in photo-conductivity would arise from the carriers being photo-injected with a definite energy and then losing this energy by the emission of an

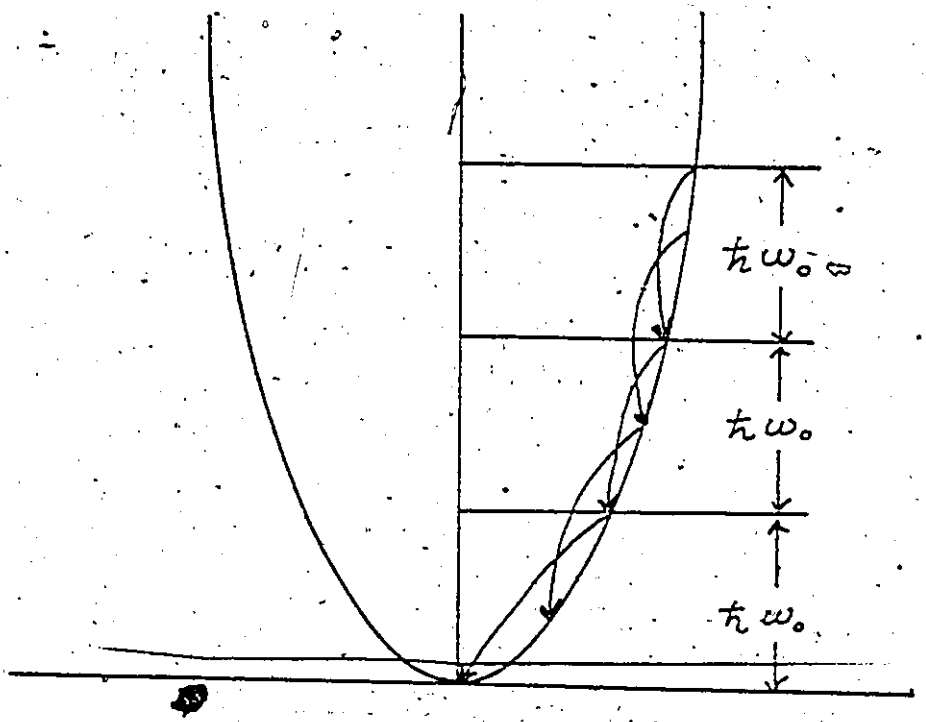

Figure 4.3: The LO phonon transition cascading process in the absence of a magnetic field.

integral number of LO phonons. This cascading process is shown in Figure 4.3. Provided the carriers are not allowed to be thermalized by acoustical phonons, their energy will then oscillate between zero and the LO phonon energy. Variations of the mobility or carrier lifetime as a function of energy in the prescribed interval will then cause oscillations in the photo-current. This model requires the following conditions for the observation of the broad oscillations associated with LO phonons:

$$\tau_{op} < \tau_l < \tau_{ac} \qquad 4.17$$

where τ_{op} is the optical phonon-electron relaxation time, τ_{ac} is the acoustical phonon-electron relaxation time, and τ_1 is the free carrier lifetime. For an intrinsic semiconductor the energy position of the photo-current minima will be given by:

$$\varepsilon_\ell = \varepsilon_g + \ell\hbar\omega_0[1 + m_c/m_{hh}] \qquad 4.18$$

where $\ell = 0, 1, 2 \ldots$ is the number of phonon emission, $\hbar\omega_0$ is the phonon energy and the term $[1 + m_c/m_{hh}]$ takes into account the valence and conduction band curvature.

Uchinokura and Fan [4.4] also explain the appearance of additional fine structures in the presence of a magnetic field by supposing that the Landau sub-bands have lower mobilities causing small dips in the photo-current. The cascading phonon emission process in the presence of a magnetic field is illustrated in Figure 4.4.

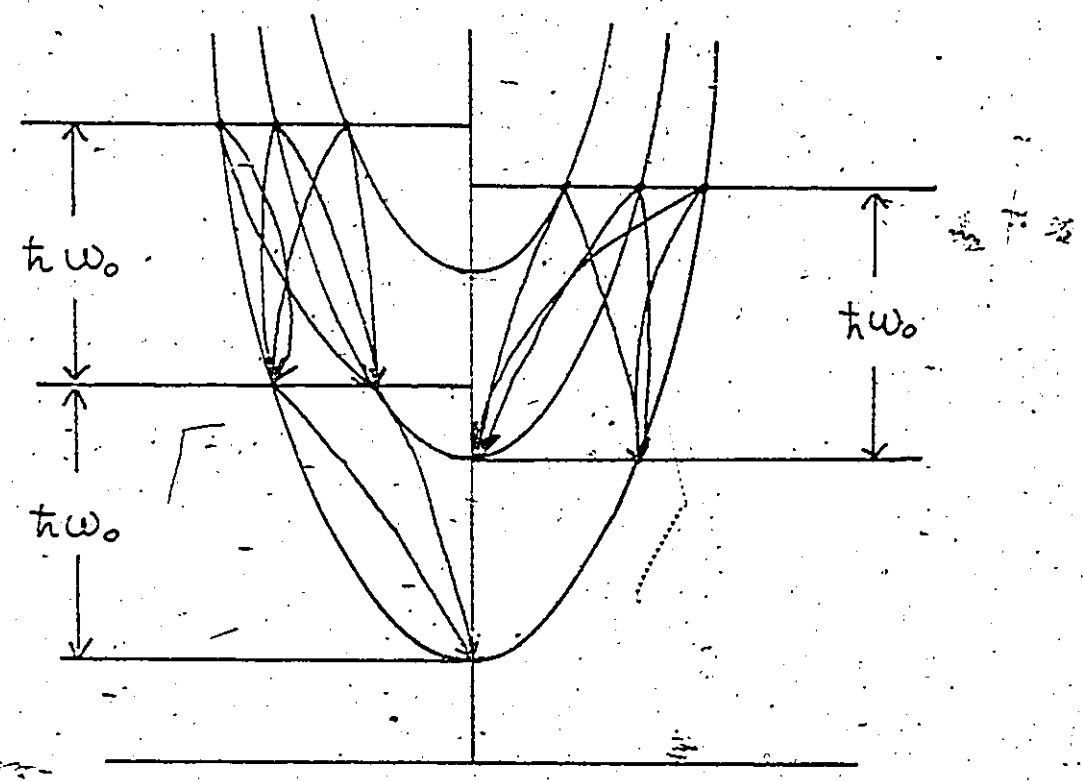

Figure 4.4: The LO phonon transition cascading process in the presence of a magnetic field.

As can be seen from the figure, there now exist a number of phonon transition possibilities in the presence of a magnetic field and the transitions to the higher energy Landau levels are responsible for the reduction in mobility of the conduction band transport electrons.

The broad oscillations associated with LO phonons have been observed in the hetero-polar materials such as GaSb, section 5.2.2., InP, section 5.3.2, and GaAs, section 5.4.3.

5. EXPERIMENTAL RESULTS AND DISCUSSION

5.1 Germanium

5.1.1 The PEM effect

5.1.2 The Dember effect

5.1.3 The irradiated and pyrolytically coated samples

5.2 Gallium Antimonide

5.2.1 The interband transitions between the Landau levels

5.2.2 The phonon-electron interactions

5.3 Indium phosphide

5.3.1 The interband transitions between the Landau levels

5.3.2 The phonon-electron interactions

5.4 Gallium Arsenide

5.4.1 The photoconductivity spectra

5.4.2 The epitaxial GaAs

5.4.3 The high resistivity GaAs

5. EXPERIMENTAL RESULTS AND DISCUSSION

The aim of this research project was to establish the PEM effect as an accurate and reliable method of investigating magneto-optical interband transitions in a semiconductor. The method could then be used to determine the band parameter values of various materials. An extensive study on two germanium crystals verifies the theoretical predictions concerning both the PEM and Dember effect and establishes the PEM effect as a powerful but simple method of magneto-optical investigation. The oscillatory spectral distribution of the PEM effect in gallium antimonide and indium phosphide then allowed us to evaluate the band parameter values for these semiconductors. Given certain specific surface conditions, broader spectral oscillations are also observed in these two materials. The broader structures were associated with phonon-electron interactions and the longitudinal (LO) phonon energy was then calculated. In gallium arsenide, photoconductivity is more sensitive to changes in absorption resulting from magneto-optical transitions. The oscillatory spectral distribution of photoconductivity in a magnetic field was therefore studied for an epitaxial gallium arsenide sample. The broader structures associated with phonon-electron interactions were also observed for gallium arsenide, this time in a high resistivity material and the LO phonon energy could also be calculated for this material. Finally we discuss the possible mechanisms responsible for the appearance of the broader phonon structures after the surface oxidation of the samples.

5.1 Germanium

In magneto-optics germanium is a very well documented semiconductor which can be obtained in a very pure form. It was the ideal material to verify the theoretical predictions concerning the PEM effect. In order for the intrinsic properties of germanium to be identified, two crystals were studied and compared. The energy position of the maxima in the spectral distribution of the PEM effect were corrected for their energy shift and analysed using the Pidgeon and Brown scheme. The excellent agreement between the band parameter values obtained and those previously reported by other workers establishes the PEM technique as an accurate method of investigating magneto-optical phenomena.

The theoretical developments concerning the PEM effect also indicated that the Dember effect should reflect the oscillatory spectral distribution of the absorption coefficient. This prediction is verified in germanium. The Dember effect also diminishes with the magnetic field; this finding supports our previous ideas concerning the mobility of diffusing carriers in a magnetic field. We conclude this section by reporting some results dealing with the surface and bulk treatment of the germanium crystals.

5.1.1 The PEM effect

A series of PEM short-circuit current spectra were obtained from two germanium samples, labelled Ge (M) and Ge (N), for both linear

polarizations, E // B and E ⊥ B, in magnetic fields up to 70 kG at 4.2K. Figure 5.1 shows the PEM spectra of both samples at 20 kG for the E // B polarization. Even at this relatively low magnetic field some fifteen well resolved structures are observed. Remembering that the PEM technique, like magneto-absorption, is a direct method this first result immediately indicates the sensitivity of the technique to changes in absorption resulting from interband magneto-optical transitions. The next figure, Figure 5.2, shows the PEM spectra of both samples at 50 kG for the E ⊥ B polarization. According to the visibility expression derived in Chapter 3.2.2, equation (3.55), one would expect the resolution of the structures to increase monotonically with the field. As can be seen in Figures 5.1 and 5.2 this is not the case for germanium. Figure 5.3 gives the visibility of the magneto-optical structures as a function of the magnetic field. The sharp decrease in the visibility of the structures above 25 kG could possibly be related to a sharp increase in the efficiency of the scattering mechanism. However, no satisfactory explanation has been found to account for such a phenomenon.

The most important feature of these figures is the correspondence between the energy position of the structures of both samples. This correspondence indicates that the energy position of the structures depends on the intrinsic properties of the material. On the other hand, the difference in amplitude and shape between the structures of both samples suggests that these characteristics depend

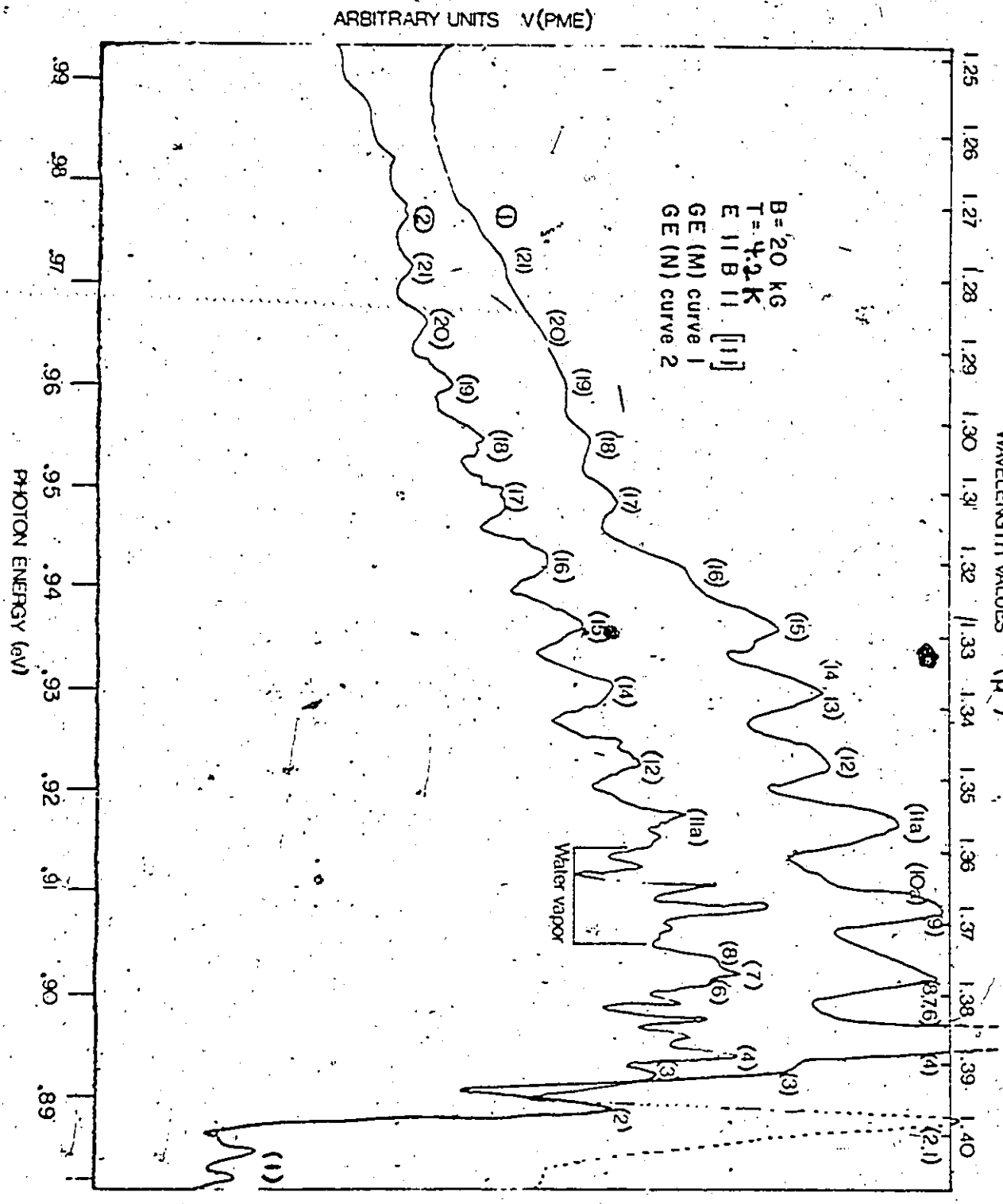

Figure 5.1: PEM spectra for the E // B polarization of both Ge (M) and Ge (N) at 20 kG. The dashed line indicates a peak scaled down by a factor of -3.

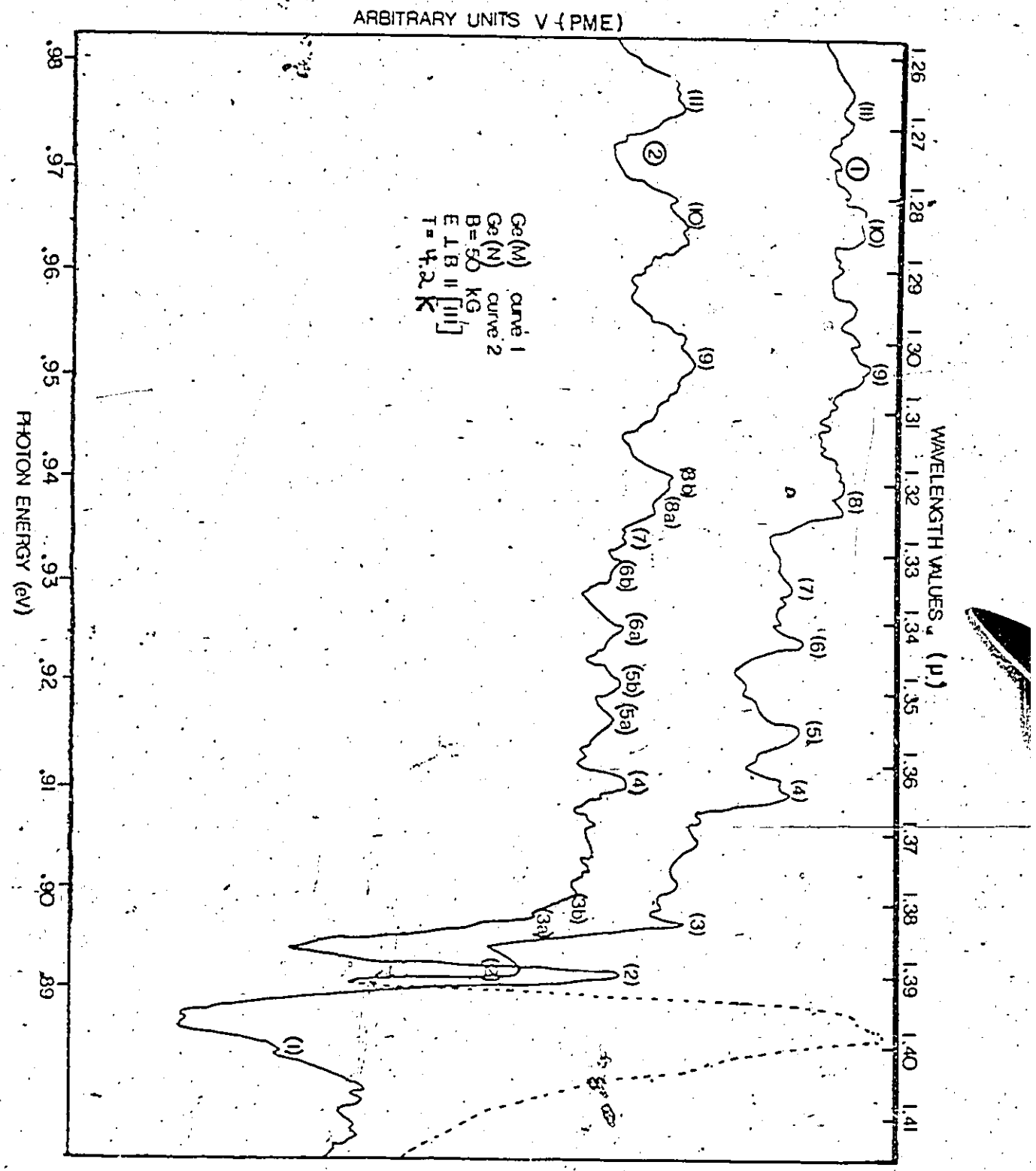

Figure 5.2: PEM spectra for the E ⊥ B polarization of both Ge (M) and Ge (N) at 50 kG. The dashed line indicates a peak scaled down by a factor of -3.

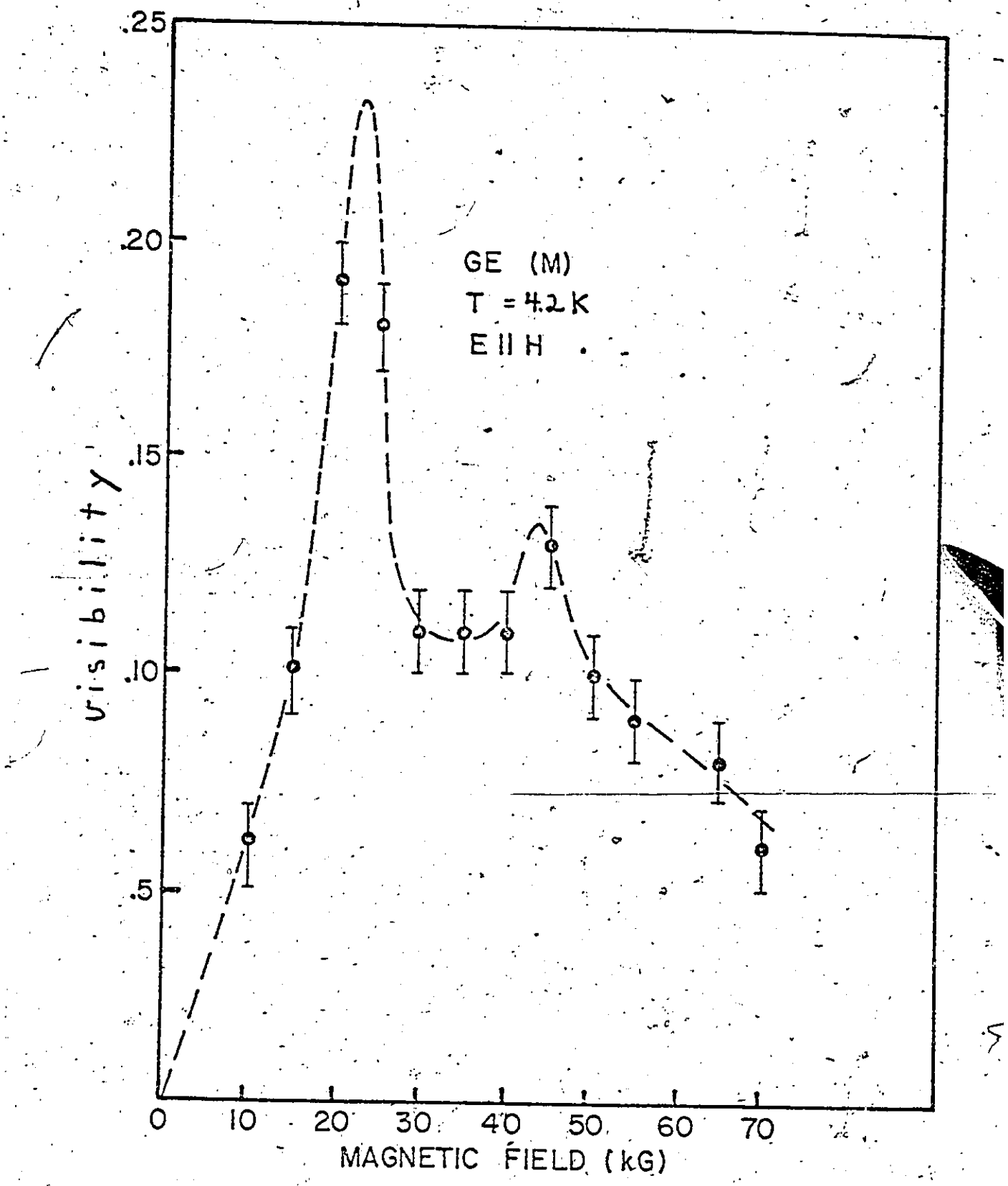

Figure 5.3: Visibility of the magneto-optical structures in the PEM spectra of germanium versus the magnetic field strength.

on externalities such as the surface treatment or the impurity concentration. In the last sub-section dealing with germanium we report an experiment which demonstrates the influence of impurity concentration on the amplitude of the structures. Below the fundamental edge the two samples differ considerably. The peak labelled 2 is believed to be associated with an excitonic level below the conduction band. The position of the other peak (≈ 5 meV below the fundamental edge) precludes its assignment to an excitonic level and suggests the presence of a deep donor impurity level.

In magneto-optics one makes use of the so-called "fan diagrams". They are graphs plotting the energy position of the maxima in the oscillatory spectral distribution of the signal versus the magnetic field strength. Figures 5.4 to 5.7 present the fan diagrams for the PEM effect in germanium for both samples and both polarizations. The dashed lines represent the experimental curves for the energy positions of the maxima versus the magnetic field. Note how the higher energy curves become equally spaced as predicted by the linear theory of Luttinger and Kohn. Their convergence energy at zero field gives, for the direct bandgap energy of germanium, a value of 0.888 ± 0.001 eV, which is in agreement with the normally quoted values of 0.888 ± 0.0005 eV (5.1). The peak labelled 2 extrapolates at zero field to a value of ∿ 1.5 meV below the above convergence energy. This confirms its assignment to an excitonic level below the conduction band. The binding energy of the exciton in germanium being usually given as

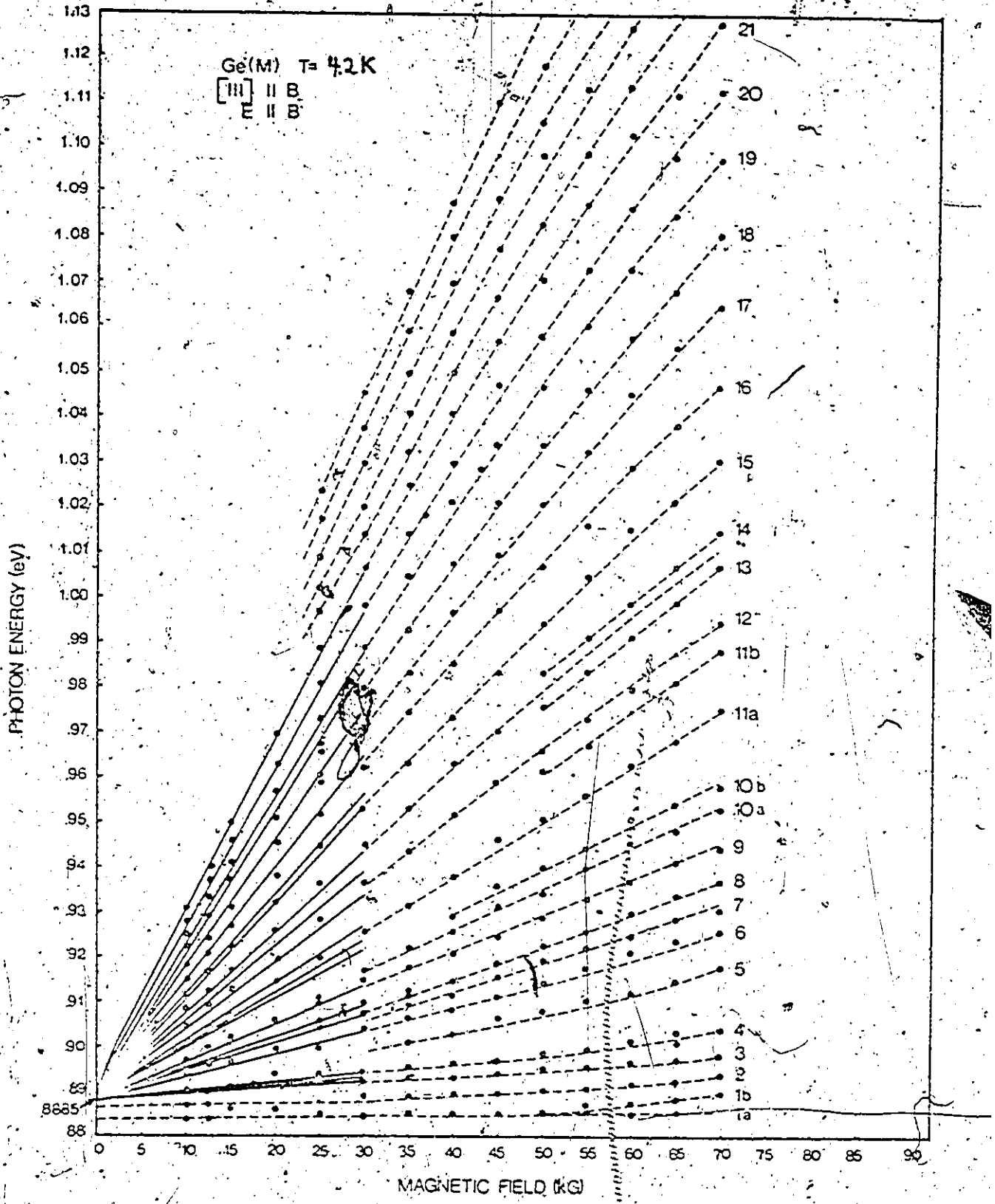

Figure 5.4: Photon energy values at the maxima versus the magnetic field strength for the E // B polarization PEM spectra of Ge (M). The dashed lines represent the experimental curves, the solid lines the theoretical curves.

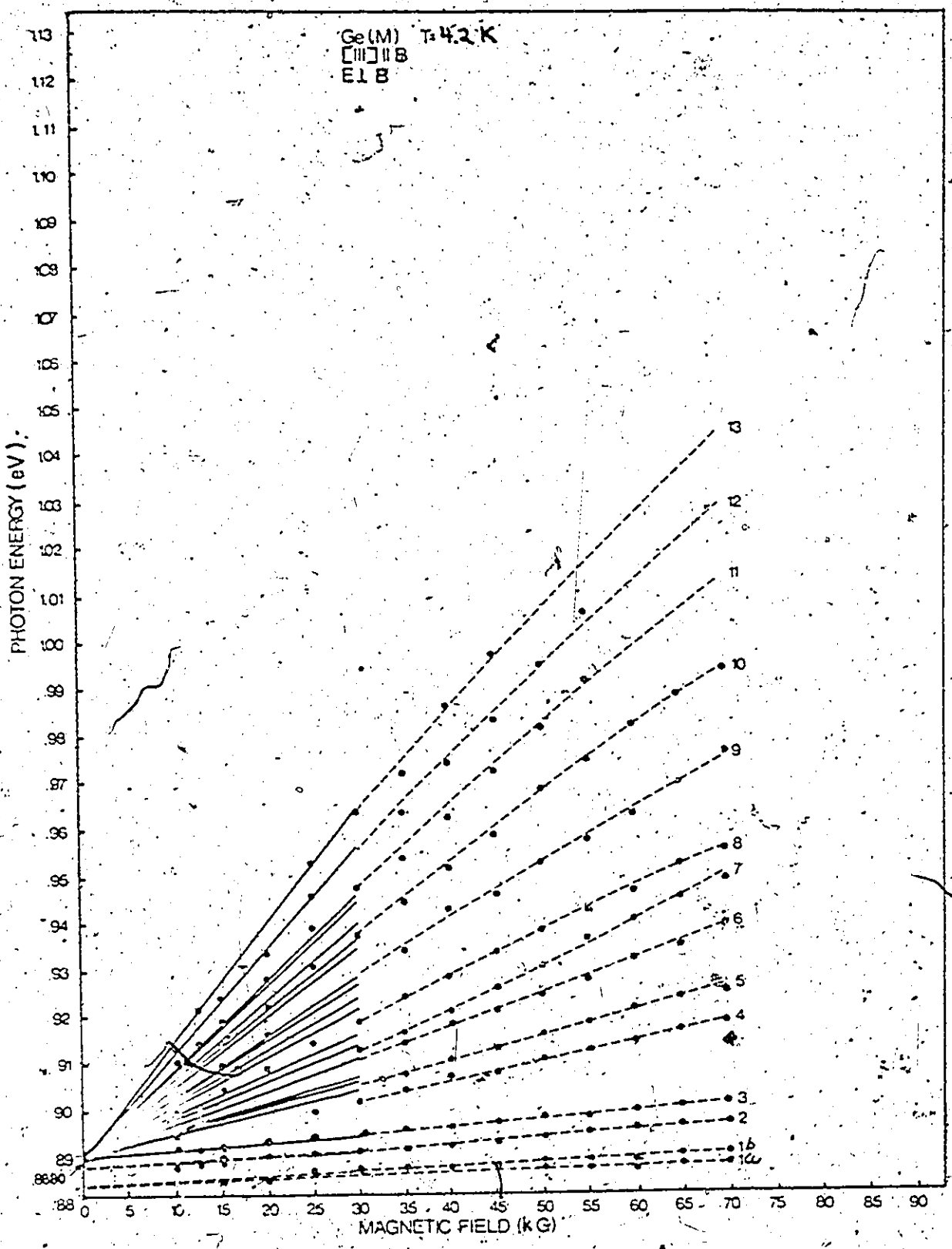

Figure 5.5: Photon energy values at the maxima versus the magnetic field strength for the E ⊥ B polarization PEM spectra of Ge (M). The dashed lines represent the experimental curves, the solid lines the theoretical curves.

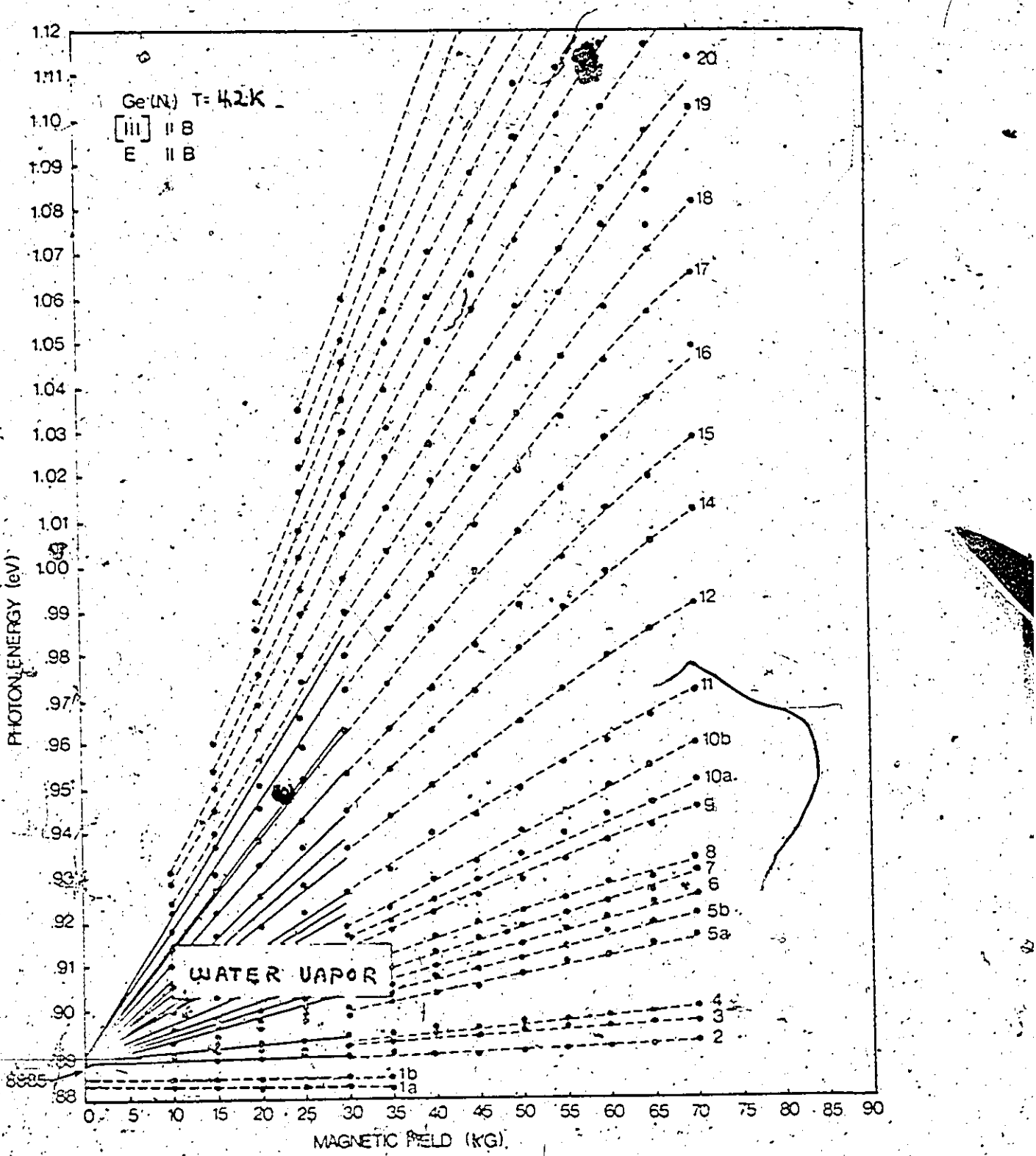

Figure 5.6: Photon energy values at the maxima versus the magnetic field strength for the E // B polarization PEM spectra of Ge (N). The dashed lines represent the experimental curves, the solid lines the theoretical curves.

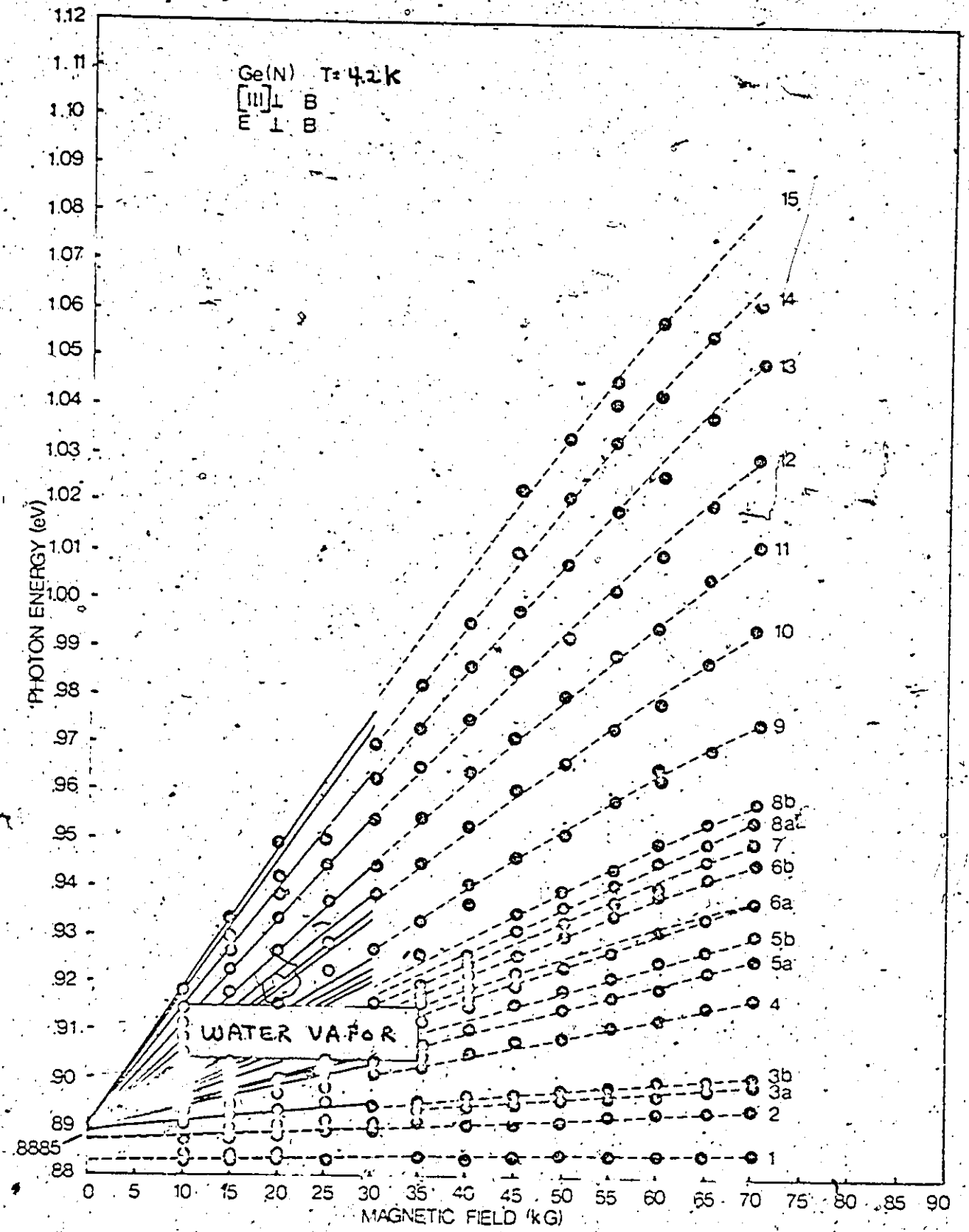

Figure 5.7: Photon energy values at the maxima versus the magnetic field strength for the E ⊥ B polarization PEM spectra of Ge (N). The dashed lines represent the experimental curves, the solid lines the theoretical curves.

1.4 - 2.2 meV (5.2).

The solid lines represent theoretical predictions of Luttinger and Kohn for the energy position of the maxima using the following parameters:

γ_1 = 13.58
γ_2 = 4.3
γ_3 = 5.68
k = 3.41

Hensel (1968) and Hensel and Suzuki (1969) (5.3)

m_c/m = 0.038
g_c = -3.0

Aggarwal (1970) (5.1)

A first comparison of the experimental curves with the linear predictions allows their identification. Using the coding system given in Table 5.1, the fan diagram of Ge (M) for the E // B polarization is identified in Table 5.2.

Table 5.1

Allowed Direct Interband Transitions Code

For E // B

$a^+(n) \rightarrow b^c(n+1)$	$A^+(n)$
$b^+(n) \rightarrow a^c(n-1)$	$B^+(n)$
$a^-(n) \rightarrow b^c(n+1)$	$A^-(n)$
$b^-(n) \rightarrow a^c(n-1)$	$B^-(n)$

For E $\perp$ B (strong)

$a^+(n) \rightarrow a^c(n-1)$	$AS^+(n)$
$b^+(n) \rightarrow b^c(n+1)$	$BS^+(n)$
$a^-(n) \rightarrow a^c(n-1)$	$AS^-(n)$
$b^-(n) \rightarrow b^c(n+1)$	$BS^-(n)$

For E $\perp$ B (weak)

$a^+(n) \rightarrow a^c(n+1)$	$AW^+(n)$
$b^+(n) \rightarrow b^c(n-1)$	$BW^+(n)$
$a^-(n) \rightarrow a^c(n+1)$	$AW^-(n)$
$b^-(n) \rightarrow b^c(n-1)$	$BW^-(n)$

Table 5.2

[3] $B^-(1)$, m = 0.83

[4] $A^+(-1)$, m = 1.1

[5] , m = 1.3

[6] $B^-(2)$, m = 1.0

[7] $A^+(0)$, m = 1.1

[8] $B^+(1)$, m = 1.1

[9] $A^-(1)$, $B^-(3)$, m = 0.94

[10a] , m = 1.0

[10b] , m = 0.97

[11a] $A^+(1)$, $A^-(2)$, $B^+(2)$, $B^-(4)$, m = 1.0

[11b] , m = 0.93

[12] $A^-(3)$, $B^-(5)$, m = 0.98

[14] $A^+(2)$, $A^-(4)$, $B^+(5)$, $B^-(6)$, m = 0.95

[15] $A^+(3)$, $A^-(5)$, $B^-(7)$, m = 0.95

[16] $A^-(6)$, $B^-(8)$, m = 0.93

[17] $A^+(4)$, $A^-(7)$, $B^-(9)$, m = 0.93

[18] $A^-(8)$, $B^-(10)$, m = 0.90

[19] $A^-(9)$, $B^-(11)$, m = 0.91

[20] $A^-(10)$, $B^-(12)$, m = 0.89

[21] $A^-(11)$, $B^-(13)$, m = 0.89

The parameter "m" associated with each experimental curve is given by:

$$\varepsilon = \varepsilon_g + aB^m \qquad 5.1$$

where "a" is a constant. For lower energy transitions, $m > 1$, a result consistent with the theory of excitonic effects in high magnetic fields (5.4). For higher energy transitions, $m < 1$, a behaviour attributable to the non-parabolicity effects.

In the Pidgeon and Brown analysis which follows, only the higher energy transitions were included in the calculations since the analysis does not take into account the excitonic effects. Furthermore, the computer program (see appendix) only fits the heavy-hole transitions. The Pidgeon and Brown analysis was therefore limited to the $B^-(7)$ to $B^-(15)$ transitions, see curve 15 to 21 for the E // B polarization spectra of Ge (M). The fixed parameters used in the analysis were:

$$\gamma_3^L - \gamma_2^L = 1.38$$

$$\varepsilon_g = 0.888 \text{ eV}$$

$$A = 0.294 \text{ eV}$$

$$F = -1.1 \ (\hbar^2/m)$$

The resulting set of fitted band parameter values for germanium is given in Table 5.3 where it is compared to other experimental and

Table 5.3

Comparison of the band parameter values for Ge determined in the present experiment with previously published values.

Parameter	Present Experiment	Aggarwal (5.1)	Lawaetz (5.5)
m_c/m	0.0385 ± 0.005	0.0380 ± 0.0005	0.038
γ_1^L	13.31 ± 0.6	13.38* ± 0.02	13.35
γ_3^L	5.6 ± 1.4	5.68* ± 0.02	5.69
k^L	3.2 ± 2.5	3.41* ± 0.03	3.41
g_c	-3.0 ± 1.5	-3.0 ± 0.2	-2.86
m_{eh}/m	0.042	0.042	0.043
m_{hh}/m	0.35	0.34	0.35
E_p	26 eV ± 3eV	26.8 eV ± 0.4eV	26.3 eV

* Taken from reference 5.3

theoretical sets of values. The root mean square deviation for the set of values obtained was only 1.35 meV. That and the excellent agreement of our results with those of Lawaetz (5.5) establish the PEM technique as an accurate and reliable method of investigating magneto-optical interband transitions.

Because of the relatively poor visibility ($\sim$ 0.15) of the structures at higher fields, a large energy shift Γ_n was expected in the position of the maxima. We refer the reader to chapter 3 equation (3.53):

$$W(n) = 1 - (\Gamma_n/2s)^{\frac{1}{2}} \qquad (5.2)$$

For a poor visibility W(n) one would expect a large energy shift, Γ_n. Actually, the fit required that an average of 5.5 meV be substracted from the experimental data. When compared to the root mean square deviation for the set of band parameter values obtained this correction is quite large. Some experimental measurements (5.19) of the carrier collision time in ultra-pure germanium at 4.2 K report values of the order of 10^{-10} to 10^{-9} seconds. For such values Γ_n equals 10^{-2} meV. This is a lower limit, the samples studied had a much larger impurity concentration at their surface (due to surface deterioration) and it is not unrealistic to expect broadening parameters of the order of a few meV. We must therefore conclude that the scattering mechanisms, probably impurity scattering, plays an important role in the spectral distribution of the PEM effect. This is also true for modulated magneto-optical experiments, since the scattering mechanisms will also shift the energy position of a differentiated structure.

5.1.2 The Dember effect.

The previous theoretical developments concerning the PEM effect indicated that the Dember effect should also reflect the oscillatory spectral distribution of the absorption coefficient for a semiconductor in a magnetic field. A series of Dember short-circuit current spectra were obtained for Ge (M) for both linear polarizations in magnetic fields up to 70 kG at 4.2 K. Figure 5.8 shows the spectra of both polarizations at 45 kG. The energy positions of the maxima correspond to those obtained for the PEM effect. This can perhaps be best illustrated by comparing the PEM effect fan diagrams for Ge (M) (Figures 5.4 and 5.5) to those obtained for the Dember effect (Figures 5.9 and 5.10). The average convergence energy of the experimental curves above the fundamental edge is 0.888 ± 0.001 eV, giving us the same bandgap energy for germanium as that obtained from the PEM spectra. The peak labelled 2, previously associated to an excitonic level below the conduction band, is more prominent in the Dember effect. In the E // B polarization spectra, Figure 5.9, a splitting of the peak at higher magnetic field, probably the Zeeman splitting, can even be observed. The extrapolated energy at zero field for this structure is approximately 1 meV below the convergence energy of the experimental curves. This energy separation is consistent with the exciton binding energy value of 1.4 - 2.2 meV for germanium (5.2).

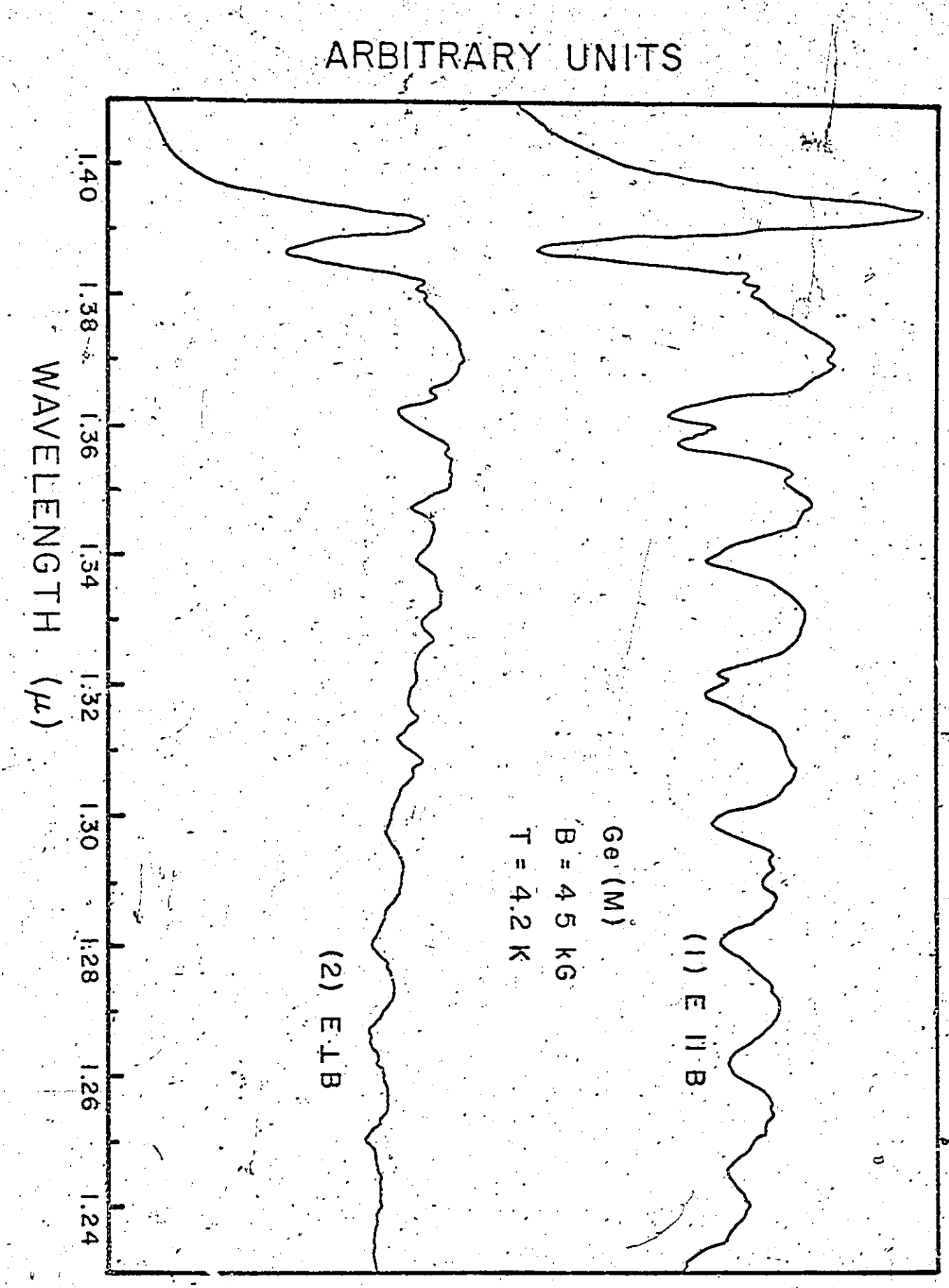

Figure 5.8: Dember spectra for the E // B and E ⊥ B polarization of Ge (M) at 45kG.

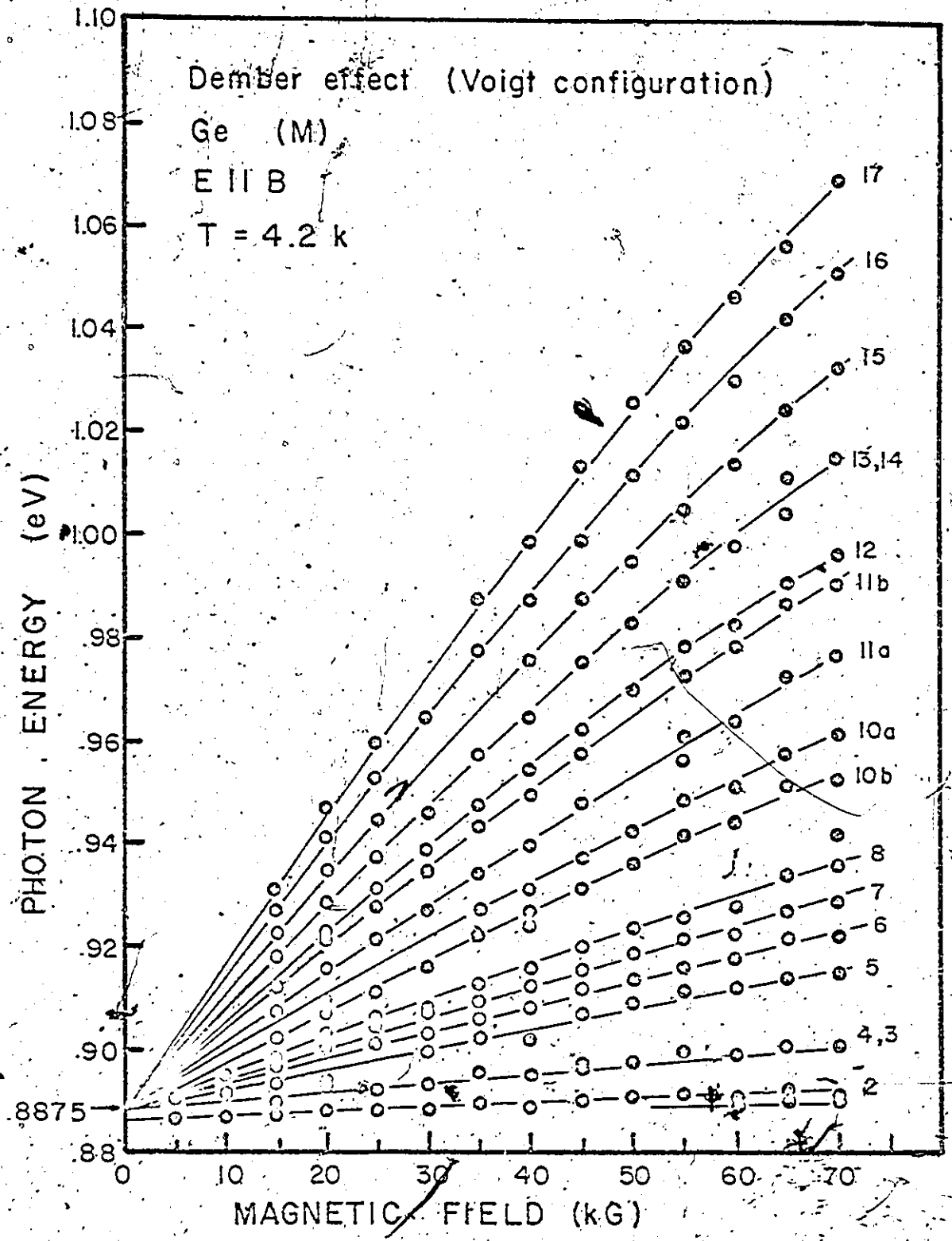

Figure 5.9: Photon energy values at the maxima versus the magnetic field strength for the E // B[0] polarization Dember spectra of Ge (M).

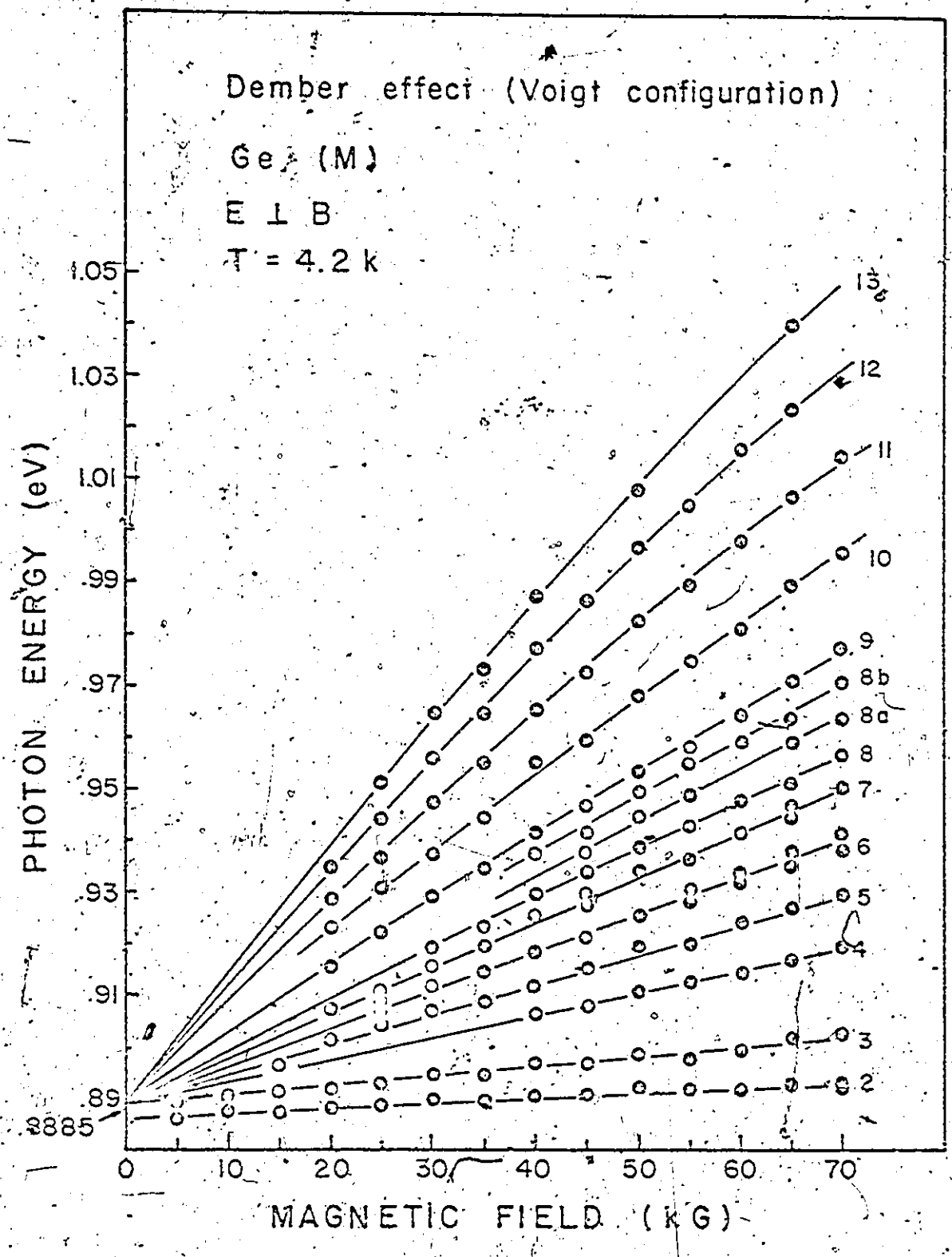

Figure 5.10: Photon energy values at the makima versus the magnetic field strength for the E ⊥ B polarization Dember spectra of Ge (M).

The lower peak, previously labelled 1 in the PEM effect, is absent in the Dember effect. Nevertheless, above the fundamental edge, the Dember spectra confirm the theoretical developments which predicted the same dependence on the absorption coefficient for both the PEM and Dember effect.

Unfortunately, the broadness and relatively poor visibility of the magneto-optical structures in the Dember spectra make this effect a less attractive method of investigation. Figure 5.11 gives the visibility of the structures in the Dember spectral distribution as a function of the magnetic field.. As with the PEM effect, the visibility of these structures was expected to increase monotonically with the magnetic field. As can be seen in Figure 5.11, this is also not the case for the Dember effect and here again, no satisfactory explanation can be found for this phenomenon.

Perhaps the most interesting result obtained from our study of the Dember effect in germanium is the dependence of the magnitude of the signal on the magnetic field strength shown in Figure 5.12 The reduction in the short-circuit Dember current could possibly be associated to a large magneto-resistance phenomenon.

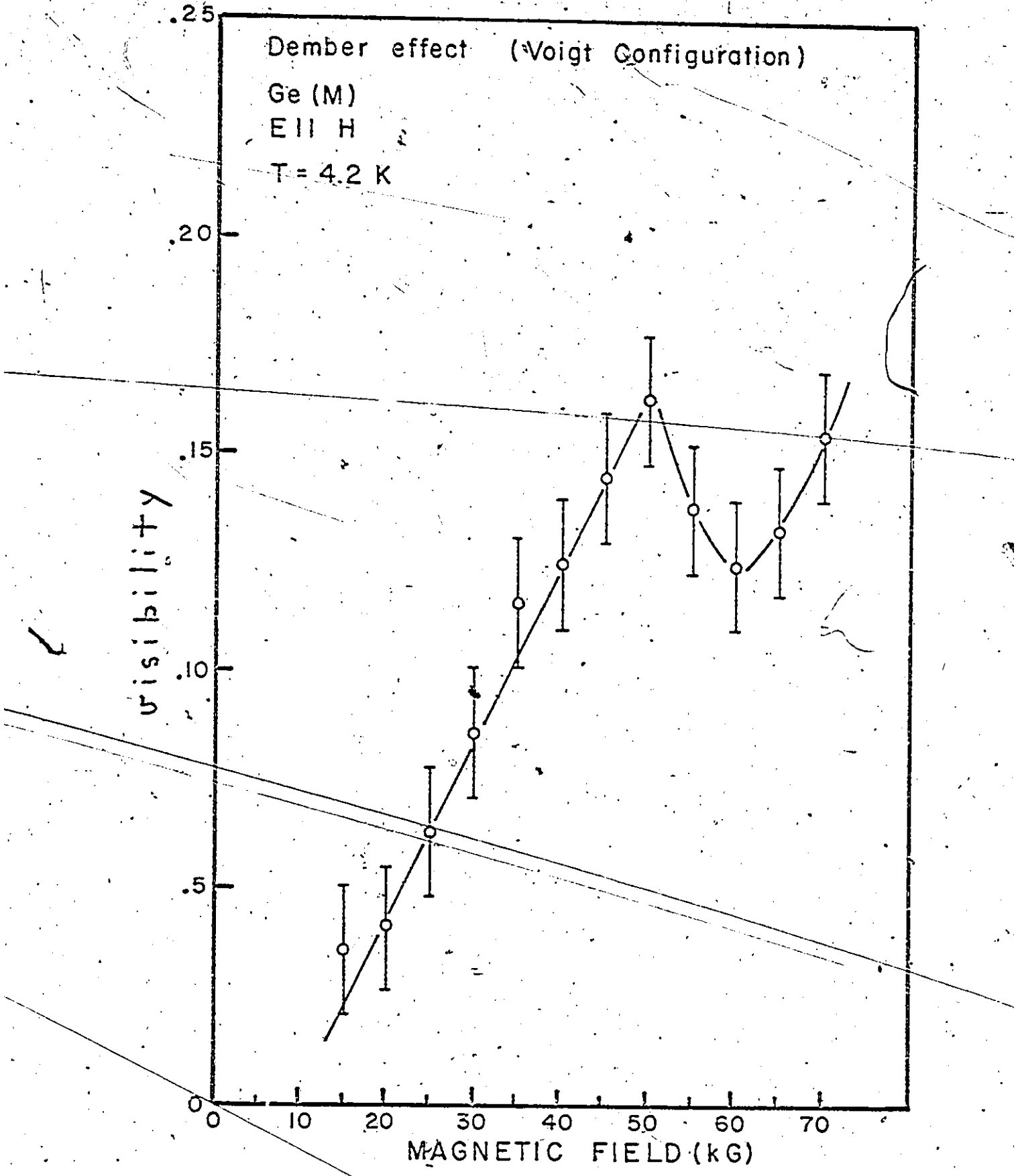

Figure 5.11: Visibility of the magneto-optical structures in the Dember spectra of germanium versus the magnetic field strength.

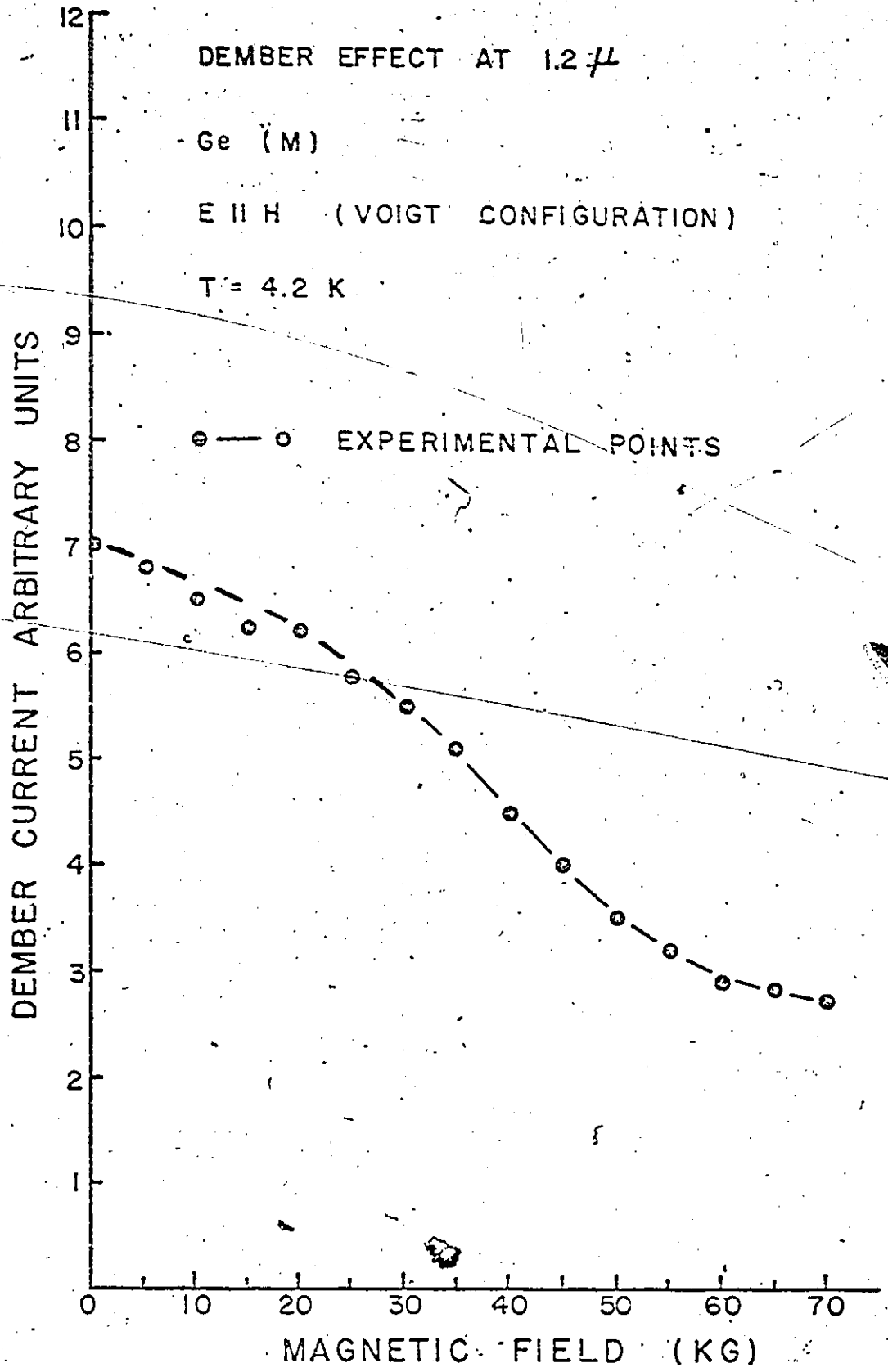

Figure 5.12: The Dember short-circuit signal as a function of the magnetic field strength.

5.1.3 The irradiated and pyrolitically coated samples

According to the line shape study presented in the previous chapter, the impurity concentration is expected to play a decisive role in the visibility and position of the magneto-optical structures. In order to verify this assumption a germanium sample, Ge (M2), had its surface protected by an aluminum oxide film in the hope of eliminating the impurities which result from surface oxidation. This preventive technique produced no significant improvement.

In order to verify that impurities did in fact reduce the visibility of the magneto-optical structures, another sample, Ge (M3), was also studied. This sample was irradiated by a neutron source. It is estimated that this treatment increased the concentration of defects by a factor of one hundred. Figure 5.13 shows the PEM spectrum of Ge (M3) for natural light at 45 kG. As expected the structures

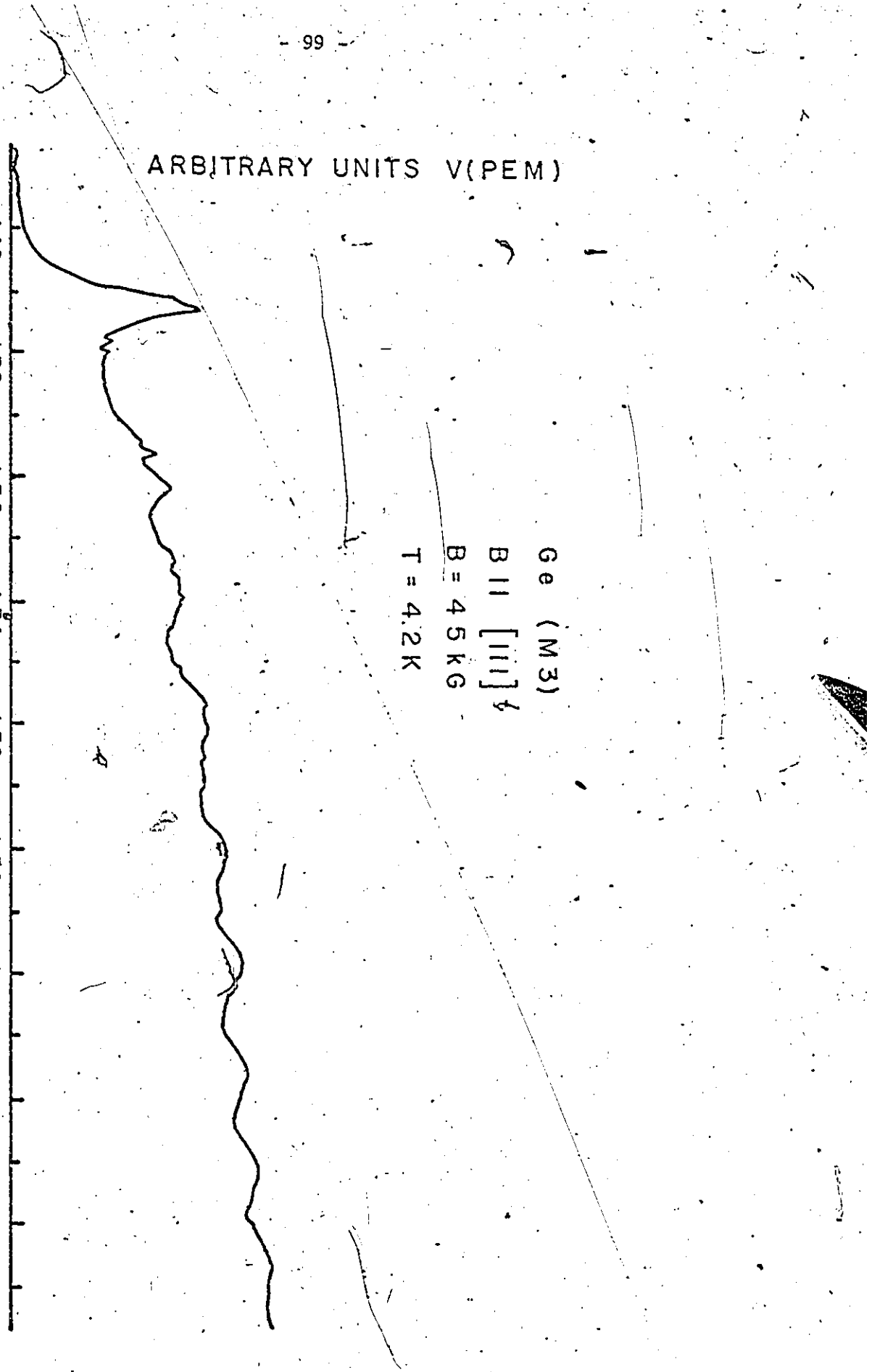

Figure 5.13: PEM spectrum of the irradiated germanium sample Ge (M3).

are much squatter as a result of the increase in the concentration of defects.

Germanium oxidizes rapidly and we must conclude that the surface of the sample (M2) was already oxidized when pyrolytically coated. As will be seen in the next three sections the pyrolytic coating process was effective in preserving cleaner surfaces for III. - V compounds. In these hetero-polar materials surface oxidation may completely modify the PEM spectral distribution.

5.2 Gallium Antimonide

Having established the PEM effect as a powerful method of investigating magneto-optical transitions in a semiconductor, we will now use this technique to obtain the band parameter values of gallium antimonide. As it turns out, the PEM spectra for this material exhibit very well resolved magneto-optical structures; so much so that the energy position of the peaks required effectively no correction prior to the Pidgeon and Brown analysis.

This analysis yields for GaSb a set of band parameter values in close agreement with those previously published. Contrary to germanium, GaSb is a hetero-polar material and, broader oscillations associated with phonon-electron interactions did appear when the semiconductor's surface was oxidized. An analysis of these broader

structures gives the LO phonon energy in GaSb.

5.2.1 The interband transitions between the Landau levels

The PEM short-circuit current spectra of the first gallium antimonide sample, GaSb (1), exhibit well resolved structures as can be seen in Figures 5.14 and 5.15. Actually, these spectra represent the best results yet obtained by the PEM technique. This is a somewhat surprising result since this material has an impurity concentration one hundred times greater than the germanium samples studied in the previous section. The type of impurity and their behaviour at low temperatures might explain this unexpected behaviour. Some twenty well defined structures could be obtained in GaSb.

Such a resolution puts the PEM technique in the same category as photoconductivity and the various modulated reflectivity techniques. Actually, we believe the PEM technique to be superior, its simplicity reducing the possibility of errors.

The fan diagrams for the above spectra are given in Figures 5.16 and 5.17. The dashed lines represent the experimental curves. Their convergence energy gives, for the direct bandgap energy of GaSb, a value of 0.812 ± 0.001 eV, which is in agreement with the normally quoted values of 0.813±0.001eV (5.6). The solid lines represent the linear theoretical predictions of Luttinger and Kohn for the following parameters of Lawaetz (5.5):

$$\gamma_1^L = 11.8$$

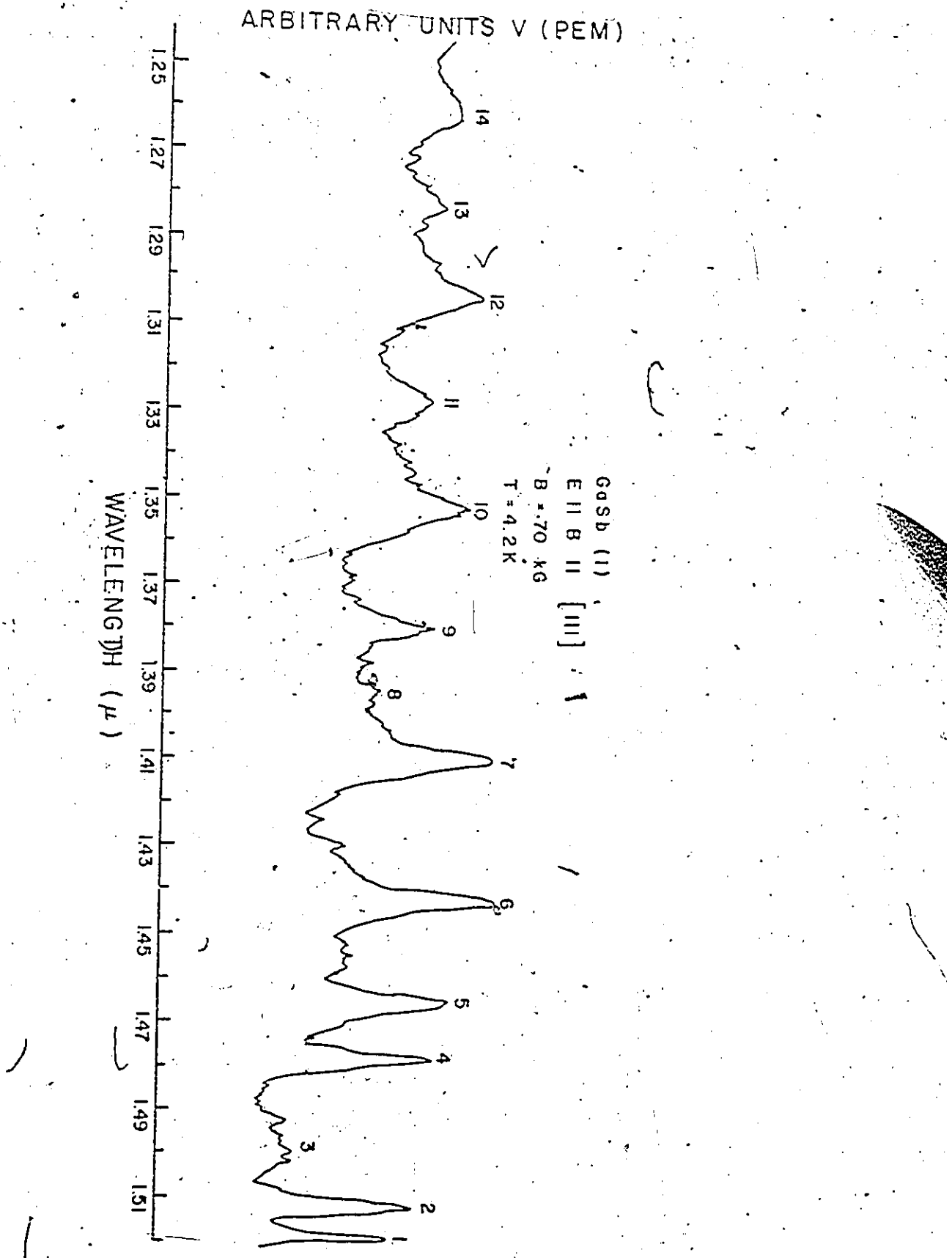

Figure 5.14: PEM spectrum for the E // B polarization of GaSb (1).

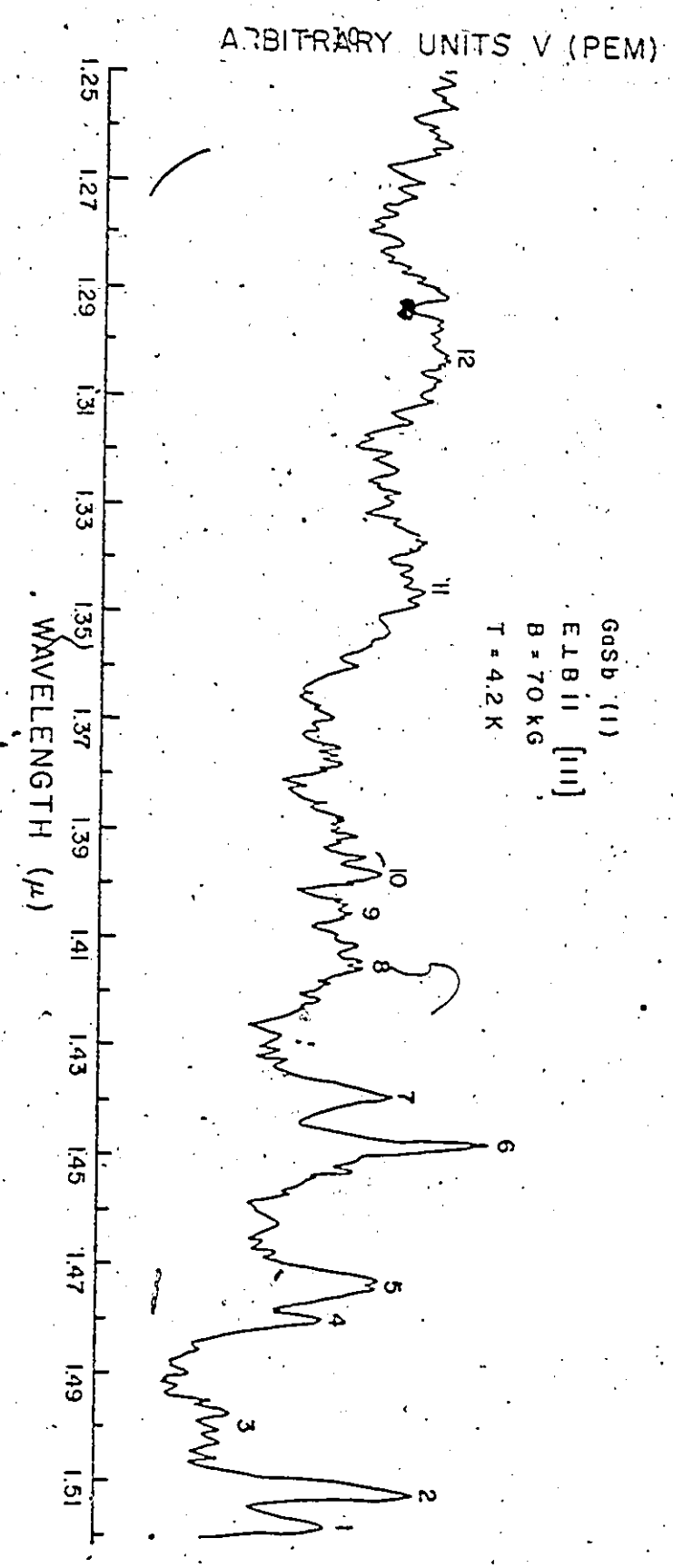

Figure 5.15: PEM spectrum for the E ⊥ B polarization of GaSb (1).

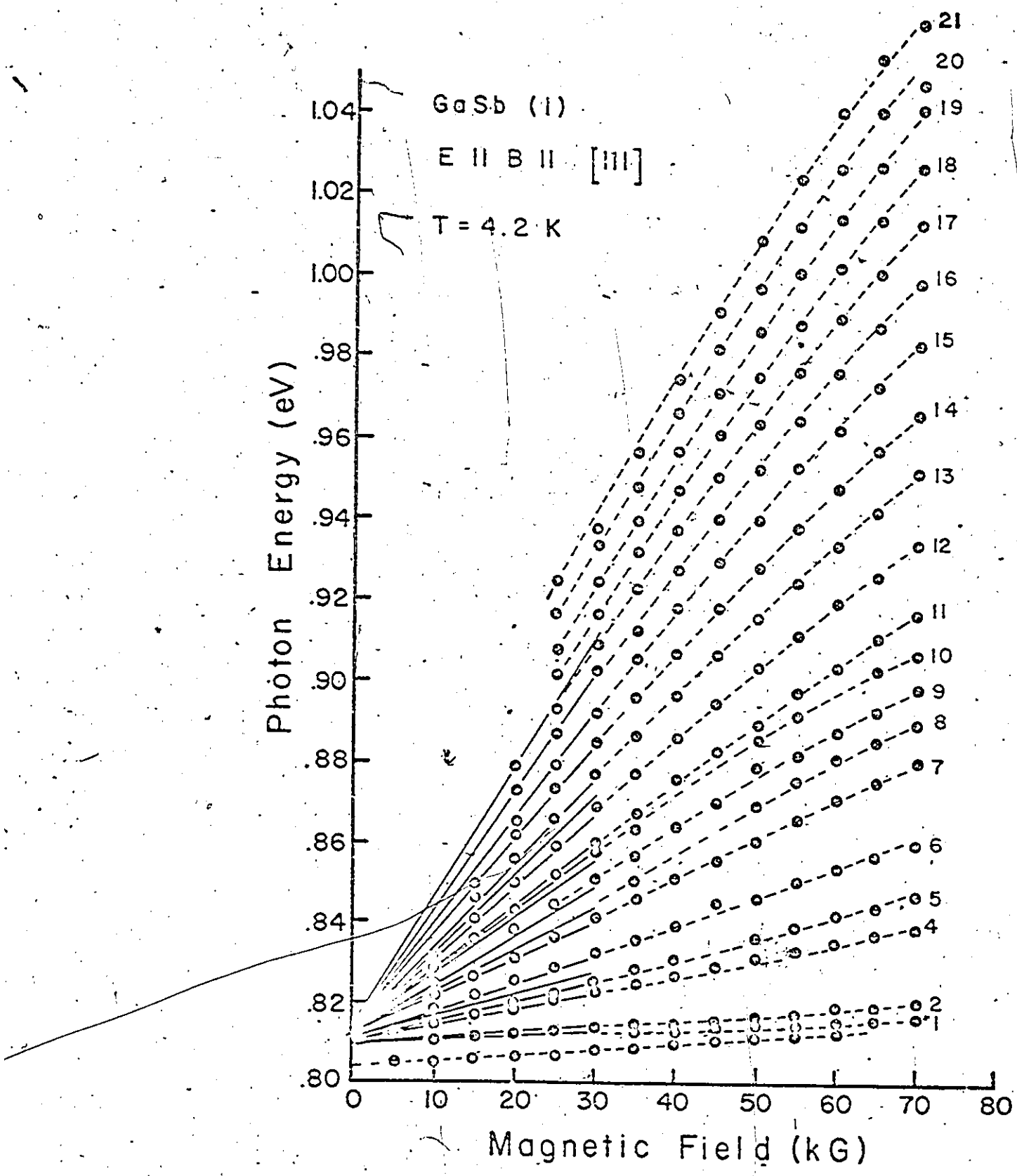

Figure 5.16: Photon energy values at the maxima versus the magnetic field strength for the E // B polarization PEM spectra of GaSb (1).

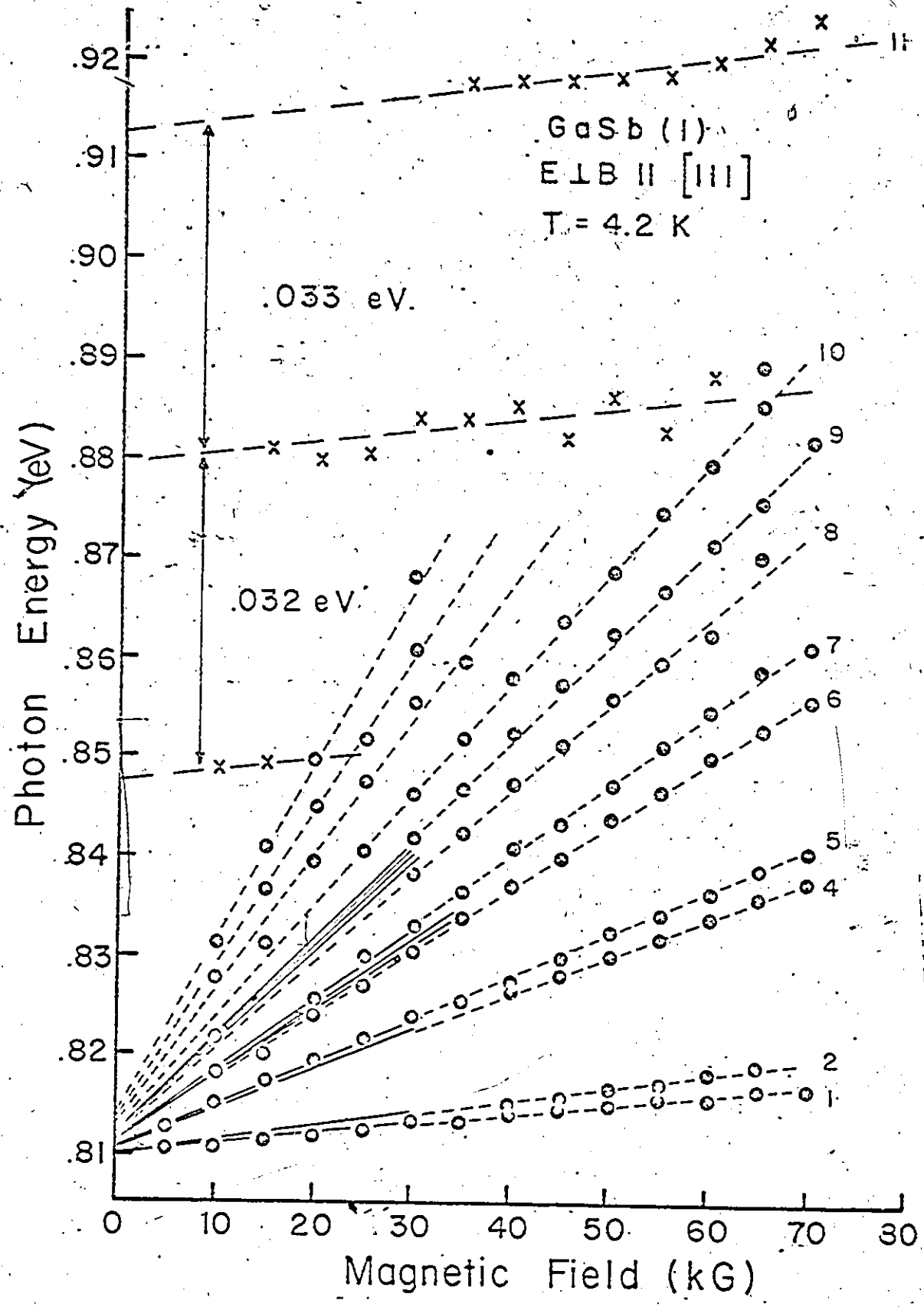

Figure 5.17: Photon energy values at the maxima versus the magnetic field strength for the E ⊥ B polarization PEM spectra of GaSb (1).

$\gamma_2^L = 4.03$

$\gamma_3^1 = 5.26$

$k^L = 3.18$

$m_c/m = 0.045$

$g_c = -7.12$

Here again, a preliminary comparison with the linear theory allows identification of the experimental curves. The heavy-hole transitions $B^-(6)$ to $B^-(15)$, see curve 12 to 21 for the E // B polarization spectra of GaSb (1), were then analysed using the Pidgeon and Brown scheme and the following fixed parameters:

$$\gamma_3^L - \gamma_2^L = 1.3 \qquad (5.7)$$

$\varepsilon_g = 0.812$ eV

$\Delta = 0.749$ eV (5.6)

$F = -1.5\ (h^2/m)$ (5.7)

The set of band parameter values obtained for GaSb is given in Table 5.4 where it is compared to other experimental and theoretical sets of values. Our root mean square deviation of 1.8 meV is somewhat larger than those of the other experiments; however, we obtain a closer agreement with the theoretical results of Lawaetz (5.5).

Table 5.4

Comparison of the band parameter values for GaSb determined in the present experiment with previously published values

Parameter	Present Experiment	Filion (5.8)	Reine (5.7)	Lawaetz (5.5)
m_c/m	0.046 ± 0.001	0.039 ± 0.001	0.042 ± 0.001	0.045
γ_1^L	12.6 ± 0.5	14.5 ± 0.4	13.3 ± 0.4	11.8
γ_3^L	5.2 ± 0.2	6.6 ± 0.2	5.7 ± 0.2	5.26
k^L	3.0 ± 0.5	4.6 ± 0.6	3.5 ± 0.6	3.18
g_c	-7.1 ± 0.1	-8.4 ± 0.8	-7.8 ± 0.8	-7.12
m_{lh}/m	0.045 ± 0.002	0.038 ± 0.002	0.042 ± 0.002	0.046
m_{hh}/m	0.36 ± 0.07	0.44 ± 0.15	0.40 ± 0.16	0.49
E_p	23.1 ± 0.1eV	26 ± 1eV	25 ± 2eV	22.4 eV

For example if we compare the results for the conduction band effective mass parameter, Lawaetz theoretically predicts $m_c/m = 0.045$ and we get $m_c/m = 0.0455$. The values reported for the other two experiments are much lower, $m_c/m = 0.039$ and 0.042. Contrary to germanium, our band parameter values for GaSb differ from those previously published (5.7, 5.8) but they confirm the theoretical predictions of Lawaetz (5.5).

If we now return to the PEM spectra for the $E \perp B$ polarization, see Figure 5.15, we notice that broader oscillations appear at the high energy end of the spectrum. In the $E \parallel B$ polarization, these structures are probably masked by the sharp Landau structures. As can be seen in the corresponding fan diagram, Figure 5.17, the energy positions for the maxima of these broader structures do not converge to the band gap energy and their separation energy remains constant with the magnetic field. They clearly do not represent interband transitions between Landau levels and they were associated to phonon-electron interactions.

5.2.2 The phonon-electron interactions

The broader structures observed in GaSb (1) appear at the higher energy end of the spectrum. There, the absorption process occurs in a very thin layer at the surface of the semiconductor. Since the surface oxidation of GaSb (1) is also believed to be shallow, it was reasoned that a more thorough surface oxidation might

possibly enhance these broader structures. Following this line of reasoning, a second sample, GaSb (2), identical to the previous one, GaSb (1), was heated to 400 K in air. When studied under the previous condition, its spectral distribution exhibited the large smooth oscillations shown in Figure 5.18. It is believed that surface oxidation increases the impurity concentration, thus reducing τ_l at the surface of the sample so that the condition necessary to observe LO phonon transitions; $\tau_{op} < \tau_l < \tau_{ac}$, is satisfied.

According to the model by Habegger and Fan the minimum of the larger oscillations correspond to the LO phonon transitions. Figure 5.20 gives the energy position of the minima versus the magnetic field. The minima are equally spaced and their separation energy remains constant with the magnetic field. The energy position of the minima also increases with the field in the same manner as the bottom of the conduction band. Figure 5.21 plots the intercept energies of the minima at zero field versus their transition order. The photon energy of the extrapoled zeroeth order gives, for the bandgap energy, 0.812 ± 0.001 eV, confirming our previous result. The slope of this graph yields for the separation energy of the oscillations 34.6 meV. Using the following equation (4.28):

$$\varepsilon_\ell = \varepsilon_g + \ell\hbar\omega_o \, (1 + m_c/m_{hh}) \qquad (5.4)$$

and the ratio $m_c/m_{hh} = 0.13$, see table 5.4, we get for the LO phonon energy in GaSb, 30.7 meV. This is in close agreement with

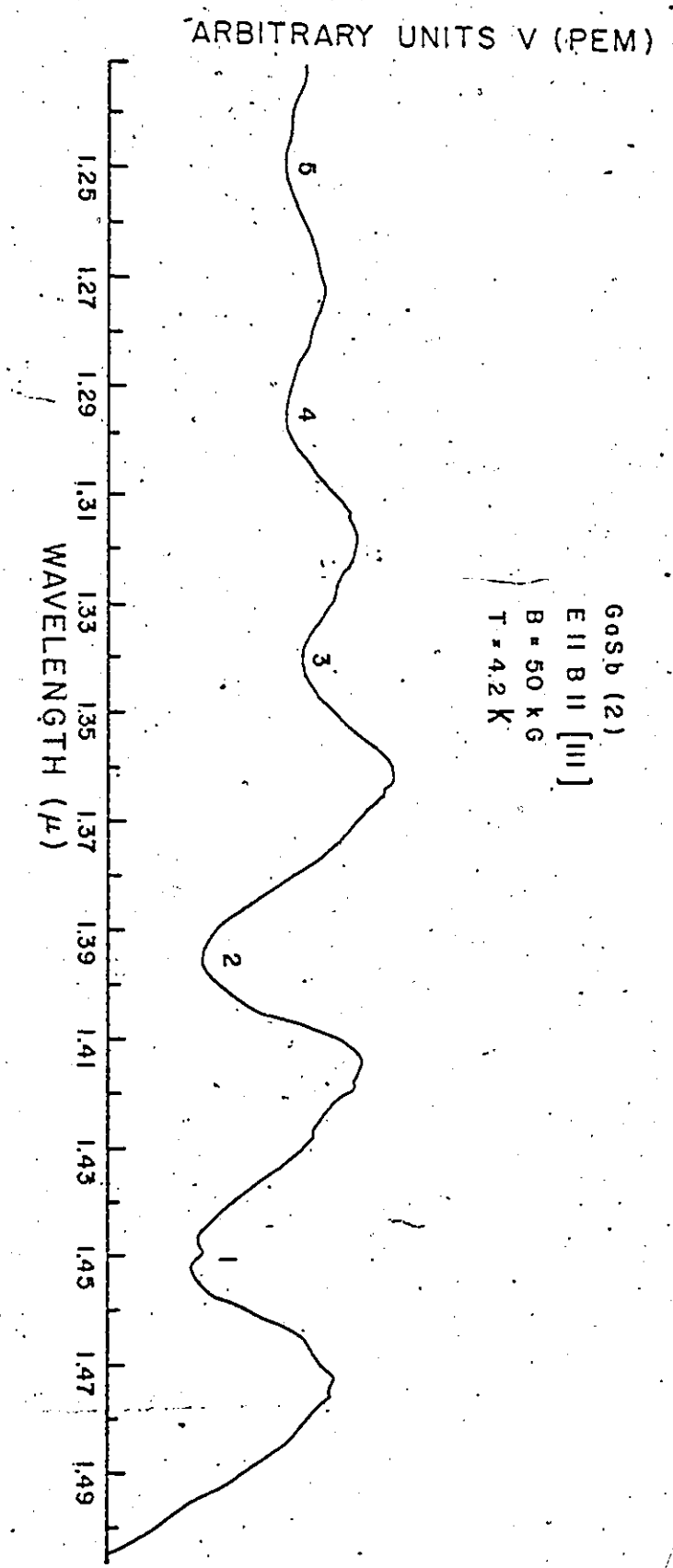

Figure 5.18: PEM spectrum for the E // B polarization of GaSb (2) at 50 kG.

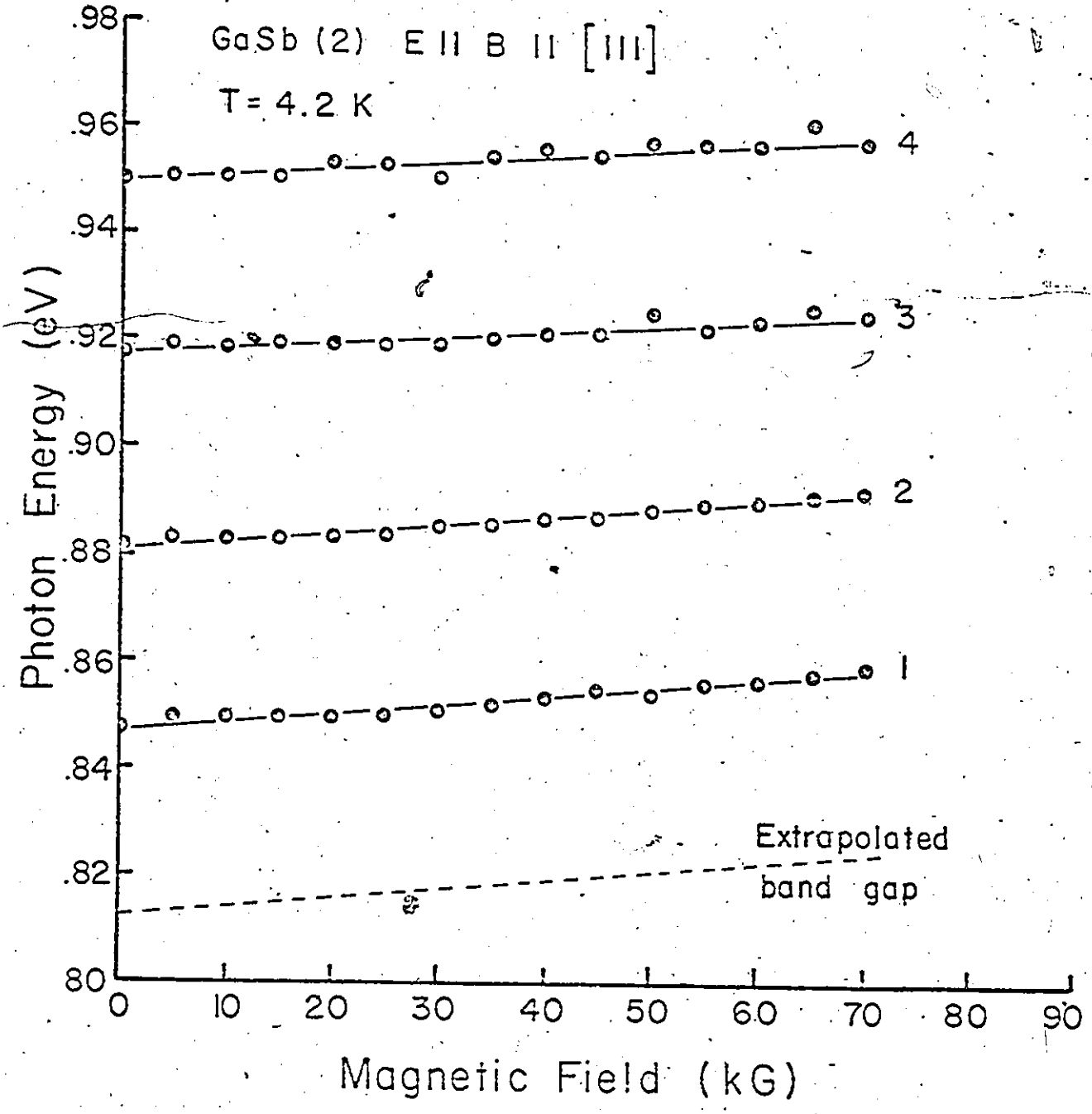

Figure 5.19: Photon energy values at the minima versus the magnetic field strength for the E // B polarization PEM spectra of GaSb (2).

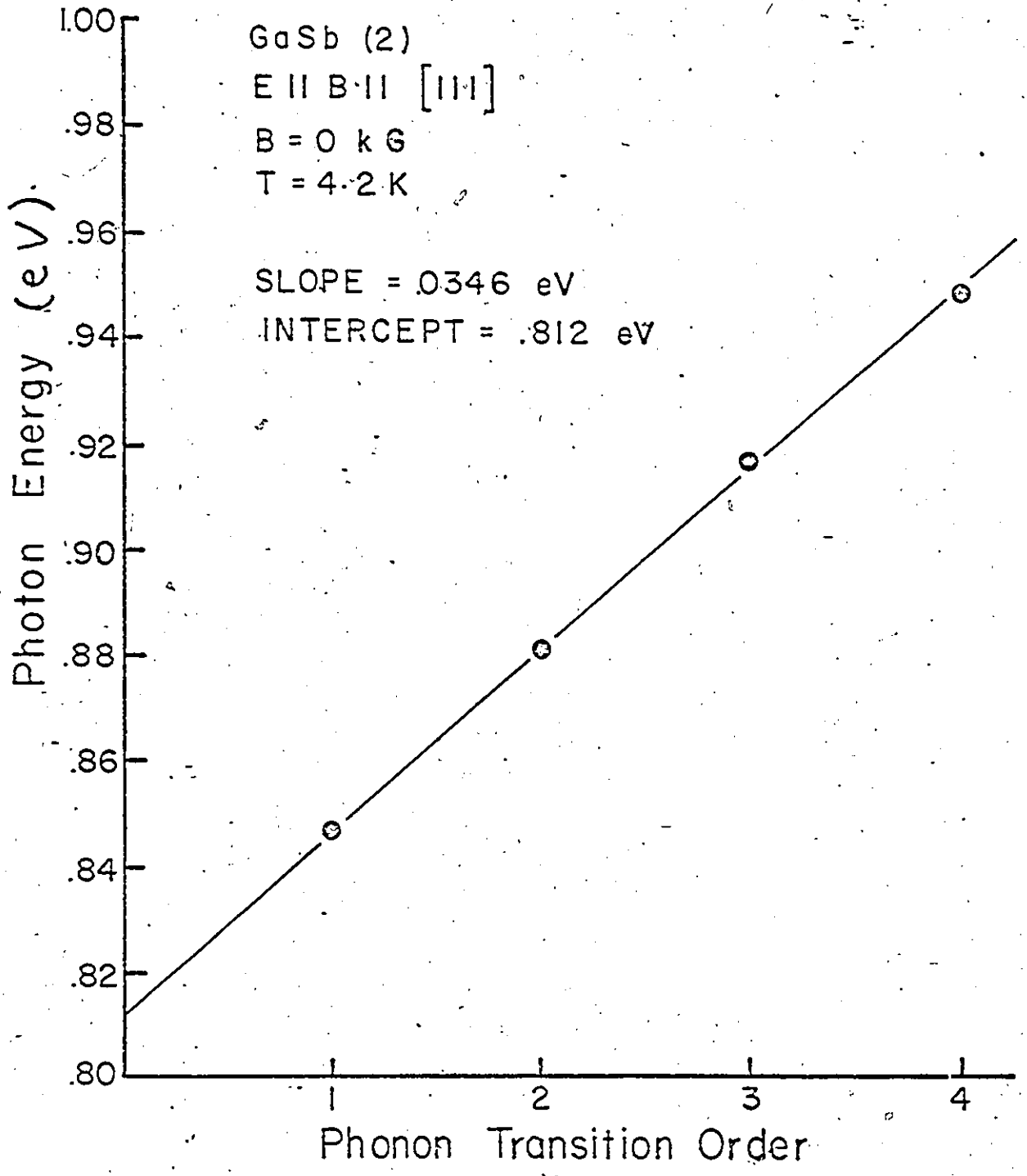

Figure 5.20: Plot of the extrapolated photon energy values at B = 0 versus the phonon transition order.

Haas and Hennis (5.9), who report a value of 29.8 meV obtained by infrared reflectivity.

5.3 Indium Phosphide

Indium phosphide is a III - V compound which has not been the subject of many investigations, the reason being that this material is difficult to obtain in a pure form. To the best of the author's knowledge no experiment treating interband magneto-optical transitions in InP has ever been reported prior to this work. Magneto-optical structures associated with interband transitions between Landau levels were observed here in the spectral distribution of the PEM effect in InP. The energy position of the minima rather than the maxima corresponds to the theoretical predictions for the transition energies. The so-called anomalous PEM effect discussed in section 4.1.3 is believed to account for such a behaviour. InP, as GaSb, is also a hetero-polar material and broader structures did appear when the surface of the semiconductor was oxidized. The analysis of these wide oscillations gives the LO phonon energy in InP.

5.3.1 The interband transitions between the Landau levels

The PEM short-circuit current spectra of the pyrolytically

coated InP sample, InP (1), are shown in Figures 5.21 and 5.22 for the E // B and E ⊥ B polarizations respectively. The magneto-optical structures appear rather squat in comparison to the previous results obtained for GaSb. This is not an unexpected result if we remember that the conduction band effective mass for InP is approximately twice that for GaSb. The first maximum, 1P, appears excitonic in nature while the successive minima (1M, 2M,...) are believed to result from interband transitions between the Landau levels. At the high energy end of the PEM spectra, a broad structure, labelled 1s, appears. Assuming that the structure originates from a transition between the split-off band and the conduction band and this has been verified by subsequent wavelength modulation experiments (5.10), we find for the spin-orbit splitting energy, 0.102 ± 0.006 eV. This value, not a precise measurement, agrees with the results of Shaklee et al. (5.11) 0.11 eV, using electroreflectivity at 300K.

The fan diagrams for the above spectra are given in Figures 5.23 and 5.24. The dashed lines represent the experimental curves. Their convergence energy gives, for the direct band gap energy of InP, 1.423 ± 0.001 eV which is in close agreement with Turner et al. (5.12) who report a value of 1.4205 eV found by optical absorption at 6 K. The solid lines represent the linear theoretical predictions of Luttinger and Kohn using the following parameters of Lawaetz (5.5):

$$m_c/m = 0.08$$

$$\gamma_1^L = 6.28$$

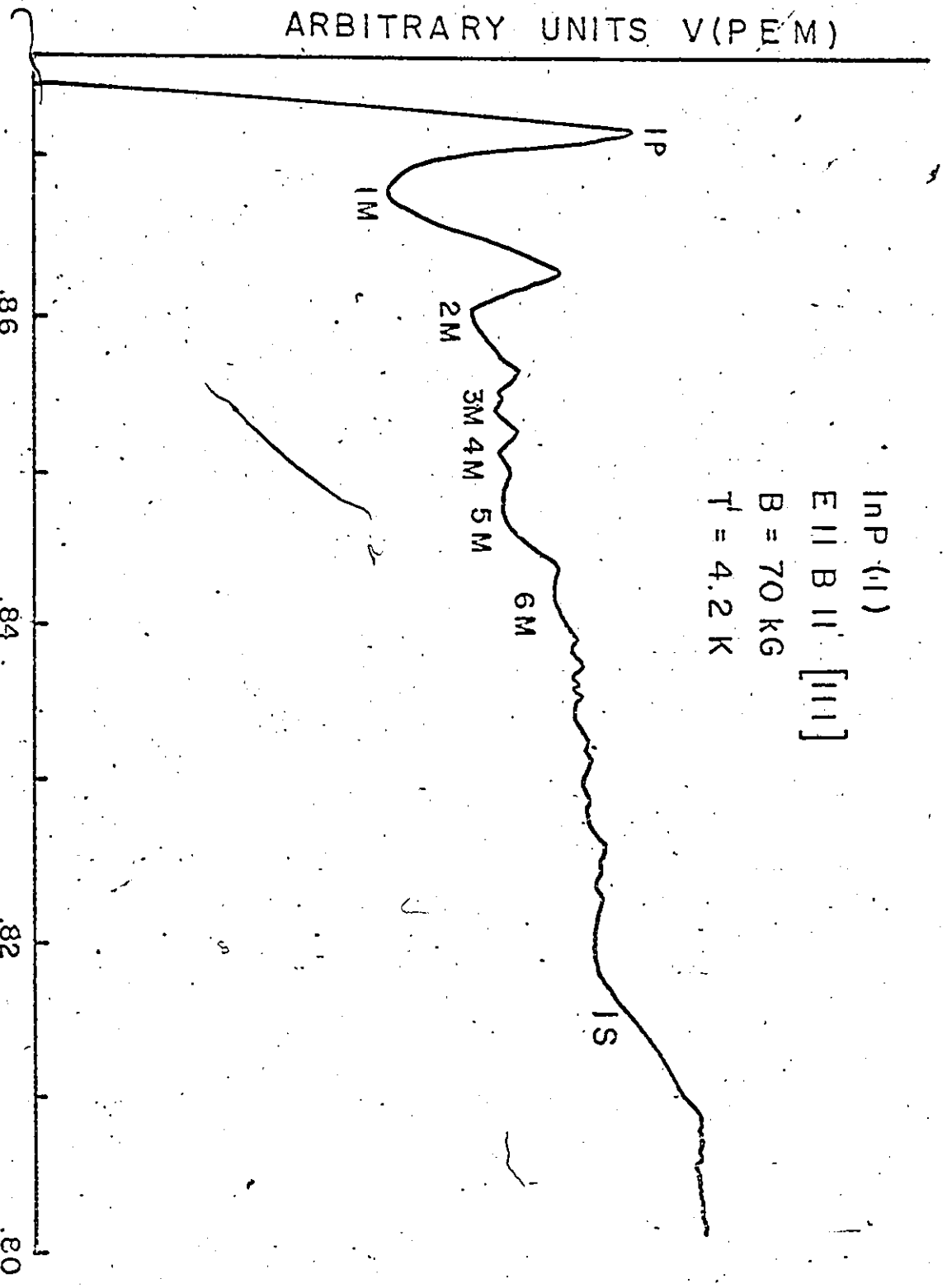

Figure 5.21: PEM spectrum for the E // B polarization of InP (1).

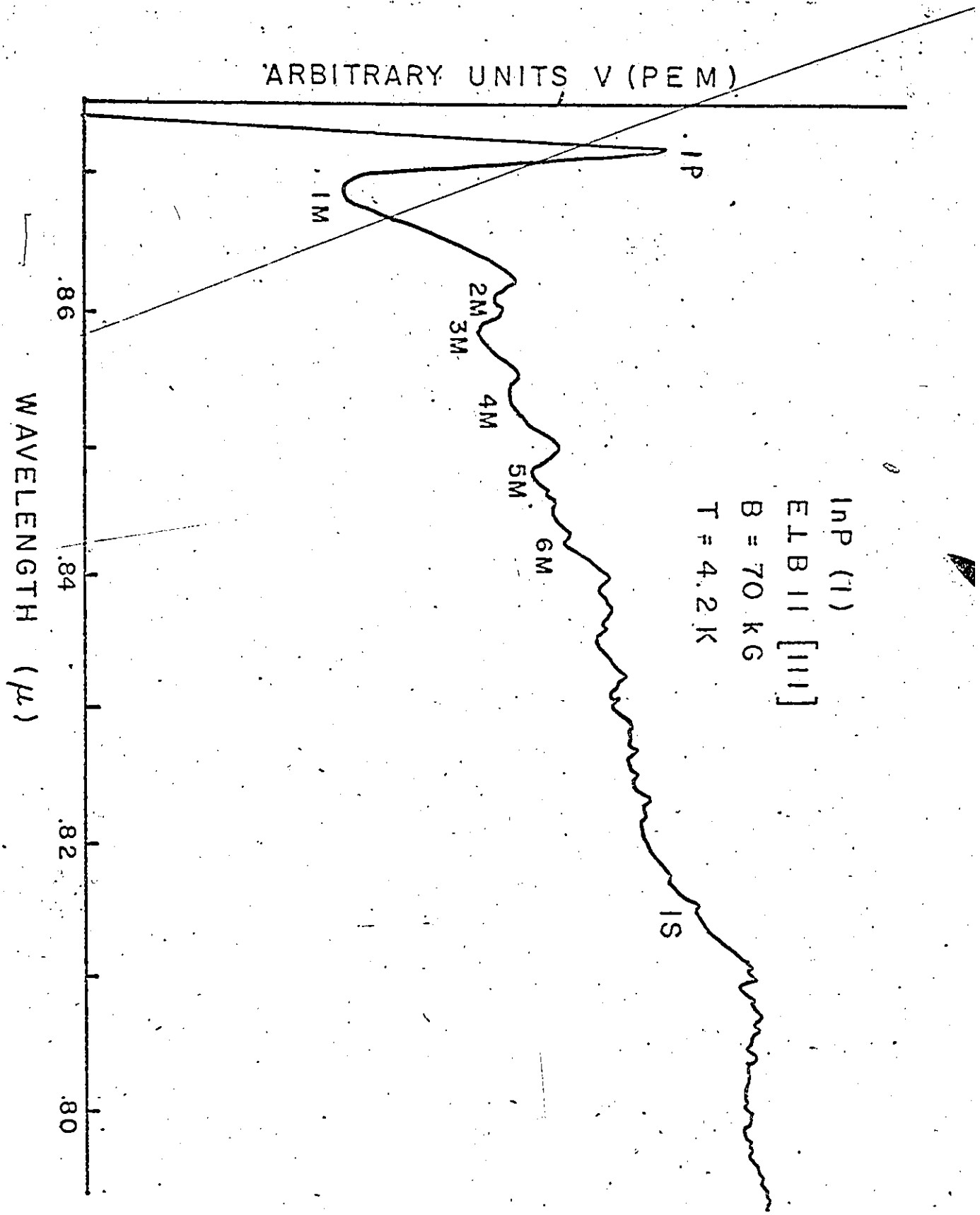

Figure 5.22: PEM spectrum for the E ⊥ B polarization of InP (1).

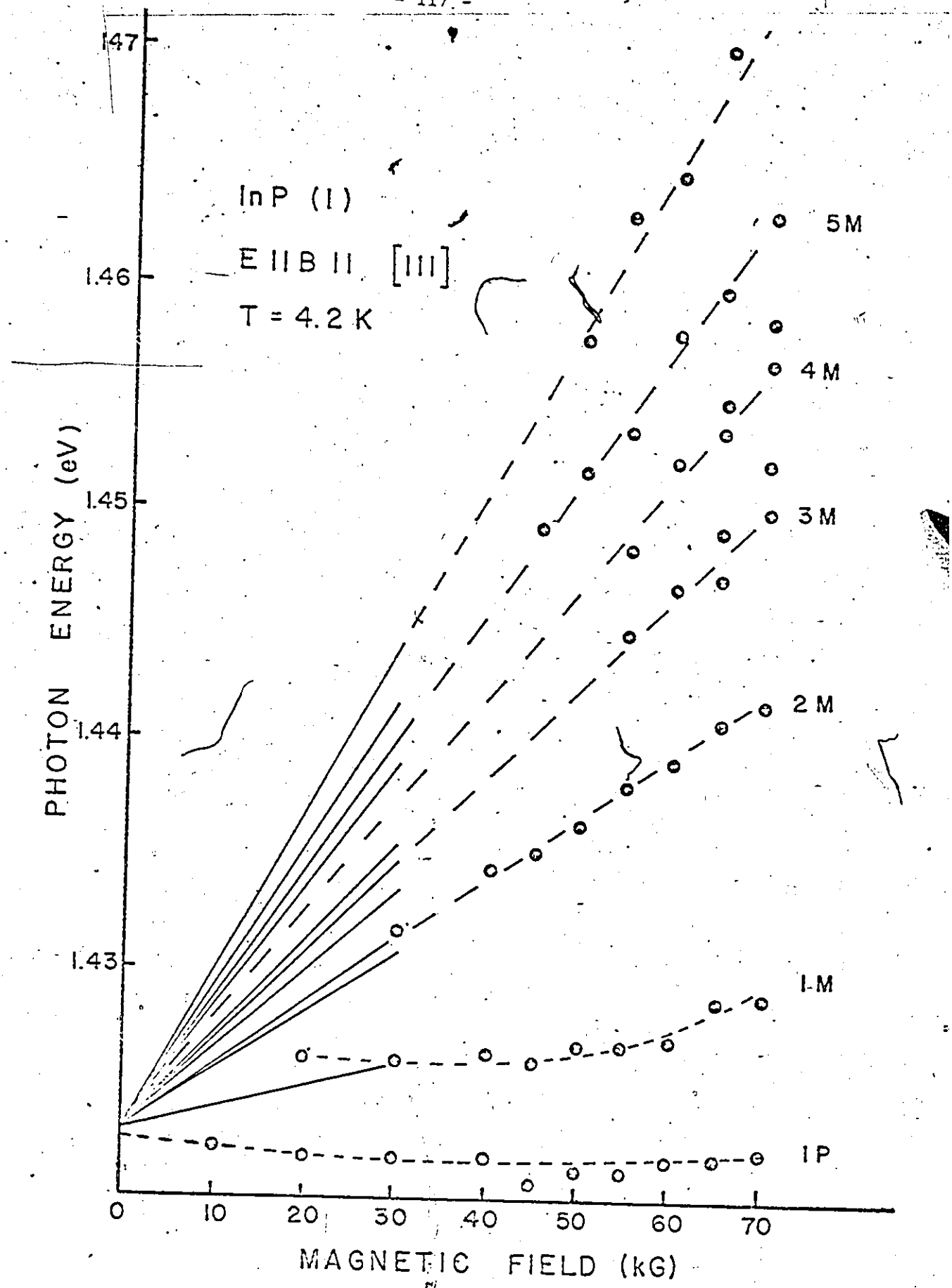

Figure 5.23: Photon energy values at the minima versus the magnetic field strength for the E // B polarization PEM spectra of InP (1).

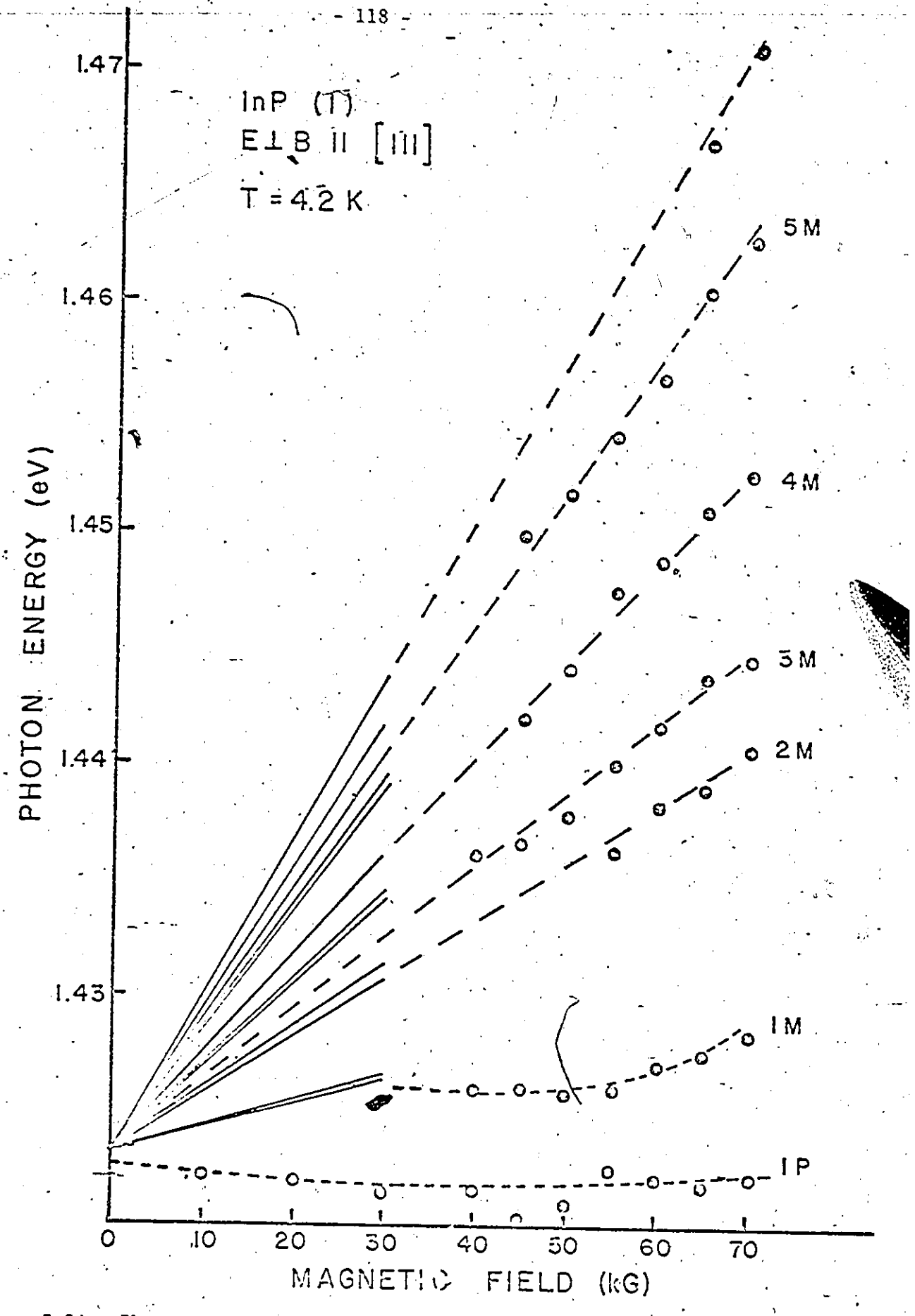

Figure 5.24: Photon energy values at the minima versus the magnetic field strength for the E⊥B polarization PEM spectra of InP (1).

$$\gamma_2^L = 2.08$$

$$\gamma_3^L = 2.76$$

$$k^L = 1.47$$

$$g_c = 1.20$$

Again, this preliminary comparison with the linear theory allows the identification of the experimental curves. The heavy-hole transitions $B^-(3)$ and $B^-(4)$, see curve 4M and 5M for the E // B polarization spectra of InP (1), were then compared to the predictions of Pidgeon and Brown for the above parameters of Lawaetz (5.5). These parameters along with the values for the direct bandgap energy and the spin-orbit splitting energy give a root mean square deviation of only 1.3 meV on the experimental points.

The good agreement between the energy position of the minima and the predictions of Pidgeon and Brown using the theoretical band parameter values of Lawaetz indicates that the minima rather than the maxima must correspond to the interband transitions between Landau levels in InP (1). Our line shape study of magneto-optical structures indicates that minima cannot correspond to absorption edges. The only explanation for the above behaviour is that we are observing the anomalous PEM effect discussed in section 4.1.3.

5.3.2 The phonon-electron interaction

In InP the exposure time to air necessary for installation sufficies to oxidize the surface of the sample. In the absence of a protective aluminium oxide film, the sample InP (2), identical to the previous sample InP (1), exhibited in its PEM spectral distribution the large smooth oscillations associated with phonon-electron interactions. Figure 5.25 shows these broader structures. Using the same analysis as for GaSb, the energy position of the minima versus the magnetic field are given in Figure 5.26 and the intercept energies versus the transition order are plotted in Figure 5.27. The photon energy of the zeroeth order then gives for the direct bandgap energy of InP, 1.432 ± 0.001 eV. The slope of the graph gives for the separation energy of the oscillations, 48.5 meV. Using this result and the following ratio, $m_c/m_{hh} = 0.088$ (5.5), we get for the LO phonon energy, 44.6 meV. This is in good agreement with Hilsum et al. (5.13) who report a value of 42.7 meV. found by Raman scattering.

5.4 Gallium Arsenide

In GaAs, contary to the previously studied semiconductors, the photoconductivity spectra exhibited better resolved magneto-optical structures than the PEM effect. Therefore, in the first

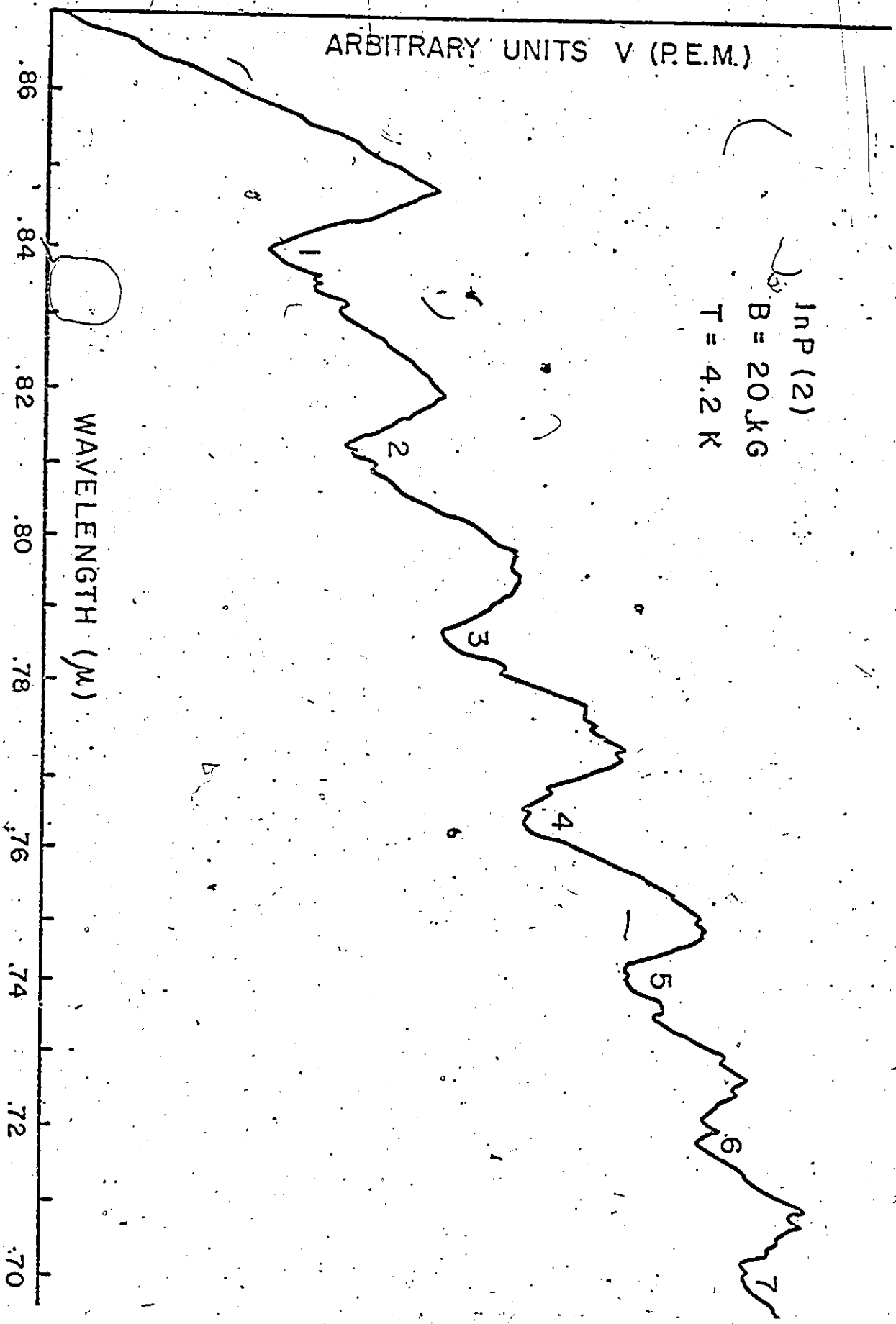

Figure 5.25: PEM spectra of InP (2) at 20 kG.

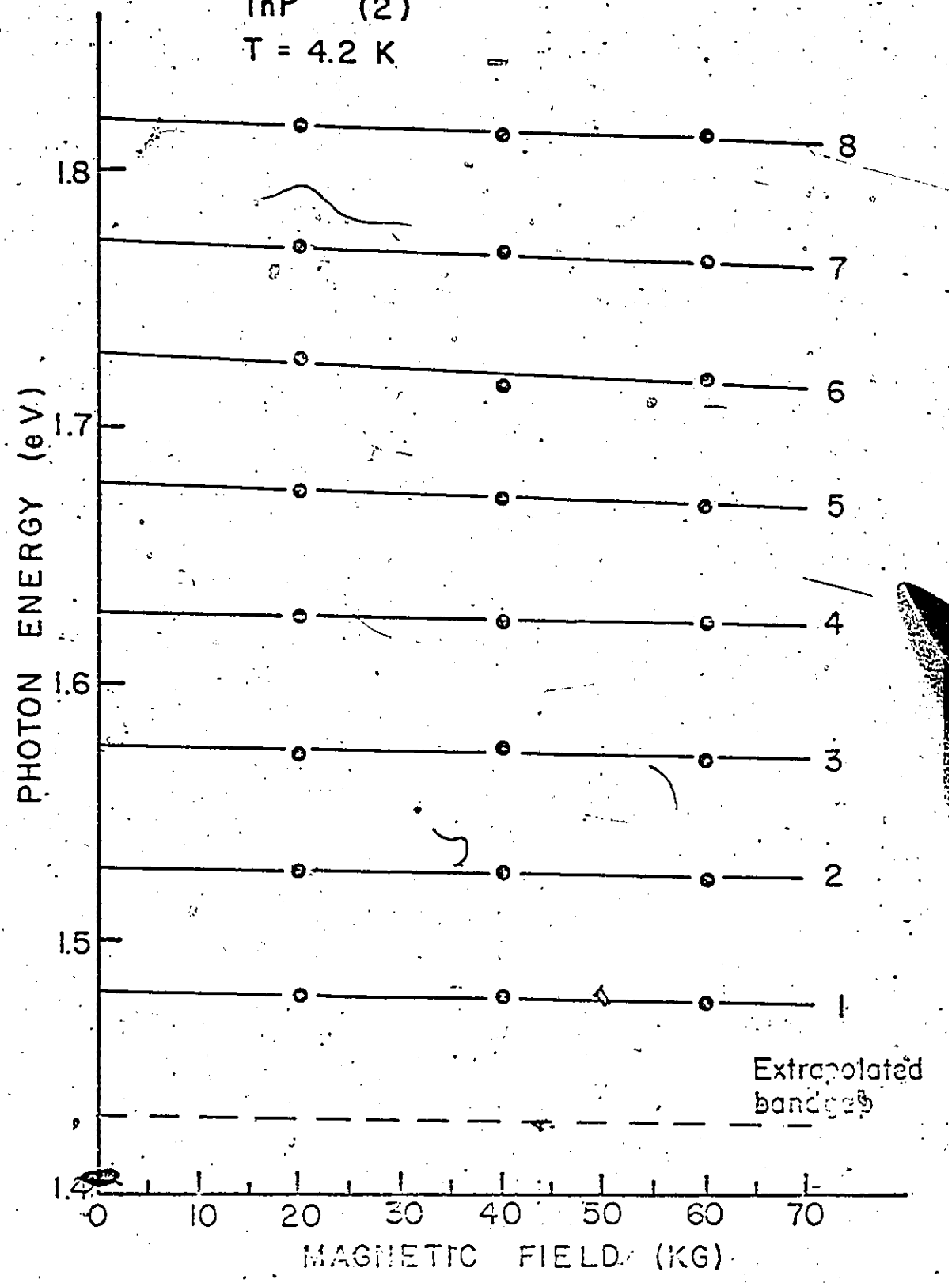

Figure 5.26: Photon energy values at the minima versus the magnetic field strength for the PEM spectra of InP (2).

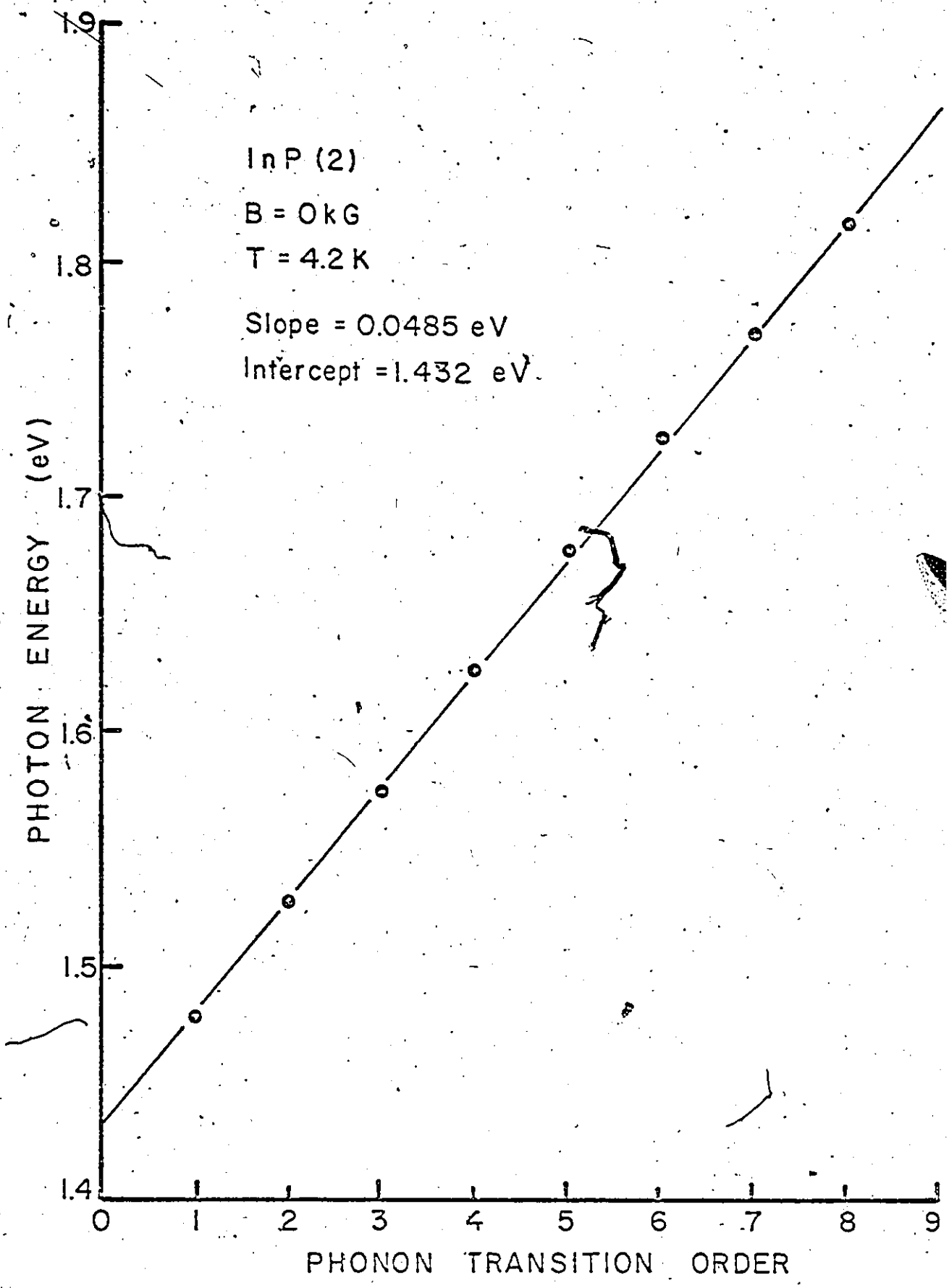

Figure 5.27: Plot of the extrapolated photon energy values at B = 0 versus the phonon transition order.

part of this section photoconductivity will be reviewed and compared to the PEM effect.

Two GaAs crystals were studied; an epitaxial material which exhibited magneto-optical structures associated with interband transitions between Landau levels and a high resistivity material which exhibited the wider structures associated with phonon-electron interactions. By comparing our results on the high resistivity material to those of Nahory (5.14) on epitaxial material, we were able to gain some insight into the mechanism relating the oxidation process to the observation of LO phonon transitions.

5.4.1 Photoconductivity

According to Uchinokura and Fan (5.15), the variation of density of states produced by a magnetic field causes the scattering to vary with the carrier energy. Scattering is high when the carrier energy is close to a Landau level where the density of states is large. This introduces structures in the photoconductivity where the minima are expected to denote the interband magneto-optical transitions between the Landau levels of a semiconductor. The findings of Filion and Fortin (5.8) in GaSb contradict the results of Uchinokura and Fan. Filion and Fortin explain the contradiction by supposing that the photo-sensitivity of GaSb is maximum at the surface of the sample.

Our photoconductivity results of GaSb agree with those of

Filion and Fortin. Figure 5.28 shows a photoconductivity spectrum obtained for GaSb (1) at 70 kG and compares it with a PEM spectrum obtained with the same conditions. As for the PEM effect, the maxima in the photoconductivity spectrum denote the magneto-optical interband transitions. In the case of GaSb the sensitivity of the PEM effect to changes in the absorption coefficient is greater than that for photoconductivity. Figure 5.29 also compares the spectral distribution of photoconductivity and the PEM effect for the oxidized sample, GaSb (2), at 30 kG. Here the PEM effect is more sensitive to changes in mobility or recombination lifetime than photoconductivity. In GaSb the PEM effect is a better method of investigation than photoconductivity. This is also true for germanium and InP, but not true for GaAs.

5.4.2 The epitaxial material

The photoconductivity spectrum of a pyrolytically coated epitaxial GaAs sample, GaAs (1), is shown in Figure 5.30. The next figure, 5.31, shows the PEM spectrum of the same sample under the same conditions. Clearly, the spectral resolution of photoconductivity is superior to that of the PEM effect in the epitaxial GaAs studied. Since the crystal orientation of the epitaxial film in the direction of the magnetic field was unknown, only natural light was used in obtaining the above spectra. Even so, the photoconductivity spectra exhibit well resolved structures. The minima labelled 1, 2,

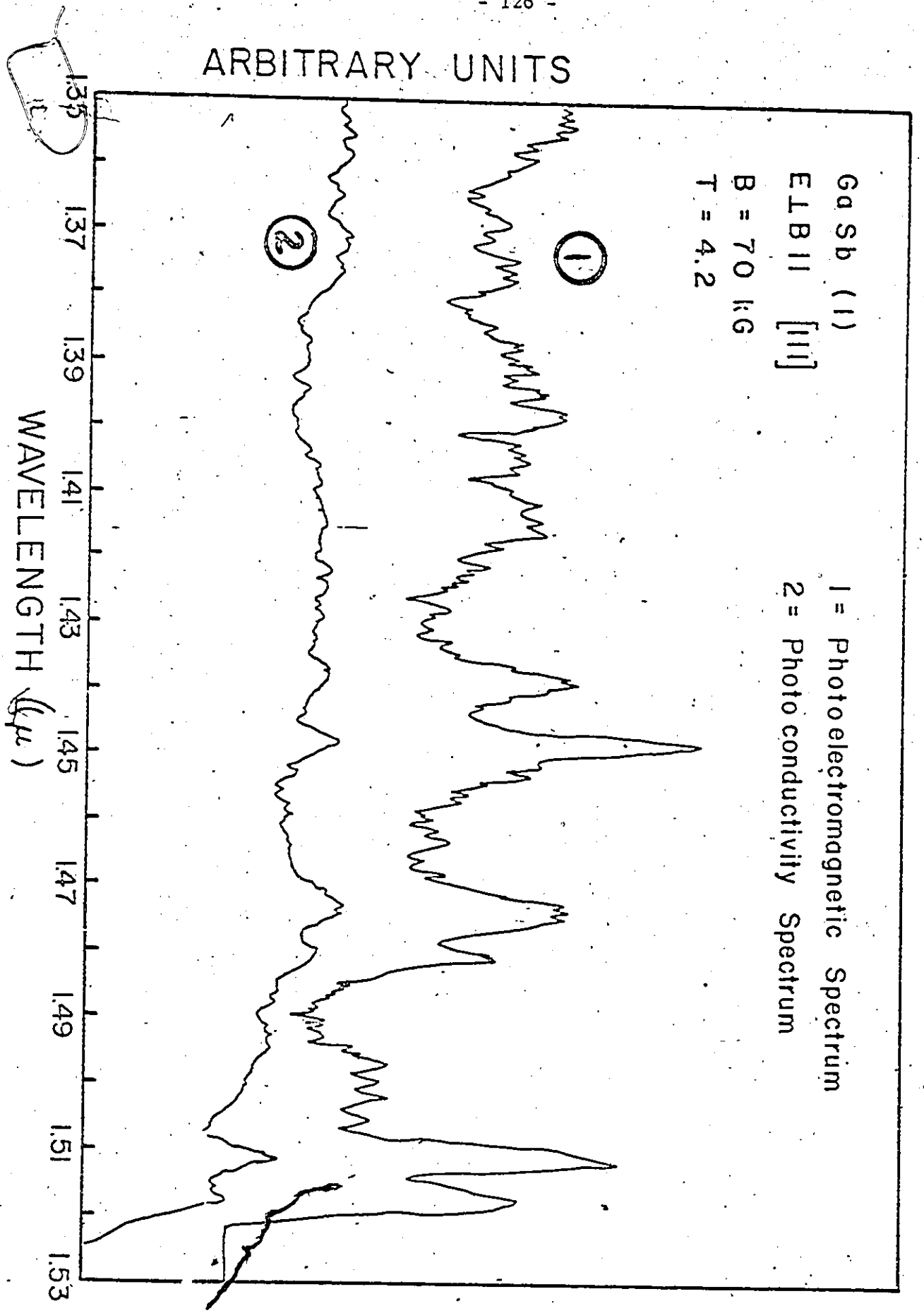

Figure 5.28: Comparison between the PEM spectrum and photoconductivity spectrum of GaSb (1) at 70 kG.

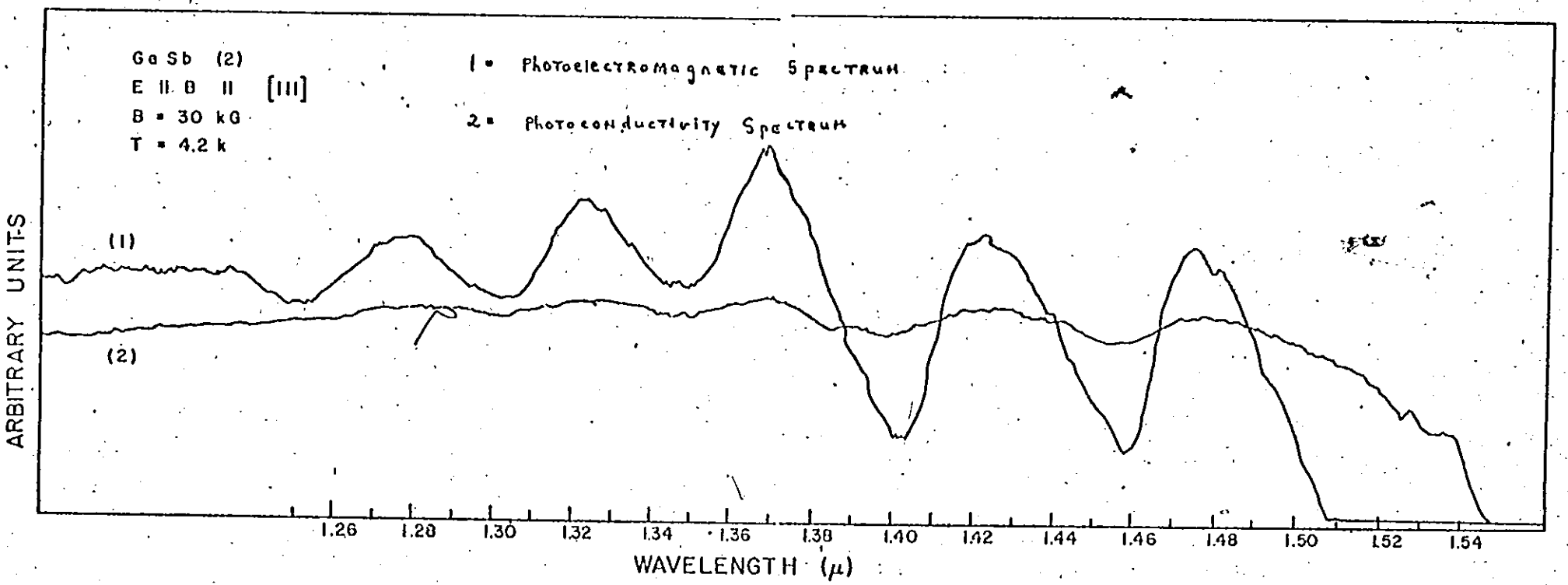

Figure 5.29: Comparison between the PEM spectrum and photoconductivity spectrum of GaSb (2) at 30 kG.

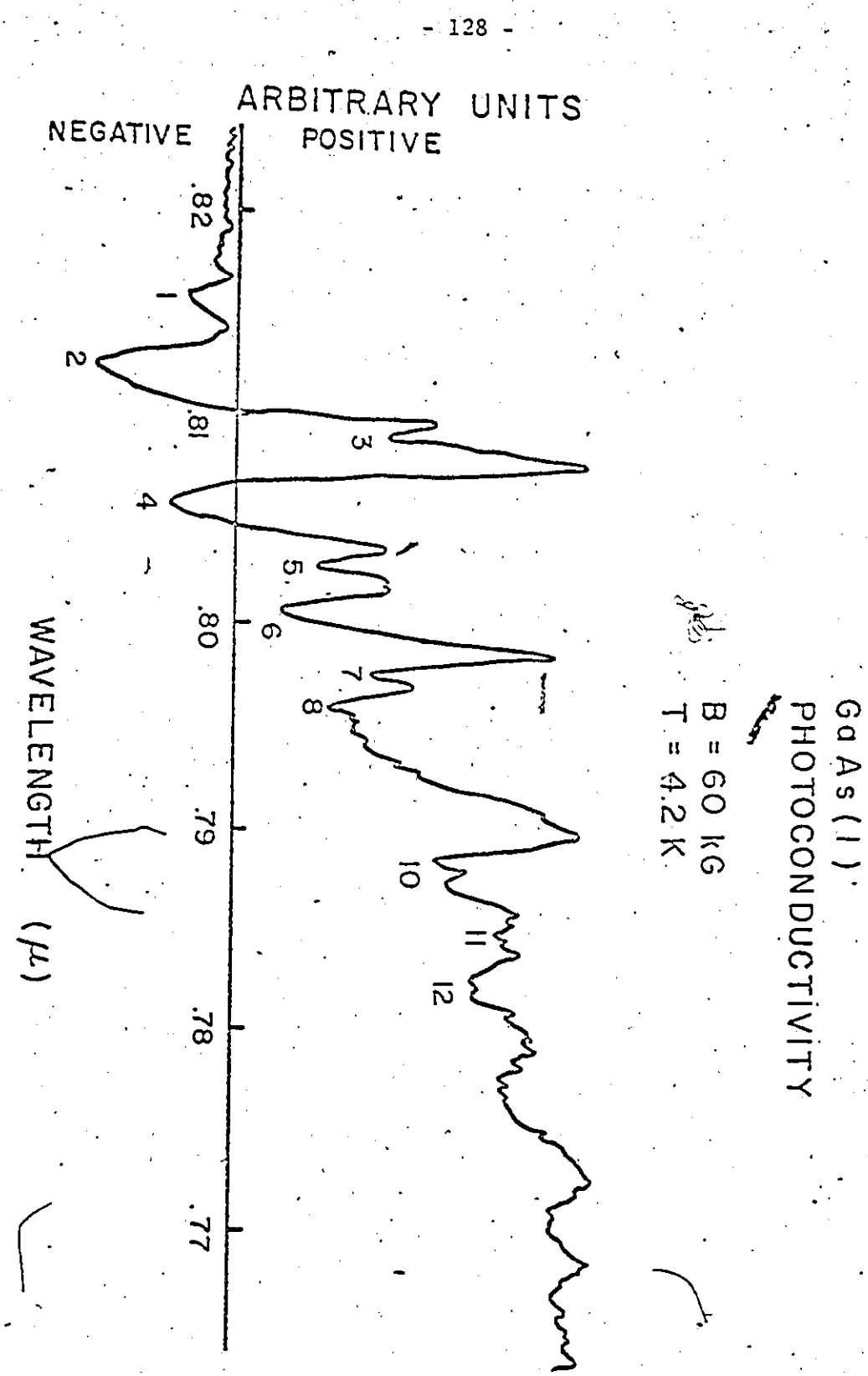

Figure 5.30:- Photoconductivity spectrum of GaAs (1) at 60 kG.

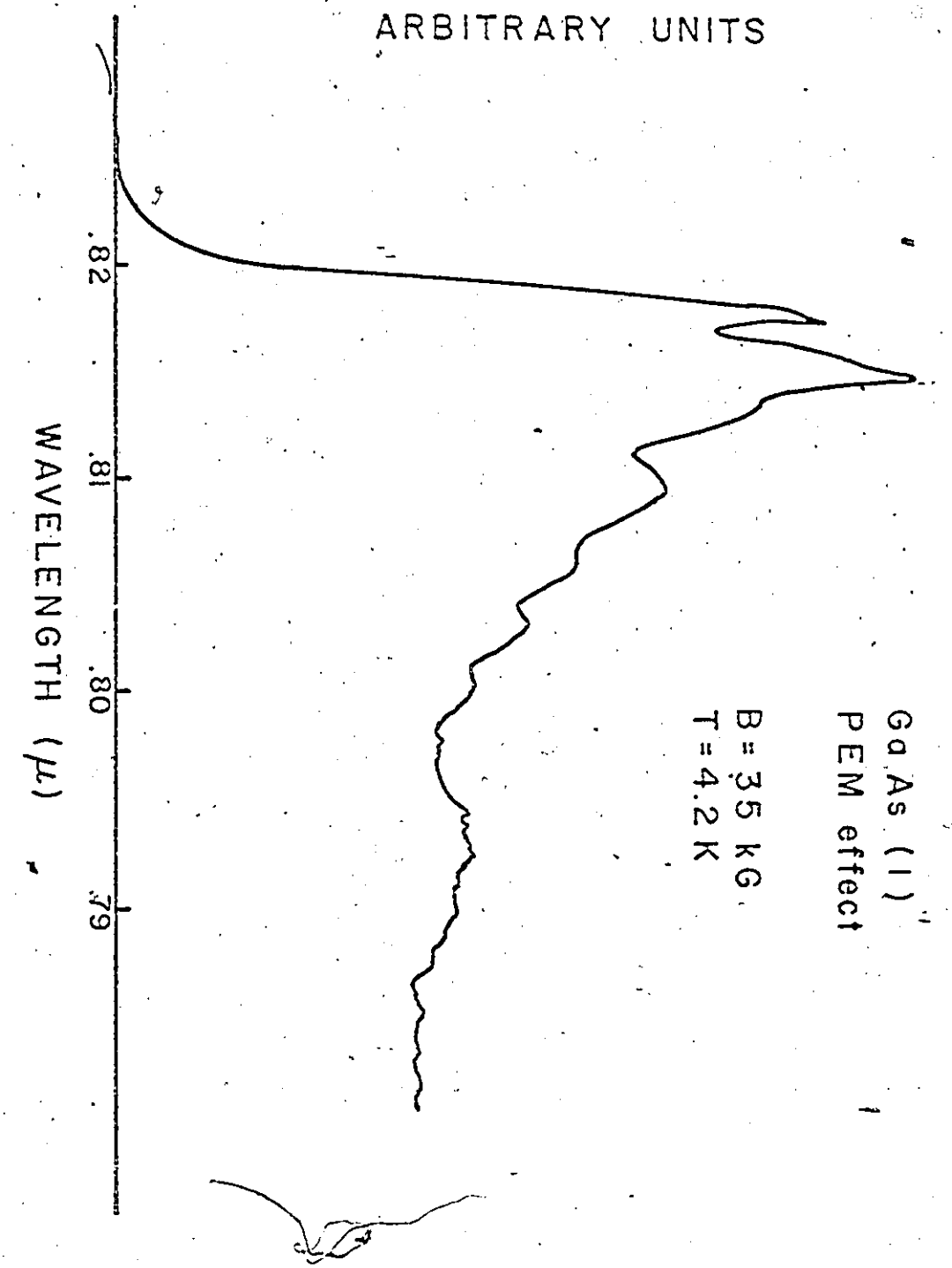

Figure 5.31: PEM spectrum of GaAs (1) at 35 kG.

and 4 denote a 180° phase shift in the photoconductivity signal. This represents either a negative photoconductivity or a drastic change in the photo-response time. No satisfactory explanation is as yet available for this behaviour.

A preliminary comparison with the theory indicates that the photoconductivity minima correspond to magneto-optical interband transitions. A fan diagram of the photoconductivity minima of GaAs (1) is shown in Figure 5.32. The convergence energy of the experimental curves gives, for the direct bandgap energy of GaAs, 1.520 ± 0.001 eV. This is in good agreement with Gilleo et al. (5.16) who report a value of 1.5202 eV obtained in a pure single crystal epitaxial film at 1.4 K. It would therefore appear that the model by Uchinokura and Fan (5.15) is valid in epitaxial GaAs or that the photosensitivity is greater at the surface of the sample. The first minimum labelled 1 extrapolates at zero field to an energy 3.4 meV below the convergence energy of the experimental curves. By optical absorption at 4 K, Sturge et al. (5.17) obtain the same value, i.e. 3.4 meV, for the exciton binding energy in GaAs. This and the upward upward curvature of the experimental curve for this first minimum justify its association to an excitonic level below the conduction band. As can be seen in Figure 5.32, there is a lot of dispersion in the experimental points. This is because the shape of the magneto-optical structures varies with the magnetic field making it very difficult to evaluate the exact energy position of the minima.

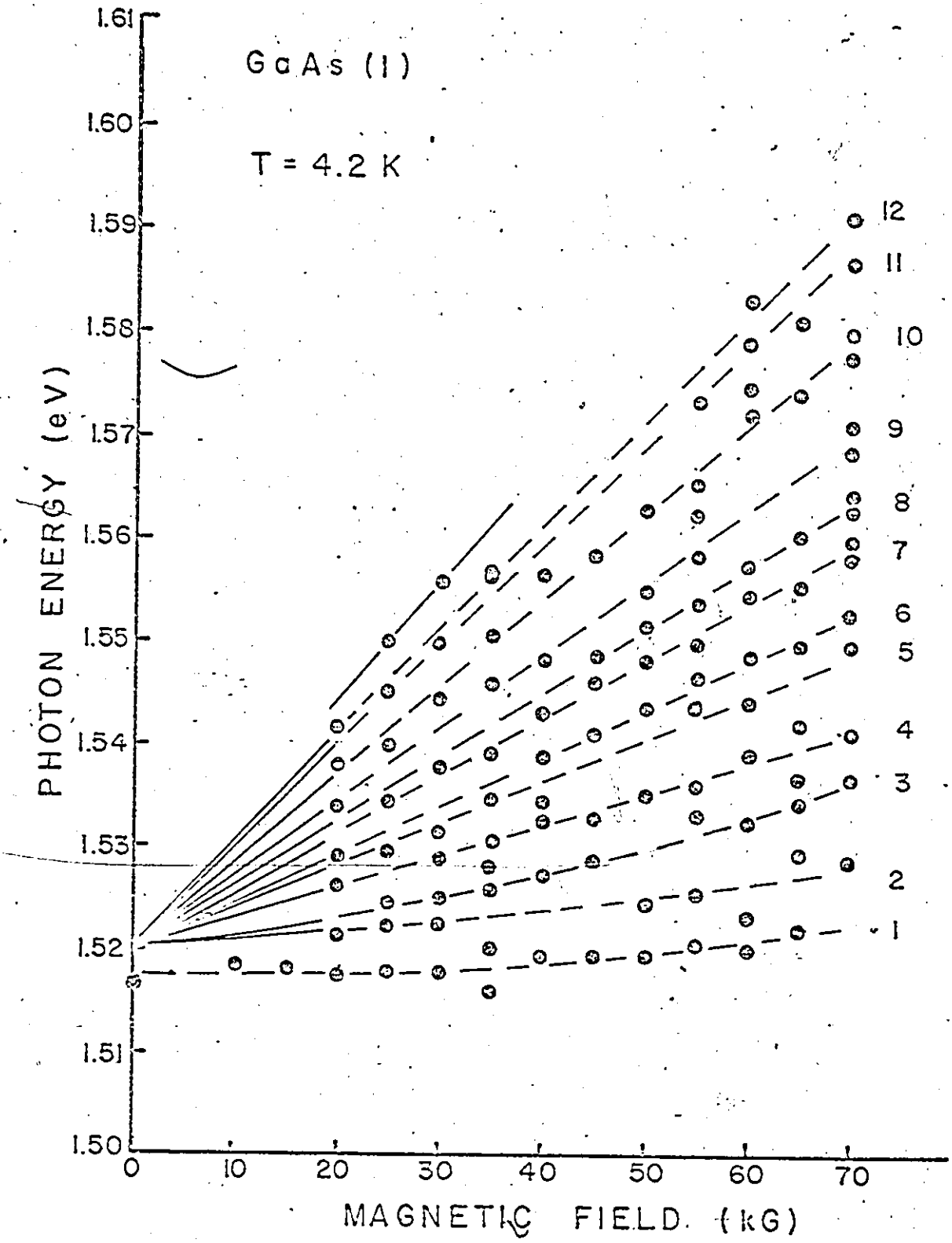

Figure 5.32: Photon energy values at the minima versus the magnetic field strength for the photoconductivity spectra of GaAs (1).

This is a new phenomena, as yet unexplained, and we suspect that this is also the reason why Reine et al. (5.7) did not analyse their stress modulated magneto-reflectivity spectra for GaAs.

5.4.3 The high resistivity material.

A high resistivity GaAs sample, GaAs (2), when studied under the previous conditions exhibits in its photoconductivity spectra the large smooth oscillations associated with phonon-electron interactions. Figure 5.33 gives those oscillations at zero field for both polarizations. The shape of the structures varies with the polarization but not with their energy position. By plotting the energy position of the photoconductivity minima versus the transition order and extrapolating to the zeroeth order, see Figure 5.34, we get for the direct bandgap energy, a value of 1.523 eV. For the energy separation of the oscillations the slope of this graph yields 42.0 meV. Using this result and the following ratio $m_c/m_{hh} = 0.108$ (5.5), we get for the LO phonon energy, 37.9 meV. This is in good agreement with Mooradian (5.18) who reports a value of 36.8 meV obtained by Raman spectroscopy at liquid helium temperature.

Nahory (5.14) reports an oscillatory photoconductivity spectrum at B = 0 for an uncoated epitaxial GaAs sample. This spectrum, shown in Figure 5.35, indicates that surface oxidation plays the same role in GaAs as it does in the previously studied semiconductors, GaSb and InP. The energy position of the minima in

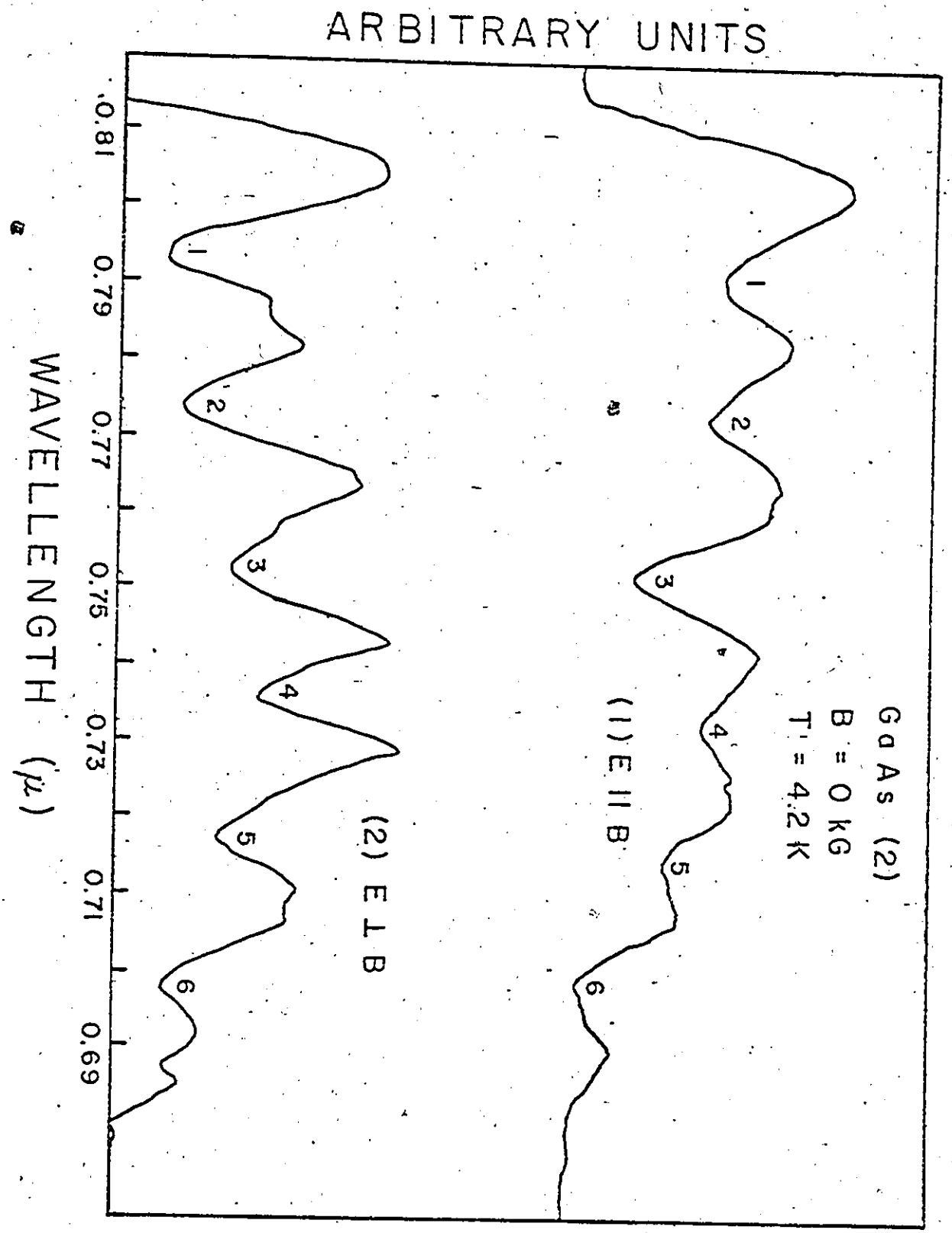

Figure 5.33: Photoconductivity spectra of GaAs (2) for both E ∥ B and E ⊥ B polarization at zero field.

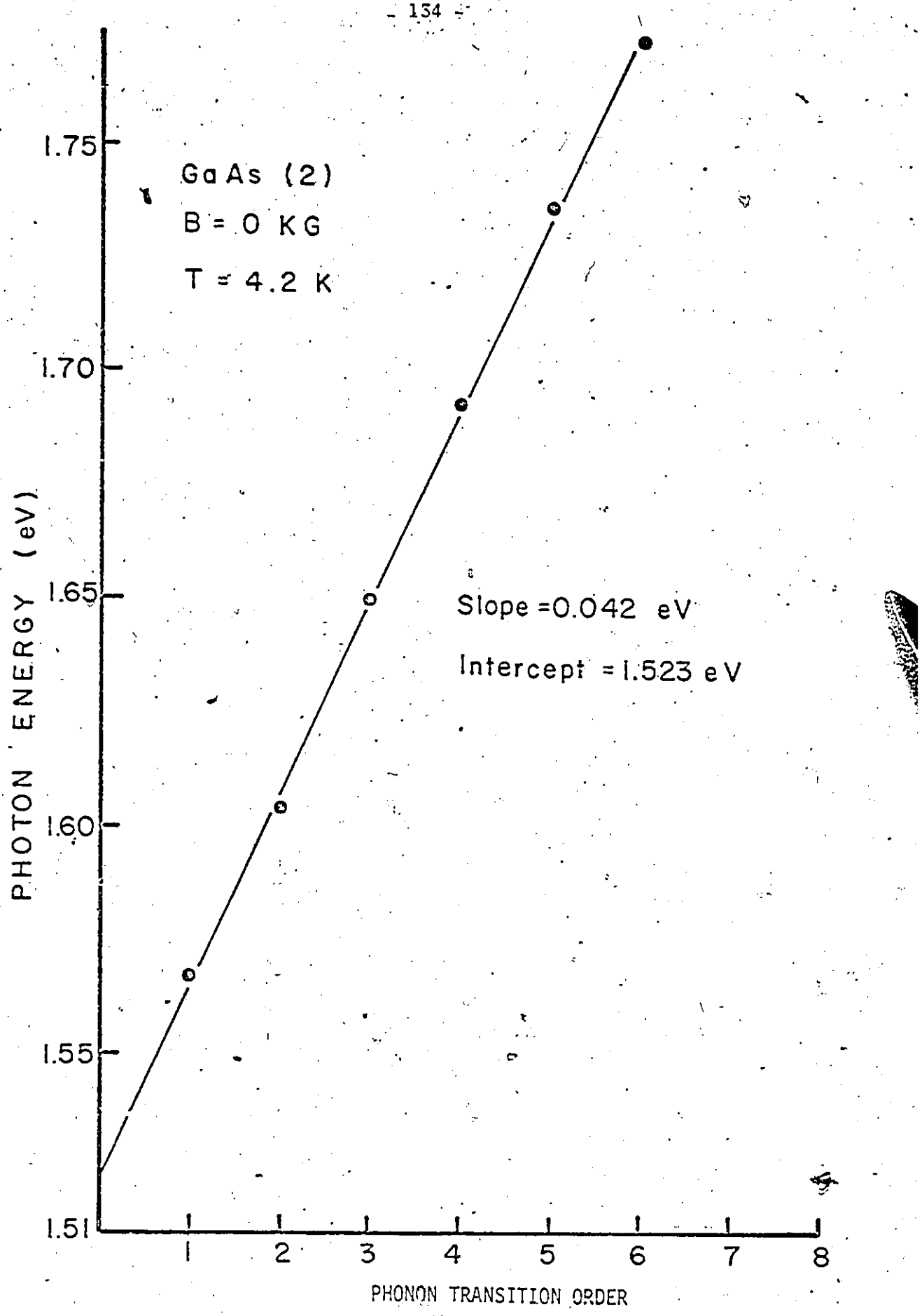

Figure 5.34: Photon energy values a the minima of the photoconductivity spectra of GaAs (2) versus the phonon transition order.

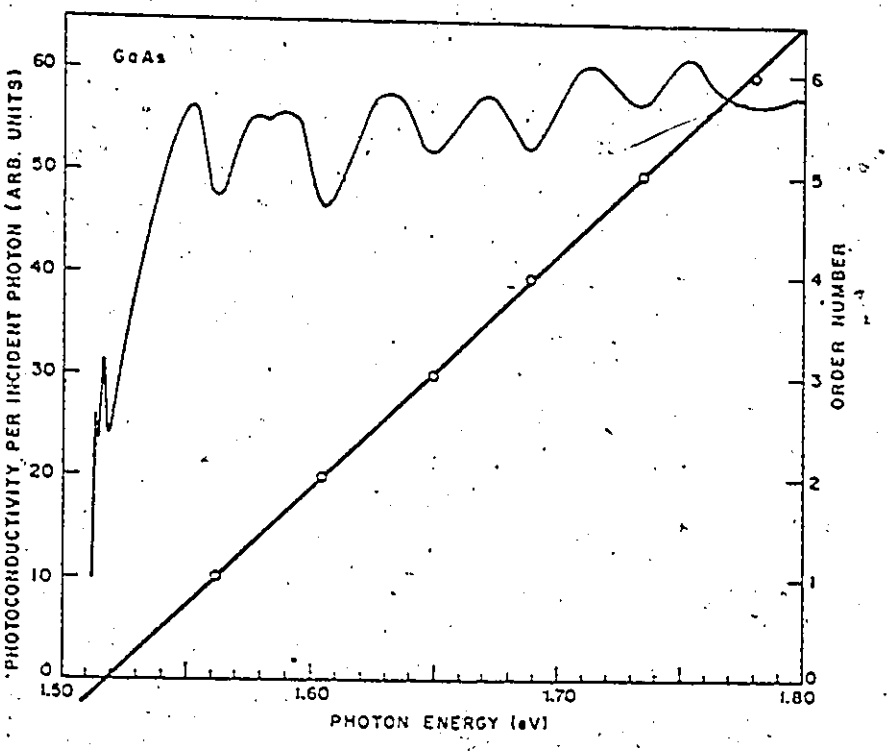

Figure 5.35 Photoconductivity of epitaxial GaAs at B = 0 given by Nahory (5.14).

Nahory's photoconductivity spectrum correspond exactly to those obtained in the chromium doped GaAs (2) sample. Both surface oxidation and doping therefore validate the condition $\tau_{op} < \tau_1 < \tau_{ac}$.* The impurities may either create trapping and increase the recombination lifetime, τ_1, such that $\tau_1 > \tau_{op}$, or, they may promote scattering and decrease the recombination lifetime, such that $\tau_1 < \tau_{ac}$.

In an effort to elucidate the above question, the PEM signal of GaSb (1) and GaSb (2) were studied. GaSb was chosen because it does not require the protective coating of Al_2O_3 which could possibly affect the PEM signal. By investigating the behaviour of the PEM signal as a function of the field for both samples we determined that,

*The reader is refered to chapter 4 section 4.2.

the recombination lifetime τ_1 at the surface of the samples increased as a result of oxidation. Before oxidation the PEM signal of GaSb (1) goes through a maximum at 15 kG, curve I of Figure 5.36 and after oxidation the PEM signal of GaSb (2) saturates, curve II of Figure 5.36. According to the theoretical development presented in chapter 4 the above result signifies that GaSb (2) has a greater surface recombination lifetime than GaSb (1) and that oxidation induces trapping.

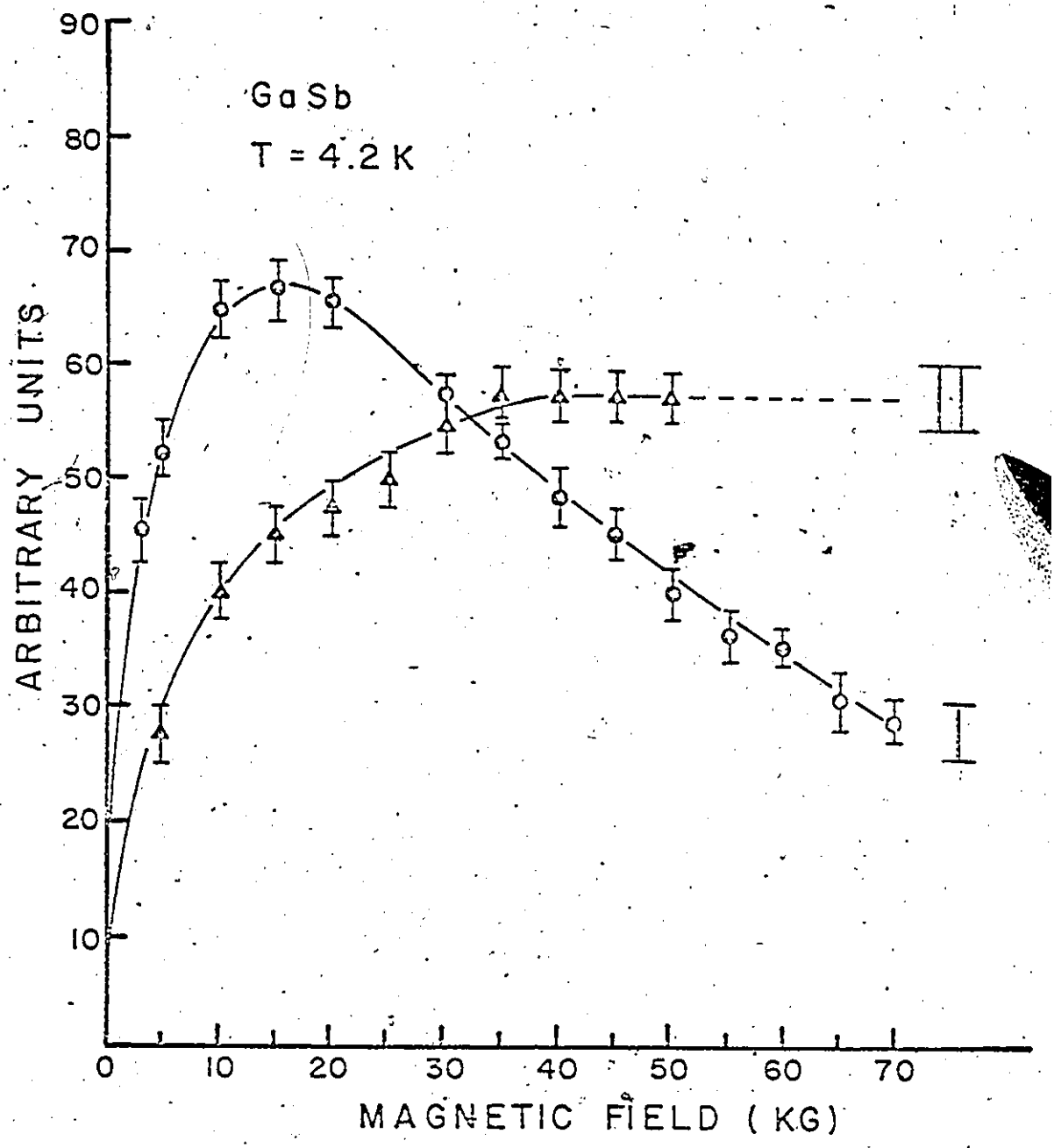

Figure 5.36: The PEM short-circuit signal of GaSb (1), curve I, and GaSb (2), curve II, versus the magnetic field strength.

6. CONCLUSION

The present research was undertaken to develop a new and simple method of observing transitions between Landau levels in semiconductors. It was believed that the already existing methods such as absorption and modulated reflectivity techniques were either too restrictive or too complicated. Various photo-effects such as photoconductivity, the photovoltaic effect and the photoelectromagnetic effect were investigated as possible alternatives to the already existing techniques. The present thesis reports this part of the work and deals mainly with the PEM effect.

A new method of investigating magneto-optical transitions, simply called the PEM technique, did indeed prove quite successful. The degree of success of the new method can be evaluated by comparing it to other techniques. For example the results obtained using GaSb compare very well with those of Reine (.14) and Filion (1.9) using stress modulated reflectivity and photoconductivity respectively. The resulting band parameter values obtained from the PEM measurements agree better with the theoretical predictions of Lawaetz (1.17). The simplicity of the new technique, namely the sample acting as its own detector, the elimination of stress made possible by the convenience of very thick samples, and the possibility of surface protection using an amorphous coating, could possibly explain the better agreement with the theory.

The success obtained with germanium is somewhat more limited and it can serve as illustration of the limitations of this new method. Being a direct method as opposed to a modulated technique the present method reflects more the shifts in the energy position of the maxima resulting from impurity scattering. Consequently in the limit of high impurity scattering which results in considerable broadening of the magneto-optical structures, a correction for the energy position of the maxima is necessary. This difficulty could be removed by coupling the PEM technique to wavelength modulation. This would sharpen the magneto-absorption structures eliminating the above mentioned problem without defeating the purpose of the new method which is its simplicity.

The coupling of the PEM technique with wavelength modulation would perhaps improve the results obtained for InP and GaAs, and possibly other high conduction band effective mass semiconductors to be studied. The results presented on InP and GaAs report the first observation of transitions between Landau levels in InP and the only such work on GaAs since that of Vrehen (6.1) who did measurements by absorption. All the experimental results presented in the previous chapter are summarized in Table 6.1; they demonstrate that the PEM effect does offer an alternative to the existing magneto-optical techniques.

Table 6.1

Recapitulative summary of the experimental results for the present research

Material	Bandgap ε_g in eV	Spin-orbit splitting Δ in eV	Exciton binding energy ε_x in meV	Conduction band effective mass m_c/m	Luttinger's parameters γ_1^L	γ_2^L	Longitudinal optical phonon energy $\hbar\omega_o$ in meV
Germanium	0.888		1.5	0.0385	13.31	5.55	
GaSb	0.812			0.046	12.6	5.2	30.7
InP	1.423	0.102		0.08	6.28	2.76	44.6
GaAs	1.520		3.4				37.9

As a study of the PEM effect itself this work presents the first observations of oscillations in the PEM effect above the fundamental edge. The structures in the PEM signal reflect variations in the absorption coefficient arising because of transitions between Landau levels in the semiconductor. A simple derivation of the PEM effect under ideal conditions gives a square root dependence on the absorption coefficient for the short-circuit PEM current. A more complete theoretical development could be the subject of an interesting theoretical project.

A secondary but important facet of this research work concerns itself with the surface treatment of the samples studied. It was discovered that oxidation of the sample surface deteriorates or quashes the magneto-optical structures, in III-V compounds it even results in the appearance of large phonon structures. The mechanisms involved in surface oxidation and their relation to the sharpness of the magneto-optical structures remains obscure. A more quantitative study of surface conditions would result in the proper monitoring of the surface treatment and the observation of better resolved magneto-optical structures. In this work a pyrolytic coating method was used to reduce surface oxidation.

The PEM technique already offers many useful and interesting advantages over other methods. Nevertheless, this work might be considered as the first step towards a more powerful

technique which would combine the addition of wavelength modulation and a better understanding of the surface conditions. It is believed that the PEM technique would then reveal its full potential and surpass the already existing methods.

APPENDIX

Computer program for the Pidgeon and Brown analysis of the heavy-hole transitions in III - V compounds.

```
FORTRAN IV G LEVEL  21                MAIN                DATE = 74036      22/58/42

      C     FIT AL AIDE DE LA THEORIE DE PIDGEON ET BROWN                    00000030
0001        DIMENSION A1(2),A2(2),A3(2),A4(2),A5(2),A6(2),A7(2),A8(2)        00000040
0002        DIMENSION A9(2),A10(2),A(10)                                     00000050
0003        DIMENSION EN4(18,3,20),END(18,3,20),ET(5)
0004        DIMENSION Y(15,20),X(15,20),CO(3,4)
0005        DIMENSION DE1G(4),DE2GL(4),DE1G3(4),DE2G3L(4),DETG(4),DETG3(4)   00000080
0006        DO 2 N=1,6
0007        M=7-N
0008        DO 2 L=6,12
0009        READ(1,1)X(L,M)
0010        X(L,M)=X(L,M)-.0055
0011        Y(L,M)=X(L,M)
0012         WRITE(3,5)X(L,M)
0013      2 CONTINUE
0014      1 FORMAT(5E13.4)
0015      5 FORMAT(5F13.4)
      C     PARAMETRES FIXES
0016        EG=.0005
0017        DELTA=.246
0018        F=-1.1
0019        SOLX=0.0
0020        SOLY=0.0
0021        SOLZ=0.6
      C     PARAMETRES VARIABLES
0022        CONDM=.038
0023         G1L=13.35
0024         G3L=5.09
0025        DO 10 II=1,20
0026        CONDM=CONDM+SOLX
0027        G1L=G1L+SOLY
0028        G3L=G1L+SOLZ
0029        EP=1.+((1./CONDM)-1.-2.*F)/(2./EG+1./(EG+DELTA))
0030         G2L=G3L-1.38
0031        WRITE (3,7)CONDM,G1L,G3L,EP,G2L
0032      7 FORMAT(15X,'CONDM,G1L,G3L,EP,G2L=  ',5F13.5 )
0033        TAU=EP/(6.*EG)
0034        GPL=G3L
0035        GPPL=2.*G3L/3.+G2L/3.
0036        G1=G1L-2.*TAU
0037        G2=G2L-TAU
0038        G3=G3L-TAU
0039        GP =GPL-TAU
0040        GPP=GPPL-TAU
0041        CONTR=SQRT(GPL*GPL+3.*GPPL*GPPL)
0042        TLEGEP=G1L+CONTR
0043        TLEGEP=1./TLEGEP
0044        TLOURD=G1L-CONTR
0045        TLOURD=1./TLOURD
0046        WRITE(3,41)TLEGEP,TLOURD
0047     41 FORMAT(1CX,'TLEGEP  =',F13.5,'TLOURD  =',F13.5)
0048        GBAR=SQRT(2.*G2L*G2L+2.0*G3L*G3L)
0049        GH=6.*(G3L*G3L-G2L*G2L)/(GBAR*(G1L-GBAR))
0050        TLE=1./(G1L+GBAR)
0051        TLO=(1.+.05*GH+.0164*GH*GH)**.6666/(G1L-GBAR)
0052        WRITE(3,8)TLE,TLO
0053      8 FORMAT(20X,'TLE,TLO=',2F13.4)
0054        APPAL=G3L+2.*G2L/3.-G1L/3.-2./3.
0055        APPA=APPAL-TAU
```

```
FORTRAN IV G LEVEL  21                    MAIN                    DATE = 74036        22/58/42

0056                    DO 102 K=1,15
0057                    L=K
                C       COEFFICIENT DE LA MATRICE A
0058                    A1(1)=L+1.+2.*EP*(L+.5)
0059                    A2(1)=(.5*L*EP)**.5
0060                    A3(1)=-(G1+GP)*(L-.5)-1.5*APPA
0061                    A4(1)=((L+1.)*EP/6.)**.5
0062                    A5(1)=-(3.*(L+1.)*L)**.5*GPP
0063                    A6(1)=-(G1-GP)*(L+1.5)+.5*APPA
0064                    A7(1)=((L+1.)*EP/3.)**.5
0065                    A8(1)=(6.*(L+1.)*L)**.5*GPP
0066                    A9(1)=-(2.**.5)*(GP*(L+1.5)-APPA/2.-.5)
0067                    A10(1)=-G1*(L+1.5)+APPA+.5
                C       COEFFICIENT DE LA MATRICE B
0068                    A1(2)=L+2.*EP*(L+.5)
0069                    A2(2)=(L*EP/6.)**.5
0070                    A3(2)=-(G1-GP)*(L-.5)-.5*APPA
0071                    A4(2)=((L+1.)*EP/2.)**.5
0072                    A5(2)=-(3.*(L+1.)*L)**.5*GPP
0073                    A6(2)=-(G1+GP)*(L+1.5)+1.5*APPA
0074                    A7(2)=(L*EP/3.)**.5
0075                    A8(2)=-(2.**.5)*(GP*(L-.5)+APPA/2.)+.5)
0076                    A9(2)=-(6.*(L+1.)*L)**.5*GPP
0077                    A10(2)=-G1*(L-.5)-APPA-.5
0078                    DO 101 J=1,2
0079                    DO 100 I=1,6
0080                    H=I.A+1/2.0
0081                    S=.0001577*H
0082                    S1=SQRT(S)
0083                    A(1)=A1(J)*S+EG
0084                    A(2)=A2(J)*S1
0085                    A(3)=A3(J)*S
0086                    A(4)=A4(J)*S1
0087                    A(5)=A5(J)*S
0088                    A(6)=A6(J)*S
0089                    A(7)=A7(J)*S1
0090                    A(8)=A8(J)*S
0091                    A(9)=A9(J)*S
0092                    A(10)=A10(J)*S=DELTA
0093                    N=4
0094                    MV=1
0095                    CALL EIGEN (A,R,N,MV)
0096                    IF (J-2) 70,75,80
0097                 70 ENA(K,1,I)=A(1)
0098                    ENA(K,2,I)=A(3)
0099                    ENA(K,3,I)=A(6)
0100                    GO TO 80
0101                 75 ENB(K,1,I)=A(1)
0102                    ENB(K,2,I)=A(3)
0103                    ENB(K,3,I)=A(6)
0104                 80 CONTINUE
0105                100 CONTINUE
0106                101 CONTINUE
0107                102 CONTINUE
0108                    CON=(3.*EG**2.+4.*DELTA*EG+2.*DELTA**2.)/((EG+DELTA)*(3.*EG+2.*
                   1DELTA))
0109                    VE=1./CONDM
0110                    CDE2M=((VE-1.)*CON+(CON*(VE+G1)+2.*G3))*VE**2./EG
```

```
0111                  FA=(EG+2.*DELTA)*(G1L+2.*G3L)/(2.*EG*DELTA)
0112                  DO 23 I=1,3
0113                  DO 23 J=1,4
0114                  CO(I,J)=0
0115               23 CONTINUE
0116                  DI=0.0
                   C  LE PROGR. DIAGONALISE ET PR L LES SOLNS SONT PHI(L) PR LES ELECTR-
                   C  ONS  PHI(L-1) PR LES TROUS LOURDS ET PHI(L+1) PR LES TROUS LEGERS
0117                  DO 99 J=1,2
0118                  IF (J-2)33,33,34
0119               33 KK=7
0120                  GO TO 35
0121               34 KK=5
0122               35 DO 26 L=6,12
0123                  LL=L
0124                  IF(J-2)24,25,26
0125               24 K=L+1.
0126                  N=L+1
0127                  NN=L+1
0128                  WRITE (3,200)L
0129              200 FORMAT(' TRANSITIONS P C D L+1 VALENCE A L COND=',I3)
0130                  GO TO 26
0131               25 K=L-1
0132                  N=L-1
0133                  NN=L-1
0134                  WRITE (3,202)L
0135              202 FORMAT (' TRANSITIONS P C G L-1 A L COND =',I3)
                   C 1   A+(K)AC(L)   2  A-(K)AC(L)   3  B+(K)BC(L)   4 B-(K)BC(L)
0136               26 DE1G=-(L+.5)*VF*VF
0137                  DE2G=(L+.5)**2.*CDE2H
0138                  Z=3.*K*(K+1.)*GPPL+GPPL
0139                  Q=G1L-(K-1.5)*GPL-APPAL
0140                  P=G1L+(K-1.5)*GPL-APPAL
0141                  Q=SQRT(Q=Q+Z)
0142                  R=SQRT(P*P+Z)
0143                  V=1./Q
0144                  U=1./R
0145                  DE1G(1)=-(K-10./6.)-1.3333*V*(G1L-(K-1.5)*GPL-APPAL)
0146                  DE1G(2)=-(K-10./6.)+1.333*V*(G1L-(K-1.5)*GPL-APPAL)
0147                  DE1G(3)=-(K-1.333)-1.333*U*(G1L+(K-1.5)*GPL-APPAL)
0148                  DE1G(4)=-(K-1.333)+1.333*U*(G1L+(K-1.5)*GPL-APPAL)
0149                  DC2GC=-(L+.5)**2.*(VF-1.)*CON/EG
0150                  DE2GL(1)=2.*FA*(K+.5)**2.
0151                  DE2GL(2)=0.
0152                  DE2GL(3)=DE2GL(1)
0153                  DE2GL(4)=0.
0154                  CONS=.5*V*(2.*(G1L-(K-1.5)*GPL-APPAL)*(-K-1./6.)+6.*K*(K+1.)*GPPL)
0155                  DE1G3(1)=1./6.-CONS
0156                  DE1G3(2)=1./6.+CONS
0157                  CONST=.5*U*(2.*(G1L+(K-1.5)*GPL-APPAL)*(K-3.17)+6.*K*(K+1.)*GPPL)
0158                  DE1G3(3)=-1./6.-CONST
0159                  DE1G3(4)=-1./6.+CONST
0160                  DE2G3C=-2.*(VF-1.)*(L+.5)**2./EG
0161                  DE2G3L(1)=4.*FA*(K+.5)**2.
0162                  DE2G3L(2)=0.0
0163                  DE2G3L(3)=DE2G3L(1)
0164                  DE2G3L(4)=0.0
0165                  DO 21 M=1,6
```

```
0166                H=3.2+M/2.0
0167                S=.0001577*H
0168                SC=S*S
0169                DETM=DE1M*S+DE2M*SC
0170                I=(J-2)700,701,701
0171          700   ET(1)=-ENA(NN,3,M)+ENA(LL,1,M)
0172                ET(2)=-ENB(N,2,M)+ENA(LL,1,M)
0173                ET(3)=-ENB(NN,3,M)+ENB(LL,1,M)
0174                ET(4)=-ENB(N,2,M)+ENA(LL,1,M)                                00001720
0175                ET(5)=(ET(2)+ET(4))/2.0                                      00001740
0176                GO TO 702
0177          701   ET(1)=0.0
0178                ET(2)=-ENA(N,2,M)+ENB(LL,1,M)
0179                ET(3)=0.0
0180                ET(4)=-ENA(N,2,M)+ENB(LL,1,M)
0181                ET(5)=(ET(2)+ET(4))/2.0
0182          702   IF(II-5)81,81,83
0183           83   IF(II-10)82,81,84
0184           84   IF(II-15)85,81,85
0185           85   IF(II-20)82,81,1000
0186           81   WRITE(3,66)(ET(JJ),JJ=1,2)
0187           82   CONTINUE
0188           66   FORMAT (20X,4F13.6,F13.4)
0189                DO 19 I=1,4
0190                DETG(I)=-DELG(I)*S+(DE2GC-DE2GL(I))*SC
0191                DETG3(I)=-DEL3(I)*S+(DE2G3C-DE2G3L(I))*SC
0192           19   CONTINUE
0193                ET(2)=ET(5)
0194                DETG(2)=(DETG(2)+DETG(4))/2.0
0195                DETG3(2)=(DETG3(2)+DETG3(4))/2.0
0196           47   I=2
0197           48   CO(1,1)=CO(1,1)+DETM*DETM
0198                CO(1,2)=CO(1,2)+DETM*DETG(I)
0199                CO(1,3)=CO(1,3)+DETM*DETG3(I)
0200                CO(2,2)=CO(2,2)+DETG(I)*DETG(I)
0201                CO(2,3)=CO(2,3)+DETG(I)*DETG3(I)
0202                CO(3,3)=CO(3,3)+DETG3(I)*DETG3(I)
0203                IF(J-2)50,52,21
0204           50   FAC=X(I,M)-ET(I)
0205                GO TO 32
0206           52   FAC=0.0
0207           32   CO(1,4)=CO(1,4)+DETM*FAC
0208                CO(2,4)=CO(2,4)+DETG(I)*FAC
0209                CO(3,4)=CO(3,4)+DETG3(I)*FAC
0210                DI=DI+FAC*FAC
0211           21   CONTINUE
0212           22   CONTINUE
0213           99   CONTINUE
0214         1000   CONTINUE
0215                CO(2,1)=CO(1,2)
0216                CO(3,1)=CO(1,3)
0217                CO(3,2)=CO(2,3)
0218                DRMS=SQRT(DI/42)
0219                WRITE(3,65)DRMS
0220           65   FORMAT(20X,'DRMS=',F13.8)
0221                D =CO(1,1)*(CO(2,2)*CO(3,3)-CO(2,3)*CO(3,2))-
                   1   CO(1,2)*(CO(2,1)*CO(3,3)-CO(2,3)*CO(3,1))
                   1  +CO(1,3)*(CO(2,1)*CO(3,2)-CO(2,2)*CO(3,1))
```

```
FORTRAN IV G LEVEL 21          MAIN                    DATE = 74036      22/50/42
0222                 DX=CO(1,4)*(CO(2,2)*CO(3,3)-CO(2,3)*CO(3,2))-
                    1   CO(1,2)*(CO(2,4)*CO(3,3)-CO(2,3)*CO(3,4))
                    1  +CO(1,3)*(CO(2,4)*CO(3,2)-CO(2,2)*CO(3,4))
0223                 DY=CO(1,1)*(CO(2,4)*CO(3,3)-CO(2,3)*CO(3,4))-
                    1   CO(1,4)*(CO(2,1)*CO(3,3)-CO(2,3)*CO(3,1))
                    1  +CO(1,3)*(CO(2,1)*CO(3,4)-CO(2,4)*CO(3,1))
0224                 DZ=CO(1,1)*(CO(2,2)*CO(3,4)-CO(2,4)*CO(3,2))-
                    1   CO(1,2)*(CO(2,1)*CO(3,4)-CO(2,4)*CO(3,1))
                    1  +CO(1,4)*(CO(2,1)*CO(3,2)-CO(2,2)*CO(3,1))
0225                 WRITE(3,500)D,DX,DY,DZ
0226           500   FORMAT(20X,4E13.5)
0227                 SOLX=DX/D
0228                 SOLY=DY/D
0229                 SOLZ=DZ/D
0230                 WRITE (3,64)SOLX,SOLY,SOLZ
0231              64 FORMAT (20X,'X,Y,Z  ',3F13.6)
0232              10 CONTINUE
0233                 RETURN
0234                 END
```

REFERENCES

1.1 Burstein, E., Picus, G. S., Wallis, R. F., Blatt, F. 1958. Phys. Rev. 113, 15.

1.2 Zwerdling, S., Lax, B., Roth, L. M., Button, K. J. 1959. Phys. Rev., 114, 80.

1.3 Aggarwal, R. L. 1970. Phys. Rev. B, 2, 446.

1.4 Reine, M., Aggarwal, R. L., Lax, B. 1972. Phys. Rev. B, 5, 3033.

1.5 Vrehen, Q. H. F., 1968. J. Phys. Chem. Solids, 29, 129.

1.6 Pidgeon, C. R., Brown, R. W. 1966. Phys. Rev., 146, 575.

1.7 Zwerdling, S., Lax, B., Button, K. J., Roth, L. M., 1959 J. Phys. Chem. Solids, 9, 320.

1.8 Cardona, M. 1969. Modulation Spectroscopy; Solid State Physics; Supplement II, (Academic Press).

1.9 Filion, A., Fortin, E. 1973. Phys. Rev. B. 8, 3852.

1.10 Rochon, P., Fortin, E. 1974. Bull. Am. Soc. p. 248, March (Can. J. Phys. 1974).

1.11 Kikoin, K., Noskov, M. 1934. Physik Sowajetunion, 5, 585.

1.12 Ph.D. Thesis by J. P. Zielinger entitled: 'Contribution à l'étude des propriétés photogalvanomagnétiques de Cu_2O à 77K et de leur rapport avec l'absorption excitonique et la structure de bandes'.

1.13 Moss, T. S., Burrell, G. J., Ellis, B. 1973. Semiconductor Opto-Electronics, Editor, John Wiley and Sons, New York.

1.14 Roosbroeck, W. 1956. Phys. Rev. 101, 1713.

1.15 Ph.D. Thesis by A. Filion entitled: 'Etude des propriétés photoconductrice du GaSb et du $GaAs_xSb_{1-x}$ et de la reflecticité modulée en longueur d'onde du GaSb en présence d'un champ magnétique'.

1.16 Luttinger, J. M., Kohn, W. 1955. Phys. Rev. 97, 869.

1.17 Lawaetz, P. 1971. Phys. Rev., B4, 3460.

1.18 Nahory, R. E. 1968. Phys. Rev., 178, 1293.

2.1 see reference 1.15

2.2 Aboaf, J. A. 1967. J. Electrochem. Soc. Solid State Science, 114, 948.

3.1 Luttinger, J. M., Kohn, W. 1955. Phys. Rev., 97, 869; Luttinger, J. M. 1956. Phys. Rev., 102, 1030.

3.2 see reference 1.6

3.3 Landau, L. 1930. Z. Physik 64, 629.

3.4 see reference 1.2

3.5 Kane, E. O. 1957. J. Phys. Chem. of Solids 1, 249.

3.6 Aggarwal, R. L. 1972. Semiconductors and Semimetals 9, Modulation Techniques (Academic Press).

3.7 Hall, L. H., Bardeen, J., Blatt, F. J. 1954. Phys. Rev. 95, 559.

3.8 Bube, R. H., 1974. Electronic Properties of Crystalline Solids (Academic Press).

4.1 See reference 1.14.

4.2 Chattopadhyaya, S. K., Mathur, V. K. 1969. J. Appl. Phys. 40, 1930; Libe, D. L. Phys. Rev. B 8, 4708, 1973.

4.3 Habegger, M. A., Fan, H. Y. 1963. Phys. Rev. Lett. 12, 99.

4.4 Uchinokura, K., Fan, H. Y. 1970. Phys. Rev. B. 1, 3395.

5.1 See reference 1.3

5.2 Senechal, R. R., Woolley, J. C. 1971. Phys. Rev. Lett. 27, 1563; Glinski, R. G. 1973. J. Phys. C: Solid State Physics 6, 3689.

5.3 Hensel, J. C. 1968. Phys. Rev. Lett. 20, 983; Hensel, J. C., Suzuki, K. 1969. Phys. Rev. Lett. 22, 838.

5.4 Zakharchenya, B. P., Seysyan, R. P. 1967. Sov. Phys. Solid State 8, 2846; Zhilich, A. G., Monozon, B. S. 1967. Sov. Phys. Solid State 8, 2846.

5.5 Lawaetz, P. 1971. Phys. Rev. B 4, 3460.

5.6 see reference 1.7.

5.7 See reference 1.4

5.8 See reference 1.9.

5.9 Hass, M., Henvis, B. W. 1962. Phys. and Chem. of Solids 23, 1099.

5.10 See reference 1.10.

5.11 Shaklee, K. L., Cardona, M., Pollack, F. M. 1967. Phys. Rev. 154, 696.

5.12 Turner, W. J., Reese, W. E., Pettit, R. S. 1964. Phys. Rev. 136, A1467.

5.13 Hilsum, C. et al. 1969. Sol. Stat. Comm. 7, 1057.

5.14 see reference 1.18

5.15 see reference 4.4

5.16 Gilleo, M. A., Bailey, P. T., Hill, D. E. 1968. Phys. Rev. 174, 898.

5.17 Sturge, M. D. 1962. Phys. Rev. 127, 768.

5.18 Mooradian, A., Wright, G. B. 1966. Sol. Stat. Comm. 4, 431.

5.19 Ohyama, T., Murose, K., Otsuka, E. 1970. J. Phys. Soc. Japan, 29, 912.

6.1 see reference 1.5.

ACKNOWLEDGEMENTS

The author takes this opportunity to thank Dr. Emery Fortin for suggesting the PEM effect as a method of investigating the magneto-optical transitions in a semiconductor. His encouragement and collaboration throughout this research project were greatly appreciated. During the four years of my graduate studies I received financial support in the form of an Ontario Graduate Fellowship and a National Research Council of Canada Scholarship.

In addition to Dr. Emery Fortin, several people have contributed to this thesis: Dr. André Filion who first used the apparatus to study photoconductivity in GaSb and Mr. Paul Rochon who is presently studying the photovoltaic effect with this same apparatus. The frequent exchange of ideas with the professors and students of the department have proved most profitable to the author. In particular I would like to thank Dr. K. S. Song and my fellow graduate students Dr. O. Berolo, Dr. J. Basinski, Dr. R. Senechal, Mr. F. Prat and Mr. R. Glinski.

One should not forget the assistance of Mr. N. Goodchild and his shop staff, in particular, Mr. R. Hart, in the installation and operation of the apparatus and Mrs. L. Leroux and Miss M. Mes who typed this manuscript.

The author is indebted to Dr. H. Pullan of the Ontario Research Foundation who provided the Ge (M) sample and to

Dr. D. L. Rode of the Bell Laboratories in Murray Hill who provided the epitaxial GaAs (1) sample.